
Unterschrift des Betreuers



TECHNISCHE
UNIVERSITÄT
WIEN

Vienna University of Technology

DIPLOMARBEIT

Understanding Muon Detection Efficiencies for Quarkonium Polarization Measurements at the Compact Muon Solenoid

AUSGEFÜHRT AM

Atominstitut Wien

in Verbindung mit dem Institut für Hochenergiephysik (HEPHY)
der Österreichischen Akademie der Wissenschaften (ÖAW)

UNTER DER ANLEITUNG VON

Univ.Doz. DI. Dr. Claudia-Elisabeth Wulz

EINGEREICHT AN

der Technischen Universität Wien
Fakultät für Physik

VON

Johannes Brandstetter
Bubing 113
4782, St.Florian, Österreich

Ort, Datum

Unterschrift (Student)

Abstract

Quarkonium physics is a fundamental field of research to get a better understanding of quantum chromodynamics – the theory of the strong interaction. *Quarkonia* are bound states of the heavy charm or bottom quark and their respective antiquarks, i.e. $c\bar{c}$ and $b\bar{b}$ states. The complexity of understanding the quarkonium production mechanism has given rise to various theoretical models. The *Large Hadron Collider* (LHC) reaches unprecedented high collision energies and has already significantly contributed to understanding the experimental side of the quarkonium puzzle. The CMS detector is well suited to study the polarization of promptly-produced χ_{cJ} states, using data taken in proton-proton collisions in 2012 at a center of mass energy of $\sqrt{s} = 8$ TeV. This thesis describes the general strategy of the analysis, focusing on the most important input parameters, namely the muon detection efficiencies. Single muon detection efficiencies as well as muon pair correlations are presented.

Kurzfassung

Die Physik der Quarkonium Zustände gilt als wichtiger Baustein für das Verständnis der starken Wechselwirkung. Als *Quarkonia* werden gebundene Quark-Antiquark Paare bezeichnet; von besonderem Interesse sind dabei $c\bar{c}$ und $b\bar{b}$ Zustände. Eine Vielzahl theoretischer Modelle versuchen die Komplexität der Formation derartiger Quarkonium Zustände zu beschreiben. Aus experimenteller Sicht eröffnen die Hochenergieexperimente am *Large Hadron Collider* (LHC) eine neue Möglichkeit, diesem Rätsel auf die Spur zu kommen. Mit 2012 aufgenommenen Daten aus Proton-Proton Kollisionen bei einer Schwerpunktsenergie von $\sqrt{s} = 8$ TeV wird mithilfe des CMS Detektors die Polarisation von prompten χ_{cJ} Zerfällen gemessen. In dieser Arbeit wird zuerst auf die Strategie zur Messung der Polarisation eingegangen und anschließend eine Spezialisierung auf die wichtigsten Eingabeparameter, die Effizienzen der Myondetektion, gemacht. Hierbei werden sowohl Untersuchungen der Effizienzen einzelner Myonen als auch der Korrelationen der Myonpaare durchgeführt und ausführlich diskutiert.

Contents

1	Introduction and Motivation	7
2	CERN and the LHC	9
3	The CMS Detector	12
3.1	Structure of the CMS Detector	12
3.1.1	Coordinate System and Frequently Used Units	12
3.1.2	The Inner Tracker	13
3.1.3	The Electromagnetic Calorimeter (ECAL)	14
3.1.4	The Hadronic Calorimeter (HCAL)	14
3.1.5	Superconducting Magnet	14
3.1.6	Muon Detectors	15
3.2	Trigger system	17
3.2.1	Level-1 Trigger	17
3.2.2	High Level Trigger	19
3.2.3	Performance of the CMS Detector	21
4	The Standard Model of Particle Physics	22
4.1	Particles of the Standard Model	24
4.2	Important Mathematical Concepts	25
4.3	Quantum Chromodynamics (QCD) - the Theory of the Strong Interaction	27
5	Quarkonium Physics	29
5.1	The Quarkonium Spectrum	29
5.1.1	Quarkonia as Tool to Understand Strong Interactions	32
5.2	Underlying Physics of Quarkonium Production	33
5.2.1	The NRQCD Factorization Approach	34
5.2.2	Color-Singlet Model	35
5.2.3	Color-Evaporation Model	36
5.2.4	Theoretical models compared to experimental data	36
6	Quarkonium Polarization	39

6.1	Concepts and Definitions	39
6.2	The Quarkonium Polarization Puzzle	43
6.3	Measurement of χ_{cJ} Polarization	44
6.4	Recent CMS Results	46
7	Tag and Probe Efficiencies	49
7.1	Tag and Probe Method	49
7.2	Used Datasets, Filters and Triggers	51
7.3	Offline Muon Reconstruction Efficiency	53
7.3.1	Scale Factor	59
7.4	Efficiency of the Muon Tracking Quality Cuts	60
7.5	L1-L2 Efficiency	63
7.5.1	Forward $ \eta $ Region	69
7.6	L3 Efficiency	70
7.7	Total Single Muon Efficiency	75
7.7.1	The MC-truth Approach	81
7.7.2	Pileup Studies	82
7.8	Dimuon Vertex Efficiencies	84
8	Muon Pair Correlations	87
8.1	Data-driven Determination of the ρ Factor	87
9	Pseudo-Data Tests	96
9.1	Seagull and Cowboy Dimuon Efficiencies	98
9.2	Pileup Dependent L3 Efficiencies	104
10	Summary and Conclusions	109
11	Acknowledgements	111
12	Appendix A	112
13	Appendix B	121
	Bibliography	124
	List of Figures	130
	List of Tables	136
	Acronyms and Abbreviations	138

1 Introduction and Motivation

Quarkonium physics, which describes the bound states of charm and bottom quarks and their respective antiquarks ($c\bar{c}$, $b\bar{b}$), has become a fundamental research field since the discovery of the J/ψ meson in 1974. From then onwards, a wide range of experiments has been conducted, but the results prior to the LHC era are inconsistent and have given rise to several theoretical models. However, these theory-guided models fail to correctly reproduce the differential production cross sections and the polarization measurements of the quarkonium states at the same time.

Since 2010 the *Large Hadron Collider* (LHC), located at CERN, the European Organization for Nuclear Research, provides proton-proton (pp) collisions at unprecedented center of mass energies. Therefore, the CMS detector at the LHC is ideally suited for quarkonium physics, especially since CMS can cover a wide range of different transverse momenta. This thesis deals with the polarization analysis of promptly produced χ_{cJ} states which are studied by their decay into a photon and a J/ψ meson, where the latter decays further into two muons. The analysis uses data taken by the CMS detector in 2012 at a center of mass energy of $\sqrt{s} = 8$ TeV.

First a short introduction of CERN and the LHC (Chap. 2) is given, followed by a description of the CMS detector, with emphasis on subdetector systems relevant for the polarization analysis (Chap. 3). In Chap. 4, the standard model of particle physics is briefly discussed with the focus on quantum chromodynamics (QCD), the theory of the strong interaction. Chapter 5 gives an introduction to both the charmonium ($c\bar{c}$) and the bottomonium ($b\bar{b}$) spectra and introduces the most important mathematical models describing quark-antiquark production. Furthermore, different quarkonium cross section measurements are discussed. Chapter 6 discusses the basic ideas of quarkonium polarization measurements, the strategy of the χ_{cJ} polarization analysis which is currently being performed at CMS and recent results on quarkonium production.

Chapter 7 introduces the Tag and Probe (TnP) method and focuses on the study of single muon detection efficiencies. In doing so, due to different detector and trigger levels, the analysis has to be split up into several sequential efficiencies. Furthermore, muon pair correlations have to be taken into account, in order to extract dimuon detection efficiencies. This yields the so called ρ factor as an additional correction (Chap. 8). In order to test basic results and investigate their influences on the analysis, pseudo-data tests are conducted in Chap. 9.

The author contributes to the χ_{cJ} polarization analysis by updating the TnP framework, determining single muon efficiencies as well as muon pair correlations and dimuon vertex efficiencies based on data collected with the CMS detector during 2012. Furthermore, results are evaluated within the analysis framework using pseudo-data tests.

2 CERN and the LHC

CERN [1], which is the acronym for '*Conseil Européen pour la Recherche Nucléaire*' (European Organization for Nuclear Research), is a huge high-energy physics research complex, established in 1954 and situated at the French-Swiss border in Meyrin near Geneva. At the moment 21 member states are part of CERN and additionally others like the U.S.A. or Russia have observer status. Altogether more than 600 universities and more than 100 countries are represented. Over the last decades CERN has undoubtedly become the center of high-energy physics. Some of its great achievements were, among others:

- Discovery of the weak neutral currents in 1973 [2][3]
- Discovery of the W and Z bosons in 1983 [4]
- Creation and isolation of antihydrogen atoms [5]
- Discovery of direct CP violation [6]
- Discovery of the Higgs boson in 2012 [7][8]

Furthermore, due to everlasting needs of new and better technology, CERN also serves as pioneer in several fields, e.g. computer science, grid computing, accelerator and detector techniques and many others. The development of the *World Wide Web* based on the concept of hypertext by Tim Berners-Lee in 1989 was, for example, one of the great achievements at CERN.

A wide range of different experiments are running at the moment or are planned for the near future. Besides the LHC, which is well known for its gigantic measures and its by far highest achieved accelerating energy worldwide, many other accelerators exist at CERN. On the one hand they are built for several different experiments, and on the other hand they are required to preaccelerate particles helping them to gain enough energy to be able to circulate in the LHC. In Fig. 2.1 the entire acceleration and experimental complex of CERN is pictured.

For pp collisions, which physics analysis in the CMS detector is based on, the following acceleration processes have to be undergone:

- LINAC2 (Linear Particle Accelerator), accelerating protons up to 50 MeV
- PSB (Proton Synchrotron Booster), acceleration up to 1.4 GeV

- PS (Proton Synchrotron), acceleration up to 26 GeV
- SPS (Super Proton Synchrotron), acceleration up to 450 GeV

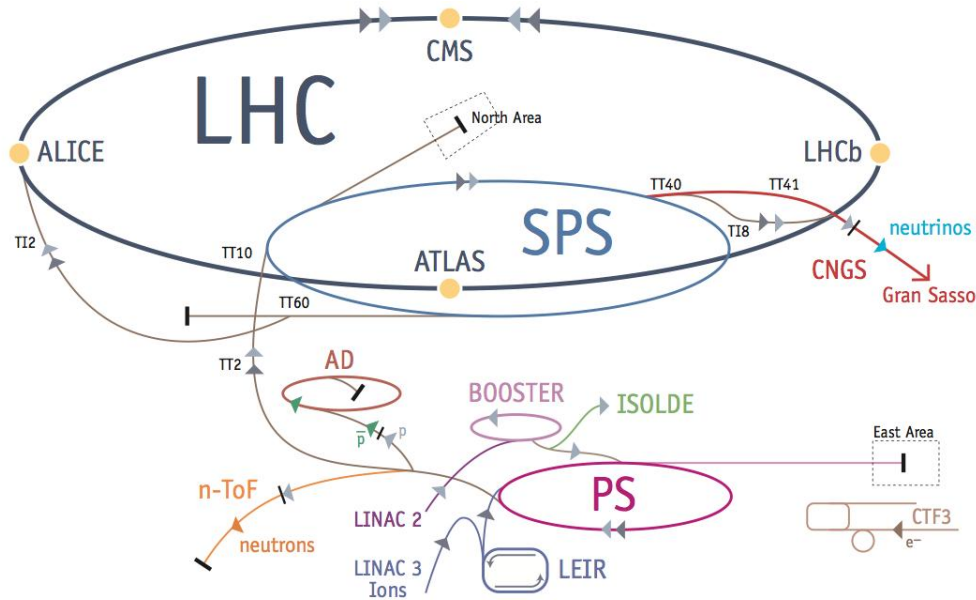


Figure 2.1: Sketch of experiments and accelerators running at CERN [9].

After the SPS, the already very highly energetic protons are injected into the LHC with a circumference of approximately 27 kilometres, where it takes roughly another twenty minutes to reach the final collision center of mass energy of $\sqrt{s} = 7$ GeV in 2011 and $\sqrt{s} = 8$ GeV in 2012, respectively. Runs of $\sqrt{s} = 13$ GeV and $\sqrt{s} = 14$ GeV are foreseen after the ramp up of the LHC in 2015. It is not difficult to guess why the nickname *'the beast'* is given to the LHC.

Collisions happen every 25 ns correlating a bunch revolution frequency of about $\nu = 11$ kHz, when two reversed *bunches* of approximately 10^{11} protons are brought to collision in one of four detectors:

1. *ATLAS* (A Toroidal LHC Apparatus)
2. *CMS* (Compact Muon Solenoid)
3. *ALICE* (A Large Ion Collider Experiment)
4. *LHCb* (Large Hadron Collider beauty)

Accelerators are characterized by the so called *instantaneous luminosity*,

$$L = \nu_n \cdot \frac{N_1 \cdot N_2}{A}, \quad (2.1)$$

where ν_n is the repetition frequency, N_1 and N_2 are the number of particles and A is the impact surface. The LHC is designed for an instantaneous luminosity of $10^{34} \text{ cm}^{-2}\text{s}^{-1}$, meaning that the LHC might produce 10^{34} collisions per second and per cm^2 in the detectors. The luminosity integrated over time is a measure of the collected amount of data and is another important value to characterize the performance of an accelerator. As 1 barn equals 10^{-24}cm^2 , normally the unit *inverse femtobarn* (fb^{-1}) is used. An integrated luminosity of 1 fb^{-1} means that for a process with a cross section of 1 fb one event (on average) has been collected.

3 The CMS Detector

3.1 Structure of the CMS Detector

The CMS detector [10][11] is 21.6 metres long, has a diameter of 15 metres and weighs approximately 12500 tonnes. Its name *Compact Muon Solenoid* arises from two characteristic properties. On the one hand it is constructed around a large solenoid, which generates an extremely strong magnetic field of approximately 4 Tesla; this field is confined by several layers of a *steel yoke* which is mostly responsible for its huge mass. The second part of the name comes from the fact that this steel yoke stops all particles except for muons. Furthermore, the CMS detector consists of silicon trackers, electromagnetic calorimeters, hadron calorimeters and muon chambers. A segment of the detector is shown in Fig. 3.1. The subsystems of the experiment are divided into a cylindrical barrel part (*central region*) and two facing *endcap* sections.

In order to identify particles, characteristic properties like mass, charge, momentum etc. are measured. For practical purposes the determination of position, momentum or loss of momentum as well as energy or loss of energy is frequently used.

3.1.1 Coordinate System and Frequently Used Units

The coordinate system of the CMS detector is centered at the nominal collision point. Hereby, the z axis points westwards along the beam direction, the y axis points vertically upwards and the x axis points inwards to the center of the LHC ring. The polar angle ϑ is measured with respect to the z axis and the azimuthal angle φ is measured with respect to the x-y plane, respectively [10].

The *pseudorapidity* η is defined as,

$$\eta = -\ln \left[\tan \left(\frac{\vartheta}{2} \right) \right]. \quad (3.1)$$

It is also possible to express η in terms of the momentum,

$$\eta = \frac{1}{2} \ln \left(\frac{|\mathbf{p}| + p_L}{|\mathbf{p}| - p_L} \right), \quad (3.2)$$

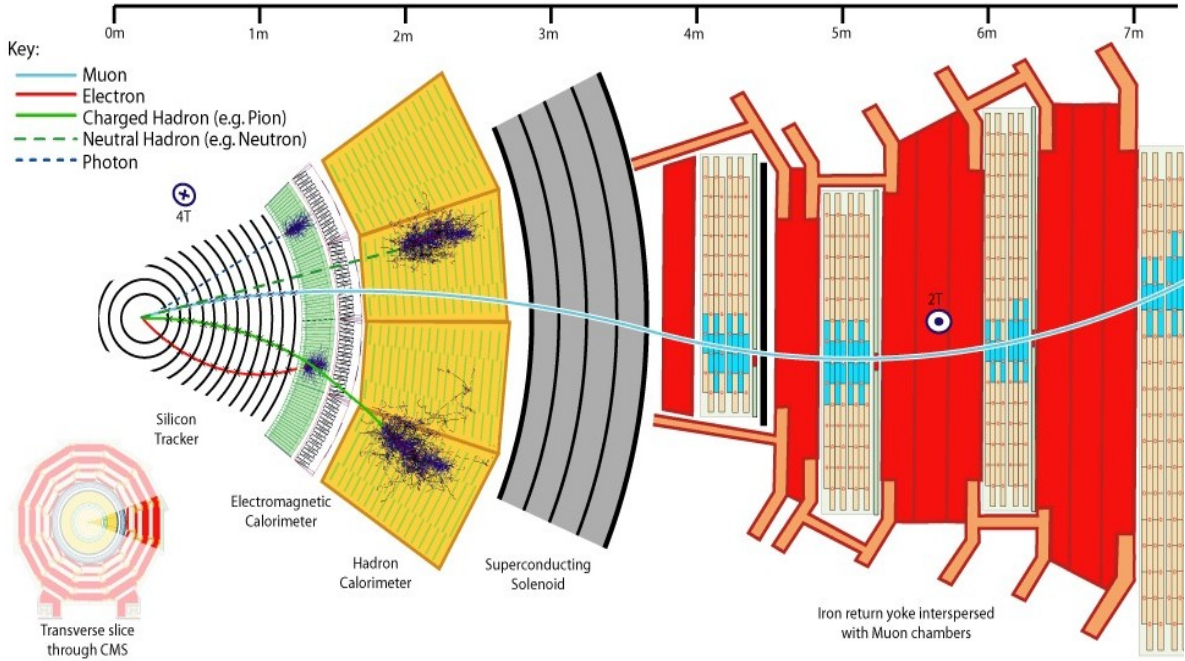


Figure 3.1: Segment of the CMS detector with various layers [12].

where p_L is the longitudinal momentum component.

A closely related variable is the *rapidity* y ,

$$y = \frac{1}{2} \ln \left(\frac{E + p_L}{E - p_L} \right), \quad (3.3)$$

where E refers to the energy of a particle. In contrast to η , y is not angle dependent. Another important variable for characterizing particles is the *transverse momentum* p_T .

3.1.2 The Inner Tracker

The innermost part of the detector, the silicon tracker, is very important for determining the momentum of the particles. One method of calculating a momentum is exploiting the fact that charged particles are bent by the Lorentz force in a magnetic field:

$$p \propto q \cdot r \cdot B \quad (3.4)$$

By tracking the curvature r of a particle with the electric charge q through the magnetic field B , its momentum p can be measured. Hence, the CMS tracker system uses several fixed points in order to identify the position of charged particles. Calculating the curvature of particles in magnetic fields gives fractional errors pro-

portional to the momentum of the particle. The tracker consists of several layers of silicon detectors. Passing charged particles produce electron-hole pairs and, thus, electric signals in silicon crystals are generated, which are amplified and detected. Altogether the silicon tracker covers an area of approximately 200 m^2 and consists of 13 layers in the central region and 14 layers in the endcaps, respectively.

3.1.3 The Electromagnetic Calorimeter (ECAL)

The ECAL [13] is designed to measure the energy of two very important particles: electrons and photons. While tracking detectors cause minimal disturbance to charged particles, shower detectors, in contrast, degrade the energy of particles sharing it among a large number of shower products. The big advantages of calorimeters over tracking detectors are the sensitivity to both charged and neutral particles and the fact of increasing accuracy with increasing energy due to decreasing fluctuation in shower processes.

Particles lose energy in the ECAL either due to bremsstrahlung or due to pair production. The more energy the original particle has, the more *shower particles* are produced. The ECAL is constructed from $PbWO_4$ crystals which are extremely dense but optically clear and therefore ideal for stopping high energy particles. Bypassing electrons and photons produce light in proportion to the particle's energy. Additionally, the ECAL contains preshower detectors in front of the endcaps. These detectors are used to distinguish between single high-energy photons less interesting low-energy photons.

3.1.4 The Hadronic Calorimeter (HCAL)

In contrast to the ECAL, the HCAL [14] measures the energy of hadrons, e.g. protons, neutrons, pions, kaons. Altogether, the HCAL is made out of 36 wedges, each of which weighs approximately 20 tons. The functionality is similar to the ECAL with the difference that the HCAL is much larger due to the huge amount of secondary particles resulting from the generally higher energetic hadrons. The HCAL is among other things made out of over a million World War II brass shell casements from the Russian Navy. It is designed for identifying position, energy and arrival time of particles using alternating layers of absorbers and scintillators. A larger HCAL would result in more precise measurements of hadrons, but in CMS its size is limited due to the surrounding solenoid.

3.1.5 Superconducting Magnet

The CMS magnet is not only responsible for the detector's name, it is also the central part around which the experiment is built. The solenoid's field strength of approximately 4 Tesla allows a very precise determination of the charge/mass ratio

due to the strong curvature in its field. The aim of having the strongest magnet possible in the detector originated from the request to be able to measure even high-energetic particles accurately enough. The stronger the field, the more the path of each particle is bent and, thus, it will even be possible to determine the highest-momentum particles resulting from $\sqrt{s} \sim 14$ TeV centre of mass collisions. The inner tracker, ECAL and HCAL fit smoothly inside the magnetic coil, while the iron structure and the muon detectors surround it.

3.1.6 Muon Detectors

Muons have the characteristic of penetrating several metres of iron without interaction and, unlike the majority of other particles, they are not stopped by any of the previous detectors. Three kinds of muon systems are installed in the CMS detector:

- Muon Drift Tubes (DT)
- Cathode Strip Chambers (CSC)
- Resistive Plate Chambers (RPC)

Figure 3.2 shows the position of the three muon systems inside the CMS detector. Figure 3.3 is an example of four reconstructed muons, three in the DTs and one in the CSCs and RPCs, respectively. The pseudorapidity region $|\eta| < 2.4$ is fully covered by muon detectors, ensuring muon reconstruction over a range corresponding to $0^\circ < \vartheta < 170^\circ$. However, muon reconstruction is less efficient in the regions between two wheels of DTs ($|\eta| \sim 0.25$, $|\eta| \sim 0.8$) and in the transition region of DTs and CSCs ($|\eta| \sim 1.2$)

Muon Drift Tubes

DTs are placed around the cylindrical barrel region ($|\eta| < 1.2$), which has a uniform magnetic field. Altogether 250 DTs exist. They are organized in five wheels consisting of four layers each. Each of these DTs has an average size of 2 times 2.5 metres and consists of 12 aluminium layers. Each layer is built up of numerous tubes having an approximate diameter of 4 cm and containing a stretched wire inside a gaseous volume. Whenever a particle passes, electrons are knocked off the gas atoms and end up at the positively-charged wire. This yields an electric current and combined with the information of drift-time between impact and signal the y and z coordinates can be determined [16].

Cathode Strip Chambers

CSCs, which consist of both positively-charged wires and negatively-charged strips, are utilized in regions with inhomogeneous magnetic field [16]. In total, 468 CSCs

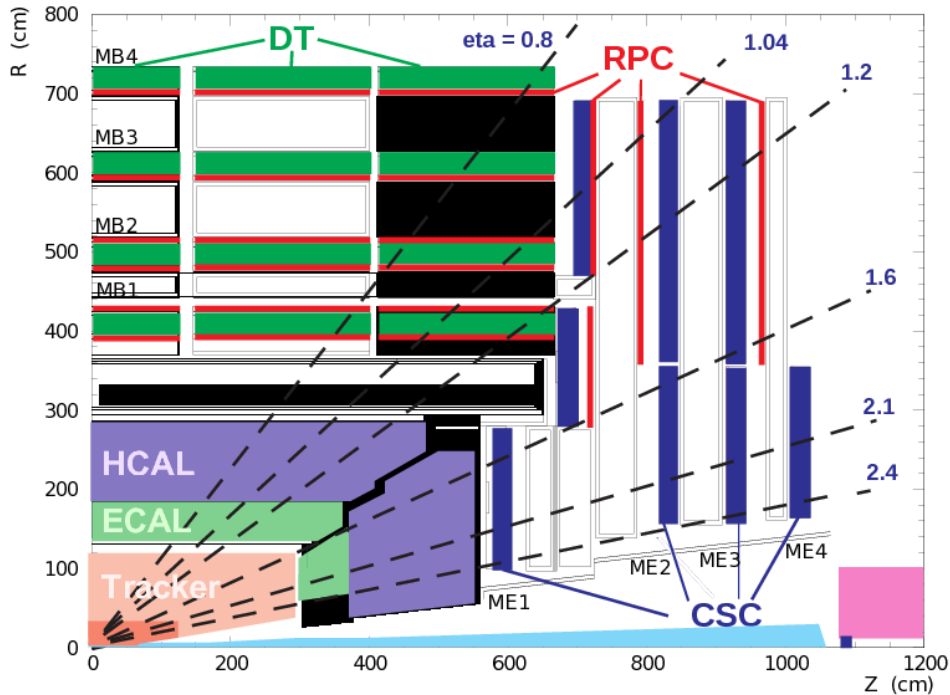


Figure 3.2: Layout of the muon systems [15].

are installed in four layers. In the overlap region of barrel and endcap ($0.9 < \eta < 1.2$) muons are detected by both - DTs and CSCs. Up to $|\eta| = 1.6$ RPCs support the CSCs to achieve better resolution of time and transverse momentum. CSCs consist of arrays of positively-charged wires crossed with negatively-charged copper strips within a gas volume. The functionality is similar to the one of DTs: Muons passing through the CSCs knock electrons off the gas atoms inside the chambers. While electrons move towards to the anode wires, positive ions move away from the wires towards the copper cathode. Because of perpendicular positioning of strips and wires a determination of x and y coordinates is possible.

Resistive Plate Chambers

RPCs are used in mid $|\eta|$ regions and consisting of two parallel plates, a positively-charged anode and a negatively-charged cathode filled with a gaseous volume in between. Muons passing through the gas cause electrons leaving the gas atoms resulting in an avalanche of electrons. The signal is picked up by metallic strips after a precisely known time delay. Due to the avalanche mode resistive plate chambers have a much faster response of about 1 ns than DTs or CSCs. The advantage of RPCs is an unambiguous identification of the correct particle bunch. The signal of RPCs is usually used to define the time when muons hit the DTs.

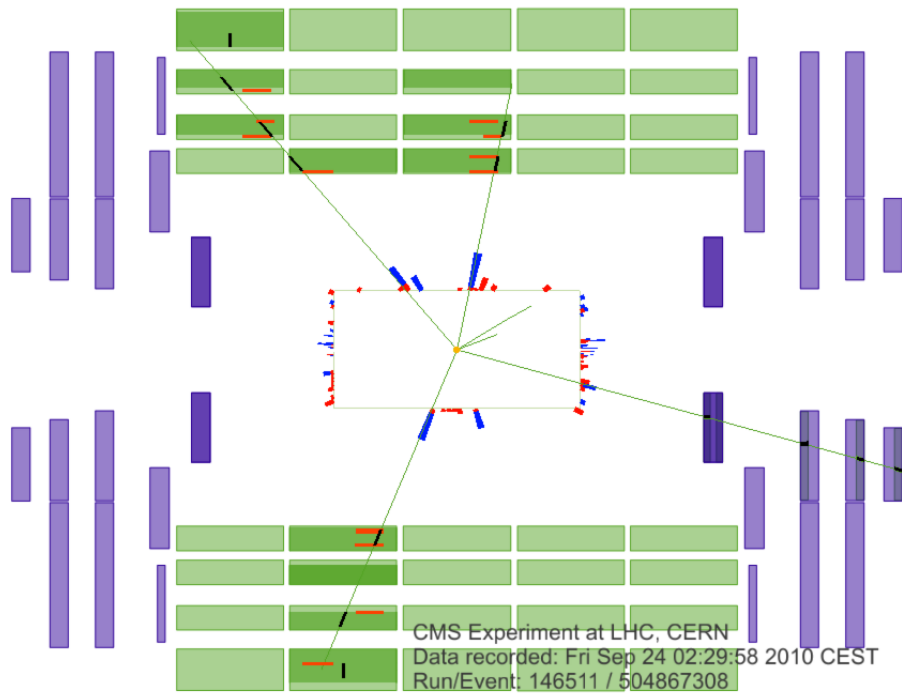


Figure 3.3: Example of four reconstructed muons [15].

3.2 Trigger system

At the design instantaneous luminosity of $10^{34} \text{ cm}^{-2}\text{s}^{-1}$ the LHC is constructed for one bunch collision (*bunch-crossing*) to happen every 25 ns corresponding to a frequency of 40 MHz. The amount of data resulting from one single crossing is approximately 1 megabyte and sums up to 40 terabytes of data per second. Hence, a stepwise reduction down to manageable rate of 100 Hz is required. During this reduction the loss of interesting events should be minimized. The process is called *triggering*. The layout of the trigger system is displayed in Fig. 3.4. Passing events are kept and stored in multiple locations all around the world (e.g. at the *Tier-2* in Vienna) and are analysed offline later. The CMS trigger system is a two-stage system consisting of hardware based *Level-1* (L1) and software based *High Level Triggers* (HLT). As an understanding of the trigger is important for the studies of the muon trigger efficiencies, the trigger system is discussed in detail below. Further information can be found in [10].

3.2.1 Level-1 Trigger

As first stage of the CMS trigger process the L1 trigger has to handle all events resulting in a *'keep or drop'* decision every 25 ns (time between two bunch-crossings). It is composed of a large number of custom made, fast electronics placed either

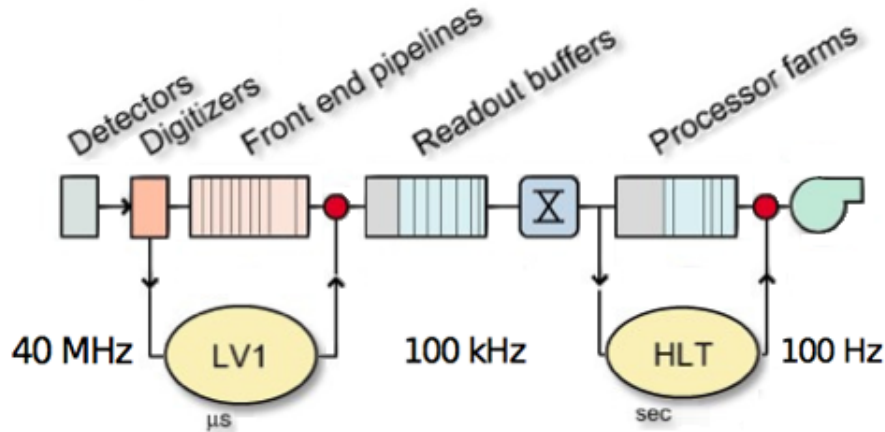


Figure 3.4: Different stages of the CMS triggering, starting at 40 MHz and ending at 100 Hz [17].

directly on the detector or due to radiation in the service caverns next to it. The decision whether an event is accepted or rejected at L1 is based on information coming from the muon chambers and the calorimeters. The structure of the decision is shown in Fig. 3.5. The *Global Muon Trigger* (GMT) uses the complementary information from the DTs, CSCs and RPCs. Additionally information coming from the calorimeters is passed to the *Global Calorimeter Trigger* (GCT).

Not involved in L1 triggering is the inner tracker, because that would require too much time for reconstruction. At last the signals of GMT and GCT are sent to the *Global trigger* (GT) making the final decision whether to keep or to reject an event. If the event fulfills all required criteria, the GT tells the data acquisition to transfer it to the HLT for further processing.

Every detector's response is stored in a buffer which holds the last 128 events. Therefore, as every 25 ns a new event is added, the maximal elapsing time for processing and returning the decision is limited to $3.2 \mu\text{s}$. All calculations are done with fast hardware using reprogrammable field-programmable gate arrays. The L1 trigger reduces the data rate from approximately 40 MHz to approximately 100 kHz.

Due to three different muon detectors, DT, CSC and RPC, a lot of complementary information is available. All of them share the information resulting from every event's original bunch-crossing. DTs and CSCs provide track segments; these informations are used and put together by so called *Track Finders* (see Fig. 3.5), whose purpose is the identification of possible muon candidates by means of using different segments of different muon stations and combining them. Furthermore, the muons are sorted by identifying their transverse momentum (p_T) and their quality. The combined information content of at most four (best) muon candidates is then sent to the GMT. On the other hand the RPCs exploits regional hit patterns

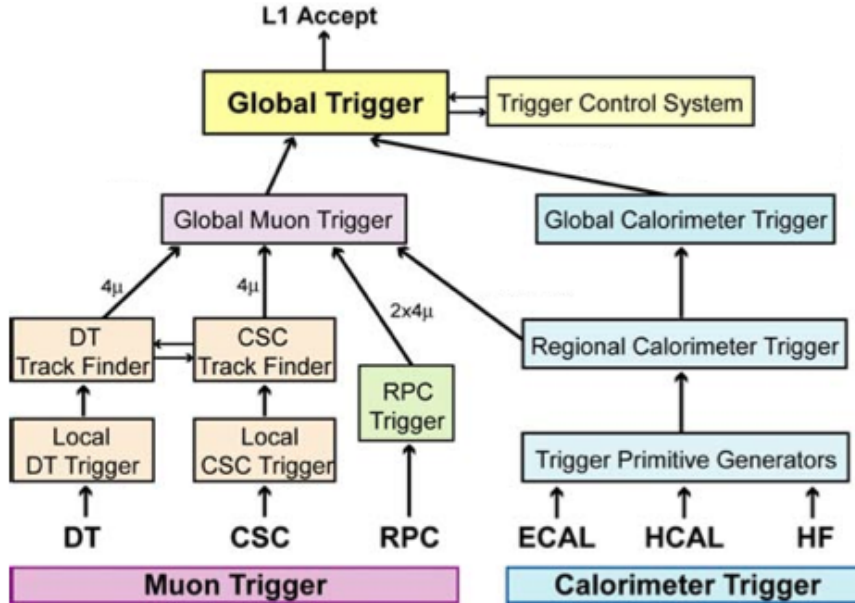


Figure 3.5: Structure of L1 trigger information flow [18].

and also send track candidates to the GMT. At this point the GMT has gained a lot of information coming from the three subsystems; important quantities are p_T , charge, pseudorapidity η , the azimuthal angle φ and a quantity representing the muon quality. Now a comparison of DT and CSC candidates on the one hand and RPC candidates on the other hand follows, providing both better selection criteria and due to merged kinematic parameters, also better momentum resolution and efficiency. Unmatched recorded candidates (for example having a match at the DTs and the CSCs, but not at RPCs) or duplicates are suppressed by the GMT. After another sorting by transverse momentum and quality, together with the information of the GCT, the muon candidates are sent to the GT, which takes the final decision whether to keep or reject an event. The GCT delivers various supplementary information about the presence of physical objects such as photons, electrons and jets as well as sums of transverse and missing energies.

3.2.2 High Level Trigger

The HLT consists of a single processor farm composed of commodity PCs, the event filter farm, which is able to conduct complex reconstruction and selection algorithms. Due to previous filtering made by L1 the incoming data is already reduced to 100 kHz and, thus, much more processing time of the order of 1 s is available. A very challenging aspect of the HLT is maximising the efficiency and keeping the CPU time acceptable at the same time. Each trigger path is a sequence

of reconstruction and sophisticated selection steps [19][20]. Since quarkonium triggers only use muons, the following section will mainly focus on the HLT muon reconstruction.

With L1 candidates as starting points the tracker information is additionally exploited. Tracking is sufficient for better reconstruction and an improved resolution of particles. For example, matching corresponding tracks to possible muon candidates greatly reduces the fake rate and substantially improves the momentum resolution. For muon reconstruction the HLT combines information from both, the muon and the tracker subdetectors, in order to identify muon candidates and determine their transverse momentum p_T . The HLT consists of two levels:

- Level-2 (L2) using information from the muon system only

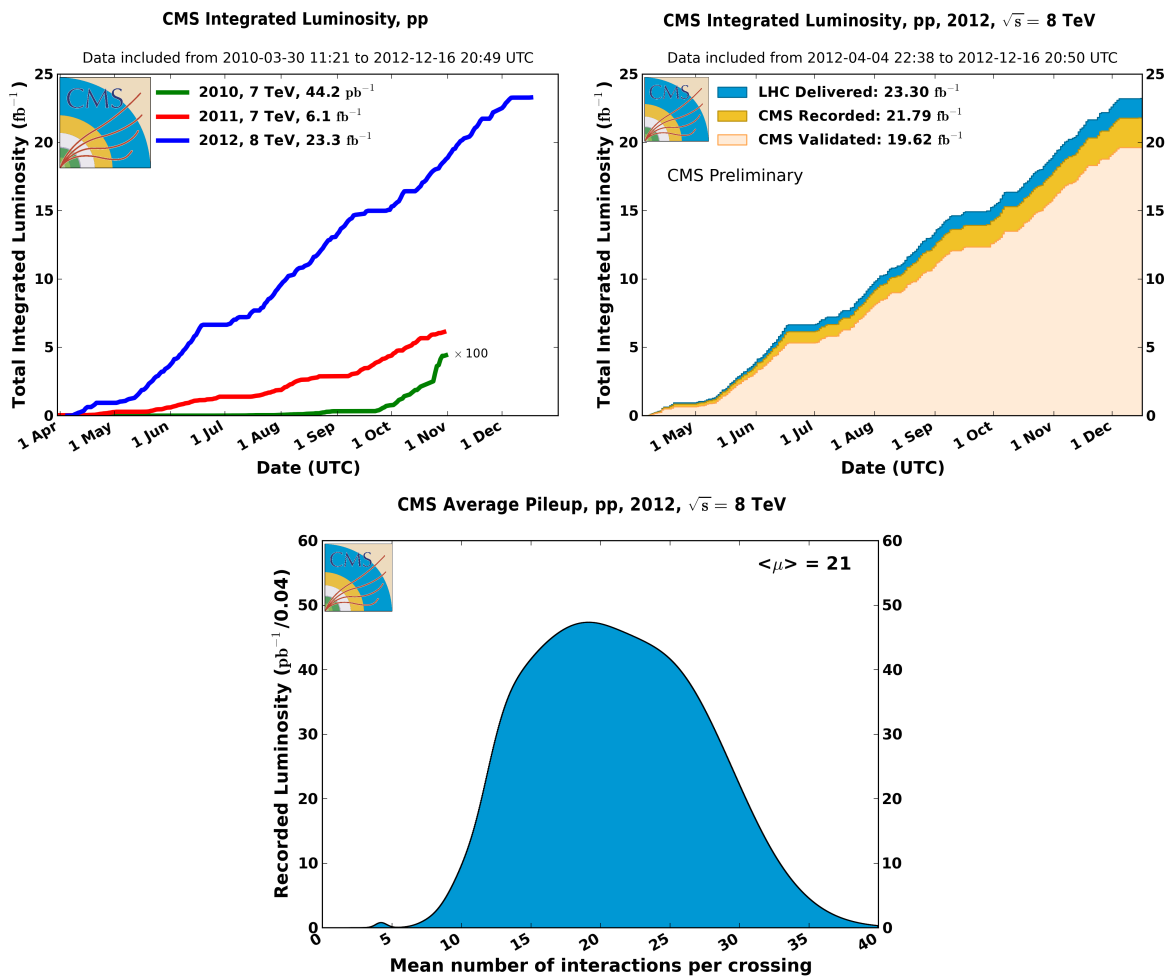
- Level-3 (L3) combining measurements from tracker and muon subdetectors.

In **L2** the reconstruction of tracks is based on the Kalman filter technique [21], a recursive and iterative algorithm performing pattern recognition and track fitting. Its basic idea is updating the parameters of the model at each measurement point by using the measurements themselves and the propagation of the parameters from previous iterations. Hence, both the detector error and deviations induced by physical processes on trajectories are taken into account. A track in the muon spectrometer built from patterns of DTs and CSCs (so called *seed*) is used as starting point of muon reconstruction. Basically each seed starts reconstructing a track by using all available measurements from the muon chambers. Possible duplicates of the same muon are removed by checking if their tracks share hits in different subdetectors. The beam spot region, which is the luminous center where protons collide, is used to constrain the tracking parameters in order to improve momentum resolution.

For **L3** muon reconstruction the additional information of the inner tracker is exploited. First, the tracker reconstruction is seeded using L2 information. Afterwards the track is reconstructed in the tracker and finally combined and fitted together with tracks of the muon systems. Three different seeding algorithms are available; each of them performs differently depending on the position of the particle in the detector. Hence, in order to optimise efficiency and timing, the fastest is used and is only followed by the second fastest one in case of failure. Reconstruction is again based on the Kalman filter technique. Reconstructed tracks and L2 muon candidates are propagated throughout the detector applying several filtering criteria, e.g. distances or directions; if a pair of compatible tracks is found a final refit over all tracker and muon systems is performed.

3.2.3 Performance of the CMS Detector

In the years of operation the LHC has continuously increased the integrated luminosity from 0.044 fb^{-1} in 2010 to 23.20 fb^{-1} in 2012 [22]. In 2012 the CMS detector reached a data taking efficiency of 93.5 percent at pp collisions with a center of mass energy of $\sqrt{s} = 8 \text{ TeV}$, corresponding to an integrated luminosity of 21.79 fb^{-1} . Furthermore, 90 percent of all data was validated, corresponding to 19.62 fb^{-1} . Also worth mentioning is the number of so called *pileup* events describing average numbers of pp collisions per bunch-crossing. The pileup evolution goes hand in hand with growing instantaneous luminosity and evolves from hardly any pileup events in 2010 to an average number of pileup events of 21 in 2012.



(c)

Figure 3.6: Integrated luminosities and pileup distribution recorded by the CMS detector in 2012 [23].

4 The Standard Model of Particle Physics

This chapter gives a short introduction to the standard model of particle physics. Furthermore, because of its importance for quarkonium physics quantum chromodynamics (QCD) is described briefly. For further reading [24][25] are recommended.

The standard model is based on the following theoretical assumptions:

- Homogeneity and isotropy of space, i.e. no direction is preferred.
- Validity of special relativity: The physical laws in two inertial systems which can be transformed by a Lorentz transformation are equal. The four dimensional space-time is described by the corresponding four-vectors. Furthermore, the speed of light is equal in all inertial systems corresponding to 299 792 458 meters per second.
- Validity of gauge symmetries: The strong interaction is based on a SU(3) and the electroweak interaction on a U(1) \times SU(2) gauge symmetry.
- Spontaneous symmetry breaking: The underlying process describing how a completely symmetric state ends up spontaneously in an asymmetric state.
- Validity of CPT invariance: The physical laws remain equal under charge conjugation ($q \rightarrow -q$), parity ($\vec{x} \rightarrow -\vec{x}$) and time ($t \rightarrow -t$) transformation. Parity violation was first observed by Chien-Shiung Wu in 1956 [26], charge and parity violation in 1964 by James Cronin, Val Fitch and others in the decays of neutral kaons [27], but there is no evidence for CPT violation yet.

By means of these axioms the standard model is able to describe the strong, the weak and the electromagnetic interactions. Weak and electromagnetic interactions can be combined to the electroweak one. However, up to now it is not possible to include gravity into the standard model, because there is no valid gauge theory for gravitation yet. Nevertheless, this implies no restriction for calculating high-energy processes, since the gravitational forces can easily be neglected for subatomic particles. The masses of leptons and quarks, the mass of the Higgs boson, the masses of the gauge bosons W^\pm and Z^0 , all coupling constants and the mixing angles are parameters of the standard model and cannot be derived from it. The photon and

the gluons have zero mass. Without spontaneous symmetry breaking, some particles (e.g. the W and Z bosons) would be predicted to be massless. To overcome this, spontaneous symmetry breaking is augmented by the Higgs mechanism, which also suggests the presence of the Higgs boson.

Although the standard model has been very successful throughout the last decades, there are still a lot of open questions which are not understood or answered yet:

- Free quarks cannot be observed due to color confinement. But the phenomenon of the confinement itself is not yet understood.
- Is there a possibility to unify the strong, the weak and the electromagnetic interactions in so called Grand Unified Theories (**GUTs**)? So far, only the electromagnetic and the weak interactions could be unified to the electroweak interaction with a universal coupling constant.
- Gravity cannot be described within the standard model. Many theorists still believe that a unification of all forces can be done and therefore, several theories have evolved in recent years.
- Why is the number of lepton and quark generations exactly 3?
 $\begin{pmatrix} u \\ d \end{pmatrix}, \begin{pmatrix} c \\ s \end{pmatrix}, \begin{pmatrix} t \\ b \end{pmatrix},$ and $\begin{pmatrix} e^- \\ \nu_e \end{pmatrix}, \begin{pmatrix} \mu^- \\ \nu_\mu \end{pmatrix}, \begin{pmatrix} \tau^- \\ \nu_\tau \end{pmatrix}.$
Is it coincidence or are yet unknown principles behind?
- What is dark energy and dark matter? Dark matter is a kind of matter hypothesized to describe gravitational effects that appear to be the result of invisible mass. Dark energy on the other hand is a hypothetical form of energy which permeates all of space and tends to accelerate the universe.
- Why does nature prefer left handed helicity particles? In particle physics, helicity is the projection of the spin \vec{S} onto the direction of the momentum.

4.1 Particles of the Standard Model

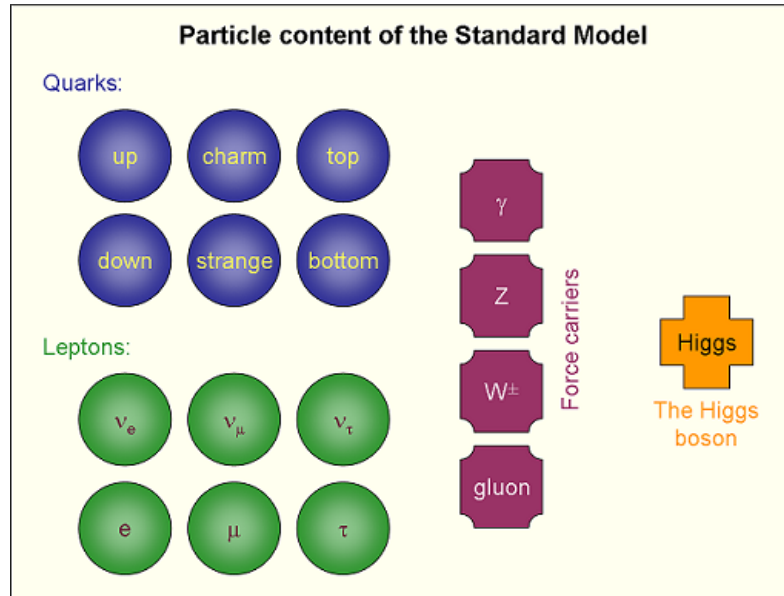


Figure 4.1: Particles of the standard model [28].

The standard model consists of the following elementary particles (Fig. 4.1), which have mostly been predicted and discovered throughout the last century (Fig. 4.2):

- **Fermions** have half-integer spin and, thus, obey the Pauli exclusion principle. In the standard model, the two fundamental groups are on the one hand leptons, which do not undergo the strong interaction, and on the other hand quarks, which themselves form either mesons (consisting of two quarks) or hadrons (consisting of three quarks). The 3 lepton generations are the electron (e), the muon (μ) and the tau (τ) and their respective neutrinos. The three quark generations contain the up and down quarks, the charm and strange quarks and the top and bottom quarks.
- **Gauge bosons** are particles with spin 1, through which the four fundamental forces are propagated. While gravitation and electromagnetism have infinite range, the weak interaction is limited to 10^{-3} fm due to the high masses of their gauge bosons W^\pm and Z^0 . The strong interaction has a range of 1.5 fm due to quark confinement. Photons are the massless gauge bosons of the electromagnetic interaction and gluons are the gauge bosons of the strong interaction.
- **The Higgs boson** is the smallest excitation of the Higgs field which is responsible for giving mass to the W and Z bosons. Its existence was finally

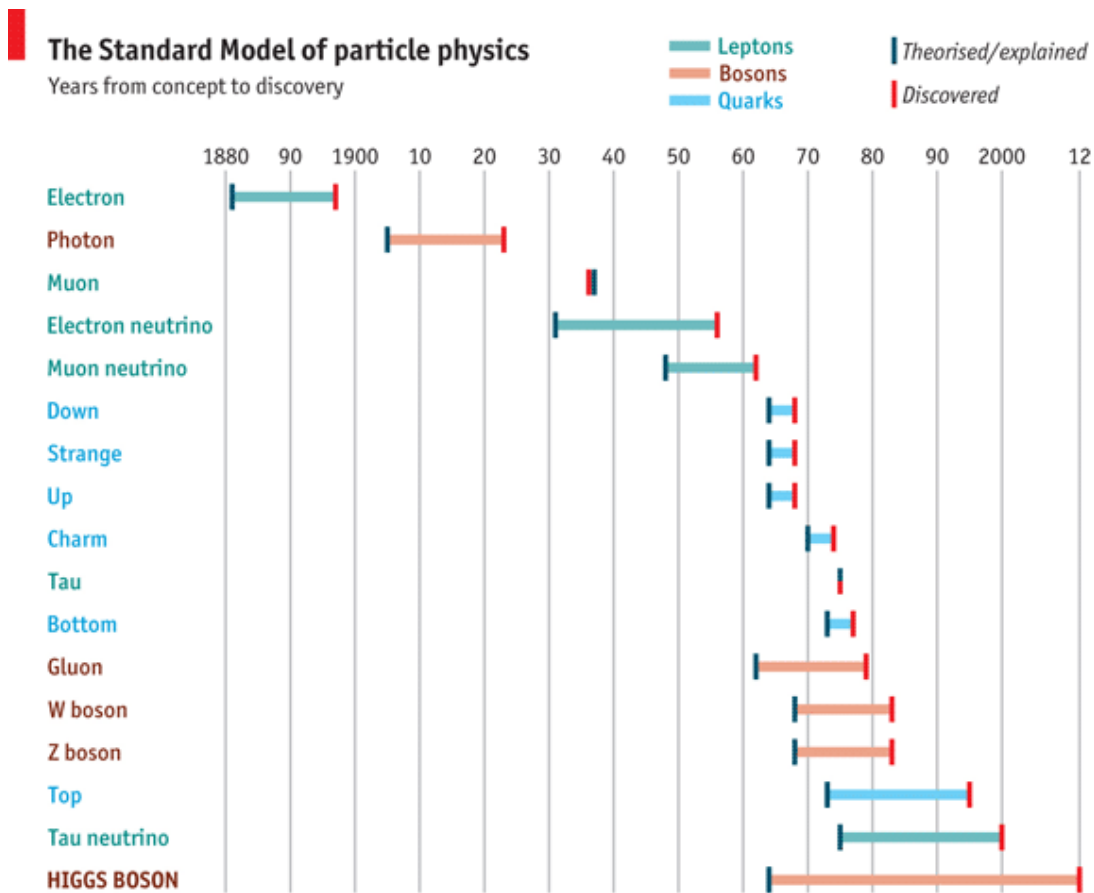


Figure 4.2: Prediction and discovery of important particles involved in the standard model [29].

confirmed nearly 50 years after it was proposed at the LHC in 2012 [7][8] with a mass of about $\sim 125\text{GeV}$, positive parity and zero spin [30]. Due to its extremely short lifetime, the Higgs particle decays far too quickly and therefore only its decay products can be detected.

4.2 Important Mathematical Concepts

The standard model of particle physics is based on Lorentz covariant field theories yielding equations which are invariant under linear Lorentz transformations. Taking into account the Lagrangian formalism of classical mechanics [31], the Euler-Lagrange equations are used to get the equations of motion out of the four dimensional, Lorentz invariant Lagrangian densities. The Lagrangian density has the form

$$\mathcal{L} = \mathcal{L}(\phi, \partial_\mu \phi), \quad (4.1)$$

with a field $\phi = \phi(x^\mu)$ and its derivative $\partial_\mu \phi$ at x^μ . x^μ is a four dimensional point in space time. The Lagrangian density just depends on the field and its derivation at each point in space time (*local field theory*). Applying the Euler-Lagrange equations to $\mathcal{L}(\phi, \partial_\mu \phi)$ yields the general field equations:

$$\frac{\partial \mathcal{L}}{\partial \phi} - \partial_\mu \left(\frac{\partial \mathcal{L}}{\partial (\partial_\mu \phi)} \right) = 0 \quad (4.2)$$

The Lagrangian density of a free fermion $\Psi(\mathbf{r}, t)$ is written as

$$\mathcal{L} = \hbar c \bar{\Psi} (i\gamma^\mu \partial_\mu - \kappa) \Psi, \quad (4.3)$$

where $\partial^\mu = \frac{\partial}{\partial x_\mu}$ equals $\left(\frac{1}{c} \frac{\partial}{\partial t}, -\nabla\right)$, κ equals $\frac{mc}{\hbar}$, c stands for the speed of light and γ_μ stands for one of the four Dirac matrices.

Variation with respect to $\bar{\Psi}$ ($= \Psi^\dagger \gamma^0$) yields the covariant Dirac equation:

$$(i\gamma_\mu \partial^\mu - \kappa) \Psi(x) = 0 \quad (4.4)$$

The demand of *local gauge invariance* leads to the embedding of interactions between particles and fields into the Dirac equation. This concept is well known throughout different fields in physics starting from classical mechanics. It states that the Lagrangian and, thus, all physical equations are invariant under a continuous group of local transformations. A phase transition has an impact on the Dirac equation of a free particle

$$\Psi'(x) = \exp(iq\Lambda(x))\Psi(x) = \hat{U}(q)\Psi(x), \quad (4.5)$$

where $\Lambda(x)$ is a continuous differentiable function and q an arbitrary parameter. To ensure unchanging physical properties, the Dirac equation is extended in the following way:

$$\{\gamma^\mu (i\partial_\mu - qB_\mu) - \kappa\} \Psi(x) = 0 \quad (4.6)$$

In this equation B_μ describes the field that the Dirac fermion is coupled to while q refers to the coupling (e.g. electric charge in the case of coupling to an electromagnetic field).

4.3 Quantum Chromodynamics (QCD) - the Theory of the Strong Interaction

This section discusses fundamental ideas of QCD which is the theory of the strong interaction. For further reading [32][25] are recommended.

After James Chadwick discovered the neutron in 1932 [33] and showed that nuclei consist not only of protons, a lot of physicists tried to solve the problem of nuclear forces. A first important step was made by the idea of Hideki Yukawa [34], who suggested to understand proton-neutron interactions in terms of an exchange of quantum particles based on Enrico Fermi's thesis showing that the Coulomb force is generated by exchange of photons [35]. Yukawa introduced a field of force between the nucleons, whose exchange particles were later recognized as mesons. Significant influence on the understanding of nuclear forces came through the independently developed quark models by Murray Gell-Mann and George Zweig [36][37] explaining nucleons as bound states of three quarks. The proton-neutron interaction inside nuclei could be seen as a residual force of not completely shielded quarks. The quark model made it possible to achieve structural order throughout all hadrons and mesons.

Probably the first indication that quarks should possess an additional quantum number was made in connection with the Ω^- baryon [38], which consists of three strange quarks with parallel, half-integer spin. Therefore, the flavor, the spatial and the spin parts of the wave function are completely symmetric, which is strictly forbidden by the Pauli exclusion principle. In order to circumvent this problem, an additional degree of freedom was introduced, the *color charge* ($|r\rangle$, $|g\rangle$ and $|b\rangle$), which is a color-like property that inspired the name quantum *chromodynamics* for the theory of the strong interaction.

The Lagrangian of QCD consists of a quark and a gluon part and is given as

$$\mathcal{L}_{QCD} = \underbrace{\sum_{f=1}^6 \bar{\mathbf{f}}_f i\gamma^\mu (\partial_\mu + ig\mathbf{G}_\mu) \mathbf{f}_f - m_f \bar{\mathbf{f}}_f \mathbf{f}_f}_{\mathcal{L}_{quark}} - \underbrace{\frac{1}{2} \text{tr}[\mathbf{G}_{\mu\nu} \mathbf{G}^{\mu\nu}]}_{\mathcal{L}_{gluon}}. \quad (4.7)$$

\mathcal{L}_{quark} , which stands for the Lagrangian density of the quarks, includes a summation of all quark flavors f (u, d, c, s, t, b), a summation of the three color types and a summation of the Dirac indices. The states of a single quark are described by a three-component vector

$$\mathbf{f} = \begin{pmatrix} f_r \\ f_g \\ f_b \end{pmatrix}, \quad (4.8)$$

where f_r , f_g and f_b are four-component Dirac spinors. \mathbf{G}_μ represents the 8-component

gauge field. The coupling between a Dirac fermion and this field occurs in analogy to Eq. 4.6.

\mathcal{L}_{gluon} is the tensor product of two gluon field strength tensors, which are akin to the electromagnetic tensor $F^{\mu\nu} = \partial^\mu A^\nu - \partial^\nu A^\mu$:

$$\mathbf{G}_{\mu\nu} = D_\mu \mathbf{G}_\nu - D_\nu \mathbf{G}_\mu = \partial_\mu \mathbf{G}_\nu - \partial_\nu \mathbf{G}_\mu + ig[\mathbf{G}_\mu, \mathbf{G}_\nu]. \quad (4.9)$$

In contrast to electrodynamics, the last term $[\mathbf{G}_\mu, \mathbf{G}_\nu]$ does not vanish because the gauge fields \mathbf{G}_μ and \mathbf{G}_ν do not commute. This aspect reveals the non-abelian character of QCD and leads to the self-interaction of the gluon fields and, thus, the peculiarity of gluons being sources of their own fields.

The main properties of QCD can be summarized as follows:

- Physical states are color neutral hadrons. Two quarks can form a meson ($\bar{q}q$) and three quarks can form a baryon (qqq or $\bar{q}\bar{q}\bar{q}$). Other bound states have not been observed in nature yet, but cannot be excluded either.
- QCD is invariant under U(1) transformations, which can be parametrized by a single rotation angle, yielding flavor conservation.
- Similar to quantum electrodynamics (QED), QCD has a running coupling constant

$$\alpha_s(k^2) \sim \frac{1}{\ln(\frac{k^2}{\Lambda_{QCD}^2})}, \quad (4.10)$$

where k stands for the energy transfer and Λ_{QCD} is the *characteristic energy scale* of QCD ($\Lambda_{QCD} \sim 10^2$ MeV). At low energy scales and large distances α_s exceeds 1, leading to the phenomenon of quark confinement. The force between particles undergoing strong interactions becomes stronger the larger their distance gets, resulting in the phenomenon that no single quark has yet been observed and will ever be observed if quark confinement is true. It also causes problems to determine cross sections or other observables because perturbative calculations cannot be applied.

- In contrast to quark confinement, for large momentum transfer and small distances α_s decreases, resulting in the so called *asymptotic freedom*, a scenario of quarks and gluons interacting very weakly. For $\alpha_s \ll 1$, perturbative calculations can be conducted, but for increasing α_s perturbative methods are no longer valid.

5 Quarkonium Physics

5.1 The Quarkonium Spectrum

In high energy physics the name *quarkonium* (pl. *quarkonia*) designates a bound state of a quark and its anti-quark. Of particular physical relevance are the quarkonium states of the charm quark ($c\bar{c}$), called *charmonium*, and of the bottom quark ($b\bar{b}$), called *bottomonium*. Because of its high mass the top quark decays faster than the formation of a bound state would take and, thus, a proof of its existence has not been found. The three light quarks (up, down, strange) could also form bound quarkonium states, but, due to their tiny masses, the states actually seen in experiments are a mixture of different light quarks. Up to the 1970's, only the up, down and strange quarks were known. In 1970, Glashow, Iliopoulos and Maiani introduced a new mechanism describing the suppression of flavor-changing neutral currents. This so called GIM (Glashow–Iliopoulos–Maiani [39]) mechanism predicted a fourth quark, the charm quark. For a short time, this prediction seemed to remain unheeded, until in 1974, the first quarkonium state to be discovered (by two independent groups led by Burton Richter and Samuel Ting [40] [41]) was the J/ψ meson consisting of a charm and an anti-charm quark (shown in Fig. 5.1). This discovery did not only confirm the validity of the GIM mechanism, it also opened a new field in physics – *quarkonium physics*.

In 1963, N. Cabibbo suggested a mixing angle Θ_C to preserve the concept of universality in weak interactions. The mixing angle Θ_C is related to the probability of down and strange quarks decaying into up quarks [42]. Since in 1964 evidence of CP violation was found in neutral kaon decays [43] implying that more than two generations exist, the Cabibbo theorem was extended by Kobayashi and Maskawa in 1973: The CKM matrix was postulated [44].

This matrix contains informations on the strength of flavor-changing weak decays in a way that it specifies the mismatch of quantum states between free propagation and weak interaction. Furthermore, another consequence of the CKM matrix was the postulation of a third generation of quarks. The discovery of the $\Upsilon(1S)$ (pronounced *Upsilon*) meson at Fermilab in 1976 [45] confirmed the third generation that was postulated by Kobayashi and Maskawa. The $\Upsilon(1S)$ meson is a bound state of the bottom quark and its anti-quark with a mass of approximately 9.4 GeV.

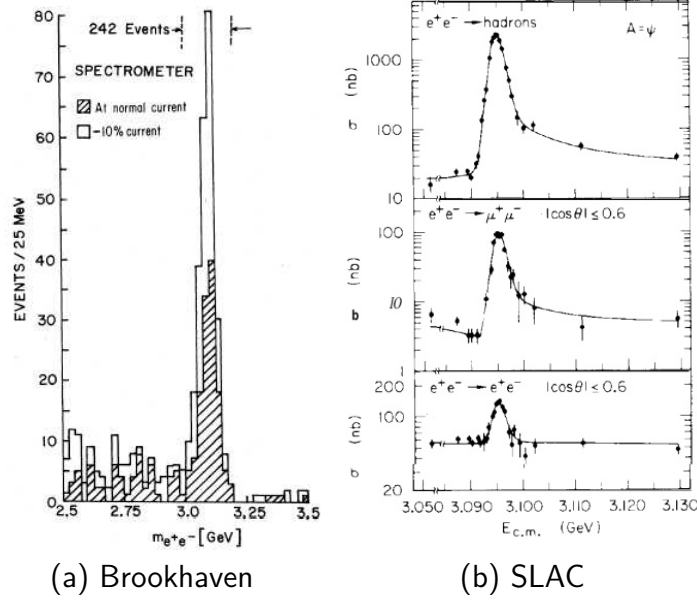


Figure 5.1: First observation of the J/ψ resonance: (a) at Brookhaven in a fixed target experiment using $p+\text{Be}$ collisions, (b) at the Stanford Linear Collider in e^+e^- collisions with J/ψ decaying into a multi-hadron state (top), into $\mu^+\mu^-$ (middle) and e^+e^- final states (bottom).

In the following years a number of excited charmonium and bottomonium states has been found. These states have different invariant masses and can decay mostly via radiative transitions into a lower energetic state. The charmonium spectrum is depicted in Fig. 5.2 while Fig. 5.3 shows the equivalent spectrum for the bottomonium case. Both figures visualize the *feed-down* contributions of higher energetic P wave states to the 1S ground state. Feed-down is an important subject in quarkonium studies and can influence the results considerably if not understood properly. Furthermore, one has to distinguish between prompt and non-prompt mesons. While prompt mesons are directly produced mesons plus feed-down contributions, non-prompt mesons mostly arise from the decay of B hadrons. Quarkonium states can be characterized through the schematic representation

$$n^{2S+1}L_J, \quad (5.1)$$

where n is the principal quantum number, S the spin angular momentum, L the orbital angular momentum and J the total angular momentum. Another frequently used notation is

$$J^{PC}, \quad (5.2)$$

which specifies a quarkonium state by quoting its total angular momentum J , its parity P and its charge conjugation C .

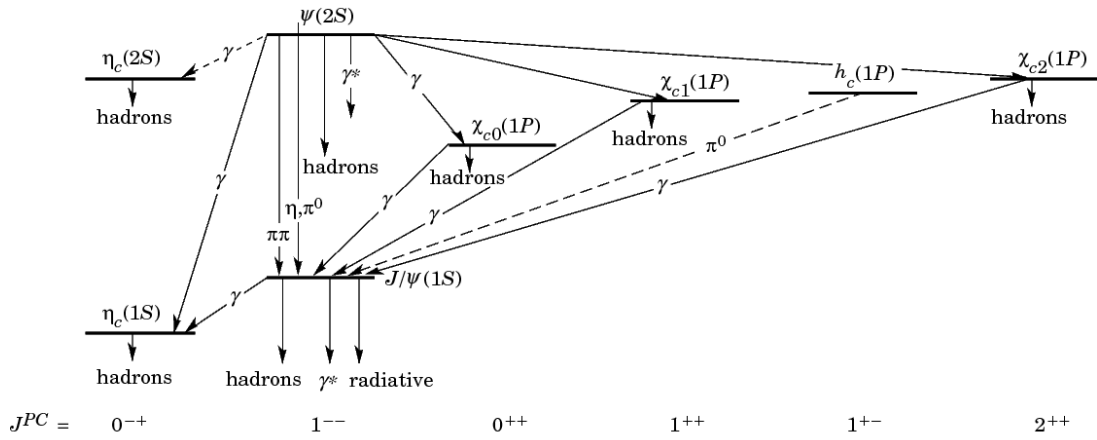


Figure 5.2: Charmonium spectrum [46]

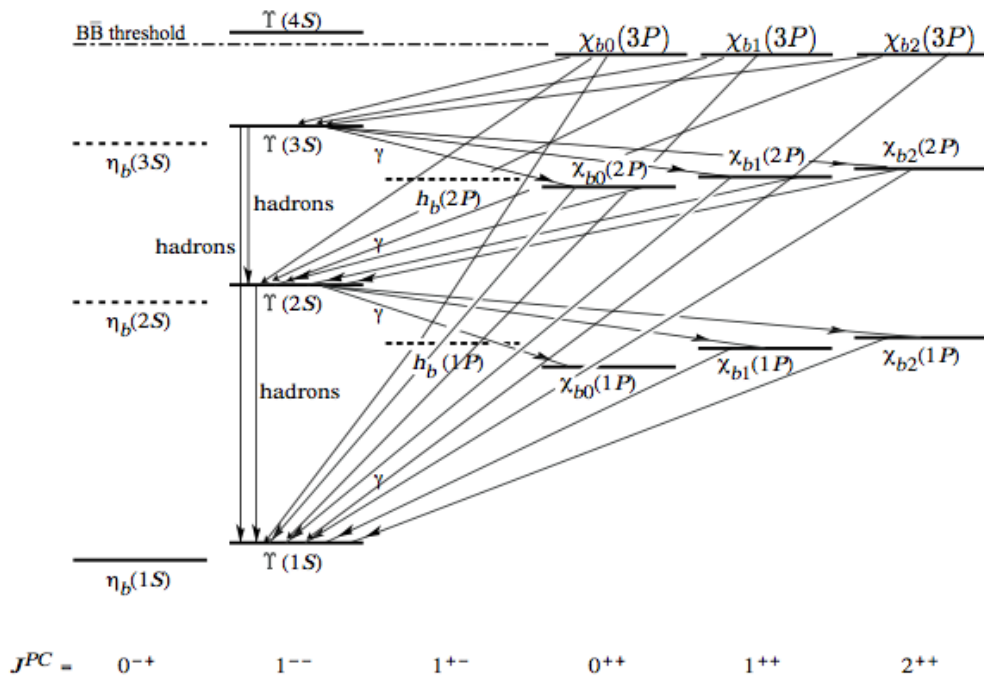


Figure 5.3: Bottomonium spectrum [46]

The properties of the most important charmonium and bottomonium mesons are summarized in Tab. 5.1 and Tab. 5.2, respectively. The $\chi_b(3P)$ system, centered at a mass of 10.530 ± 0.005 (stat.) ± 0.009 (syst.) GeV, has only been recently discovered [47] and added to the system.

Name	Mass [MeV/c^2]	J^{PC}	$n^{(2S+1)}L_J$
J/ψ	3096.9 ± 0.01	1^{--}	1^3S_1
χ_{c0}	3414.75 ± 0.31	0^{++}	1^3P_0
χ_{c1}	3510.66 ± 0.07	1^{++}	1^3P_1
χ_{c2}	3556.2 ± 0.09	2^{++}	1^3P_2
ψ'	3686.09 ± 0.05	1^{--}	2^3S_1

Table 5.1: Properties of the charmonium meson family [46].

Name	Mass [MeV/c^2]	J^{PC}	$n^{(2S+1)}L_J$
$\Upsilon(1S)$	9460.3 ± 0.26	1^{--}	1^3S_1
$\chi_{b0}(1P)$	9859.44 ± 0.42	0^{++}	1^3P_0
$\chi_{b1}(1P)$	9892.78 ± 0.26	1^{++}	1^3P_1
$\chi_{b2}(1P)$	9912.21 ± 0.26	2^{++}	1^3P_2
$\Upsilon(2S)$	10023 ± 0.31	1^{--}	2^3S_1
$\chi_{b0}(2P)$	10232.5 ± 0.4	0^{++}	2^3P_0
$\chi_{b1}(2P)$	10255.46 ± 0.22	1^{++}	2^3P_1
$\chi_{b2}(2P)$	10268.65 ± 0.22	2^{++}	2^3P_2
$\Upsilon(3S)$	10355.2 ± 0.5	1^{--}	3^3S_1
$\chi_b(3P)$	10530 ± 5	0^{++}	3^3P_0

Table 5.2: Properties of the bottomonium meson family [46].

5.1.1 Quarkonia as Tool to Understand Strong Interactions

The forces inside a nucleus arising from the strong interaction are by far the strongest of the four fundamental forces. Nevertheless, the theory of strong interactions is poorly understood and raises a lot of questions (Chap. 4). Two important fields using the means of quarkonium states and quarkonium physics are briefly introduced:

- QCD predicts that if the “temperature“ of nuclear matter increases above a certain threshold, strongly interacting matter (quarks, gluons) undergoes a phase transition. The resulting new state is referred to as quark-gluon plasma (QGP), a hot and dense phase of deconfined quarks and gluons. This phase

transition from color-neutral hadrons to color-charged hadrons implies that the degrees of freedom change. Since the late 1980's, due to the seminal work of Tetsuo Matsui and Helmut Satz [48], heavy-ion collisions are considered to very likely produce QGP at high temperatures. The original idea suggests that quarkonia can survive this phase transition due to their small sizes. Hence, quarkonium states start to move through the emerging QGP but, due to color screening and other phenomena, they start to “melt“. This melting manifests itself as the suppression of quarkonia production in heavy-ion collisions, compared to the quarkonium production in pp collisions. Melting of quarkonia at high temperatures is therefore a strong sign of QGP. As different states have different masses and most importantly, different binding energies, screening and dissociation in the QGP happens at various temperatures. The first sign of QGP in CMS was observed in 2011 when the collaboration measured a dramatic difference in the number of $\Upsilon(2S)$ and $\Upsilon(3S)$ states produced in heavy-ion collisions and pp collisions. CMS measured the relative production in heavy-ion collisions to be only about 30% of the comparative rates in pp collisions [49].

- Similar to the e^+e^- bound state, which is considered to be the simplest object to study the electrostatic Coulomb force described by quantum electrodynamics (QED), in a way $c\bar{c}$ and $b\bar{b}$ are analogue objects for a detailed study of the strong interaction described by QCD. Despite very different mass ranges and underlying physics, both spectra show quite a few similarities. Therefore, quarkonia are a suitable system to precisely determine QCD parameters such as the strong coupling constant α_s [50].

5.2 Underlying Physics of Quarkonium Production

The following section gives a short overview of the underlying theoretical concepts of quarkonium production, encountered problems and experimental results. References [50][51] are recommended for further reading. The fundamental idea of all quarkonium production considerations is the factorization theorem.

When heavy quarkonia are produced in hard-scattering processes, a large energy-momentum transfer usually takes place. The masses of the heavy charm and bottom quarks are much larger than Λ_{QCD} . The transverse momentum p_T can also exceed Λ_{QCD} . The associated values of the QCD running coupling constant are much smaller than 1 ($\alpha_s(m_c) \sim 0.25$ and $\alpha_s(m_b) \sim 0.18$) [50]. The production of the quarkonium states therefore happens at very different scales:

1. Short distance: The production of the initial quark-antiquark pair.

2. Long distance: The transition of the initial pair into a bound state.

While the first process can be described by the means of perturbative QCD calculations (high momentum, short distances) the second step involves inherently non-perturbative physics (lower momentum, larger distances). In order to apply well known perturbative methods to *short-distance* contributions with high momentum, *short-distance* and *long-distance* elements have to be separated. This splitting of the quarkonium production in short and long distance processes is called *factorization*. Non-perturbative elements have been discussed extensively over the recent decades and different treatments have led to various theoretical models. The most important models are the *CSM* (color-singlet model), the *CEM* (color-evaporation model) and the *NRQCD* (non relativistic quantum chromodynamics) factorization approach.

5.2.1 The NRQCD Factorization Approach

The NRQCD factorization approach was first introduced in 1995 by Bodwin, Braaten and Lepage [52]. It contemplates the wide range of energy scales in certain quarkonium states:

1. m , the heavy quark mass;
2. mv , the typical heavy quark momentum;
3. mv^2 , the typical heavy quark kinetic and binding energies.

In this context, v is the heavy quark velocity, which commonly takes the values $v \sim 0.3c$ for charmonium and $v \sim 0.1c$ for bottomonium bound states. The inclusive cross section for producing a certain quarkonium state H at large momentum transfer (p_T) can be written as

$$\sigma(H) = \sum_n F[Q\bar{Q}(n)] \langle 0 | \mathcal{O}^H(n) | 0 \rangle . \quad (5.3)$$

$F[Q\bar{Q}(n)]$ are the *short distance* coefficients (SDC) with a characterizing energy cut-off Λ ($\sim m$). For processes with $p < \Lambda$ the theory produces full QCD. The summation is done over all $Q\bar{Q}$ states n ,

$$n = {}^{2S+1} L_J^{[c]}, \quad (5.4)$$

where $[c]$ stands for the color multiplicity. The $\langle 0 | \mathcal{O}_n^H | 0 \rangle$ are vacuum expectation values, representing the *long distance* matrix elements (LDME) and describing the probability of a $Q\bar{Q}$ pair to evolve into a heavy quarkonium state. The LDMEs are non-perturbative, but they are conjectured to be universal (process independent).

They are written as matrix elements of four-fermion operators with a projection onto an intermediate state of the quarkonium H plus anything:

$$\mathcal{O}^H(n) = \langle 0 | \chi^\dagger \kappa_n \Psi \left(\sum_X |H + X\rangle \langle H + X| \right) \Psi^\dagger \kappa'_n \chi | 0 \rangle \quad (5.5)$$

where Ψ and χ are individual wave functions of the $Q\bar{Q}$ pair and κ_n, κ'_n are combinations of Pauli and color matrices. For example, the first two color-octet and color-singlet states read:

$$\mathcal{O}_1^H(^1S_0) = \langle 0 | \chi^\dagger \Psi \left(\sum_X |H + X\rangle \langle H + X| \right) \Psi^\dagger \chi | 0 \rangle \quad (5.6)$$

$$\mathcal{O}_1^H(^3S_1) = \langle 0 | \chi^\dagger \boldsymbol{\sigma} \Psi \left(\sum_X |H + X\rangle \langle H + X| \right) \Psi^\dagger \boldsymbol{\sigma} \chi | 0 \rangle \quad (5.7)$$

$$\mathcal{O}_8^H(^1S_0) = \langle 0 | \chi^\dagger J^a \Psi \left(\sum_X |H + X\rangle \langle H + X| \right) \Psi^\dagger J^a \chi | 0 \rangle \quad (5.8)$$

$$\mathcal{O}_8^H(^3S_1) = \langle 0 | \chi^\dagger J^a \boldsymbol{\sigma} \Psi \left(\sum_X |H + X\rangle \langle H + X| \right) \Psi^\dagger \boldsymbol{\sigma} J^a \chi | 0 \rangle \quad (5.9)$$

Equations 5.6-5.9 reveal that the quarkonium evolves from both the color singlet and the color octet state. J^a represent the 8 generator matrices of the color $SU(3)$ group and $\boldsymbol{\sigma}$ are the Pauli matrices. In contrast to the CSM, quarkonium can be produced through both color-octet and color-singlet $Q\bar{Q}$ states in the NRQCD factorization approach. While color-singlet production LDMEs are simply related to color-singlet decay LDMEs, color-octet LDMEs have to be determined from phenomenology. Because of these appearing color-octet states, unlike the CSM and the CEM, the NRQCD factorization approach depends on an infinite number of unknown matrix elements. Nevertheless, the sum of Eq. 5.3 can be organized as an expansion in powers of v and powers of α_s . In order to describe phenomenological applications, the expansion is truncated at a fixed order in v and, thus, only a few matrix elements need to be considered. The predictive power depends on the validity of such a truncation. If all color-octet contributions are dropped, the remaining contributions equal the CSM. Additionally, one should mention that the NRQCD factorization approach is believed to only hold true for large values of $\frac{p_T}{M}$.

5.2.2 Color-Singlet Model

The CSM assumes that the quarkonium state is produced from a color-singlet state with the same quantum numbers as the initial state. The CSM was postulated shortly after the discovery of the J/ψ meson [53] and was considered valid until

cross section measurements at the CDF (Collider Detector at Fermilab) showed discrepancies of more than one order of magnitude. The CSM predictions had clearly underestimated differential cross sections in higher p_T regions. Recent theoretical developments show that the next-to-leading order (NLO) and next-to-next-to leading order (NNLO) terms of the Taylor expansion in α_s are large contrary to what was assumed before. As explained in Sec. 4.3 the running coupling constant of QCD reveals a dependency of $\alpha_s(k^2) \sim \left(\ln\left(\frac{k^2}{\Lambda_{QCD}^2}\right)\right)^{-1}$ on the energy transfer $\Delta E = k$. For $k \gg \Lambda_{QCD}$, corresponding to large p_T , higher order corrections of α_s are not negligible. The expansion in α_s might therefore not converge, but instead yield even larger corrections. Furthermore, the CSM is already known to be inconsistent in describing production and decay of P-wave and higher angular-momentum states [50].

5.2.3 Color-Evaporation Model

The CEM was first proposed in 1977 [54]. It states that the probability of forming a specific $Q\bar{Q}$ state can be assumed to be independent of the color of any quark pair. Some predictions even claim a spin independent mechanism. In the CEM the cross section of producing a certain quarkonium state H is some fraction of the CEM parameter F_H . F_H is defined as the probability of a $Q\bar{Q}$ pair with a mass less than $2m_M$ evolving into a quarkonium H. Thereby, m_M stands for the lightest meson containing Q. F_H is assumed to be zero if the $Q\bar{Q}$ mass exceeds $2m_M$. When two quarks are close, they exchange gluons and create a very strong color field which binds the quarks together. In contrast to the upper mass limit, the quarkonium production is independent of the color of the quarks since the original color is neutralized due to the interaction of the quarks with the induced color field (*color evaporation*). Under the invariant mass threshold $2m_M$, the $Q\bar{Q}$ pair can either produce heavy-flavor hadrons by obtaining the additional energy from the non-perturbative color field or form a quarkonium bound state. Hence, summarizing all fractions F_H usually yields values less than unity. These fractions are considered to be universal and can be used to predict cross sections in other processes or kinematic regions. In [55], the CEM and the NRQCD factorization approaches have been compared by fitting CDF data taken at Fermilab for J/ψ , $\psi(2S)$ and χ_c production at $\sqrt{s} = 1.8$ TeV. The quality of the resulting fits for the CEM is rather poor compared to the NRQCD factorization approach.

5.2.4 Theoretical models compared to experimental data

The three theoretical models described above give very different predictions for quarkonium production cross sections. Figure 5.4 shows the NRQCD prediction for the cross section of the J/ψ and $\Upsilon(1S)$ decaying into $\mu^+\mu^-$ in comparison to

the cross section measured by CDF at Fermilab in 1997 [56][57]. Not only the total cross section, but also the color-singlet and color-octet contributions are shown. The color-singlet contribution at LO alone is not able to describe the experimental results. Including leading color-octet contributions and adjusting non-perturbative parameters to fit the data yields substantial improvement. At large p_T , higher order terms may become more important than lower orders. Because of $v \sim 0.1c$, higher orders are less significant in case of the bottomonium states compared to the charmonium states.

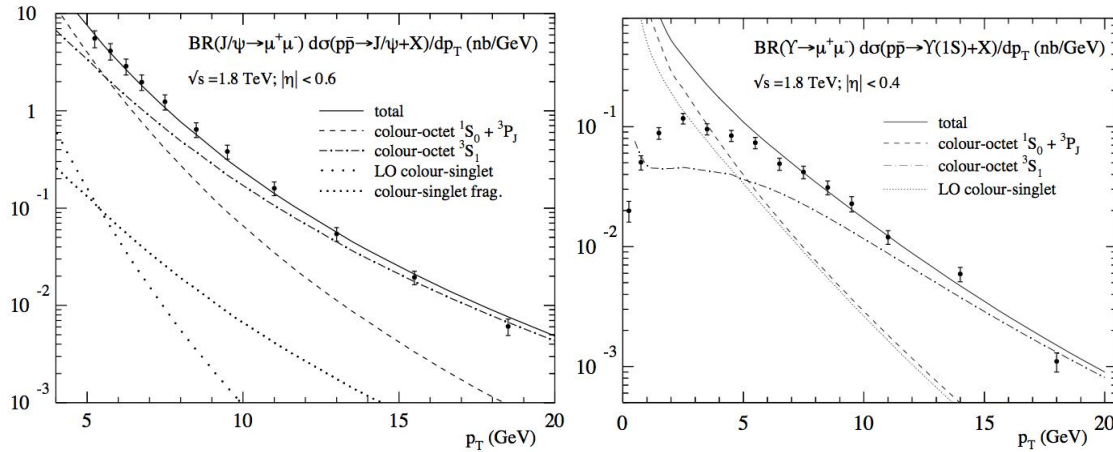


Figure 5.4: Comparison of color-singlet and color-octet calculations to prompt J/ψ (left) and $\Upsilon(1S)$ (right) production at the Tevatron ($\sqrt{s} = 1.8 \text{ TeV}$).

Fig. 5.5 shows the prompt J/ψ and $\Upsilon(1S)$ cross sections measured by the upgraded Collider Detector at Fermilab (CDF II) using data taken between 2002 and 2005 at $\sqrt{s} = 1.96 \text{ TeV}$ in comparison to the CSM at NLO and NNLO* [58]. NLO contributions are characterized by orders up to α_s^4 and NNLO* contributions by orders of α_s^5 . Furthermore, NNLO* calculations use an energy cut-off to suppress the divergent parts.

The primary conclusion is that for the J/ψ cross sections even NNLO* contributions do not describe the actual data accurately. But in contrast to LO and NLO, NNLO* contributions do a better job for the $\Upsilon(1S)$ cross sections.

Recent efforts to implement higher order corrections in color-octet calculations [59] have led to a better understanding of long-distance matrix elements. Butenschön and Kniehl conducted global fits to J/ψ datasets from experiments involving hadroproduction, photoproduction and electron-positron annihilation in different kinematic regions. Furthermore, the results of the LHC were included, which provide more statistics and a larger range in rapidity and p_T . Fig. 5.6 shows that the color-octet contributions are needed to properly describe the data at low p_T . At higher p_T , the theory is in disagreement with the experiment.

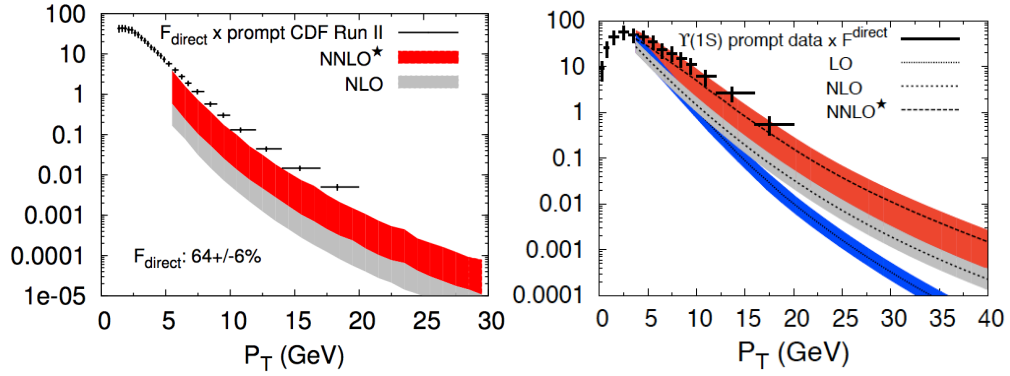


Figure 5.5: NLO and NNLO* contributions of the CSM for J/ψ (left) and $\Upsilon(1S)$ (right) (using CDF II data taken at $\sqrt{s} = 1.96$).

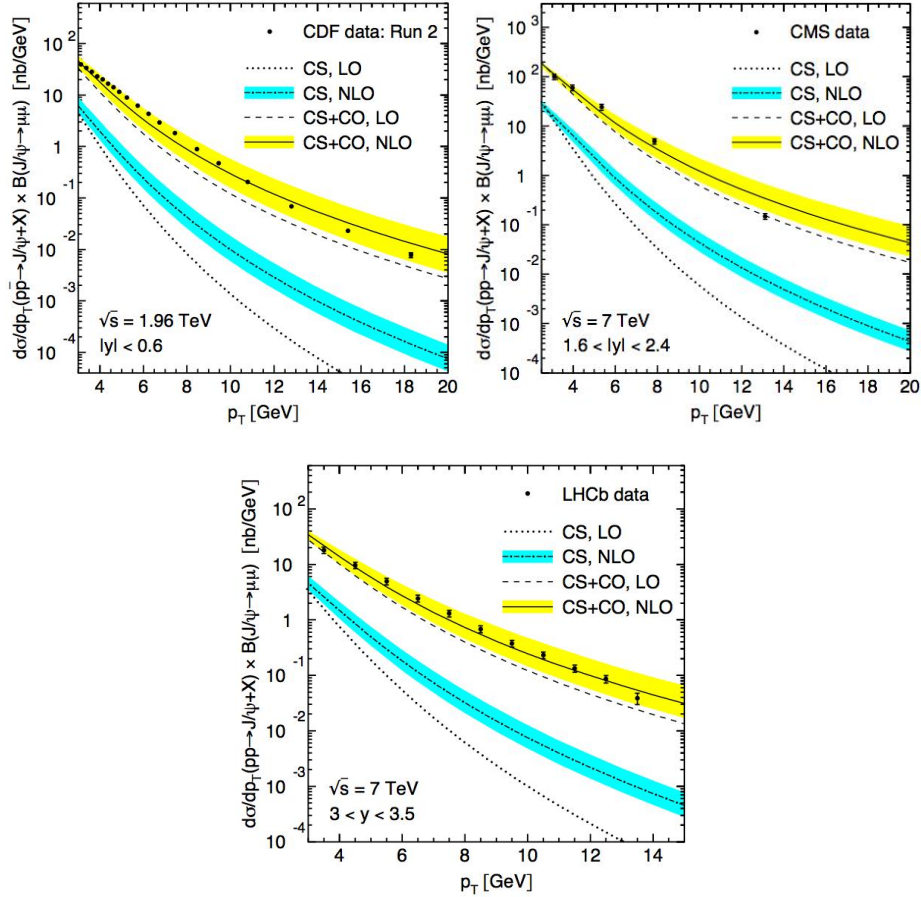


Figure 5.6: Global fits of the NRQCD factorization approach at NLO at different rapidity regions compared to data taken with the CDF detector at Fermilab (top left), the CMS (top right) and the LHCb detectors (bottom) at CERN.

6 Quarkonium Polarization

As seen in the previous chapter, among several theories the NRQCD factorization approach seems to come closest to valid descriptions of quarkonium production differential cross sections at the moment. The NRQCD factorization approach using NLO calculations for colour-singlet and colour-octet contributions has some very promising results, but nevertheless, its calculations depend on long distance color-octet matrices, which are non-perturbative parameters and have to be adjusted to the data.

At this point, it is obvious that differential cross sections do not provide enough information to clearly ensure further progress in understanding the fundamental process of quarkonium production. This leads to the concept of using quarkonium polarization: If a vector quarkonium is measured in a state consisting of one of the three eigenstates of the total angular momentum component J_z with respect to the quantization axis z , this particle is called polarized. While unpolarized particles are an equal mixture of $J_z = -1, 0$ and 1 eigenstates, preferred spin alignment corresponds to the exclusive presence of the $J_z = \pm 1$ or $J_z = 0$ eigenstates and the absence of the other eigenstates. The different theoretical models predict very different polarizations. Since none of the previous cross section measurements has properly taken into account polarization, experimental studies of the polarization of the quarkonium states decaying into lepton pairs, can be expected to give complementary information. On the one hand polarization studies are another test of the theoretical models, and on the other including polarization makes theoretical model predictions more reliable. In this chapter basic ideas and concepts of quarkonium polarization are summarized. For further reading [60][61] are recommended.

6.1 Concepts and Definitions

Different polarization states are characterized by different shapes of the angular distributions of their decay products. While an unpolarized quarkonium state yields, on average, a spherically symmetric distribution, any anisotropy reflects an existing polarization. The distribution of the decay products is measured with respect to a suitable coordinate system defined in the *rest frame* of the quarkonium.

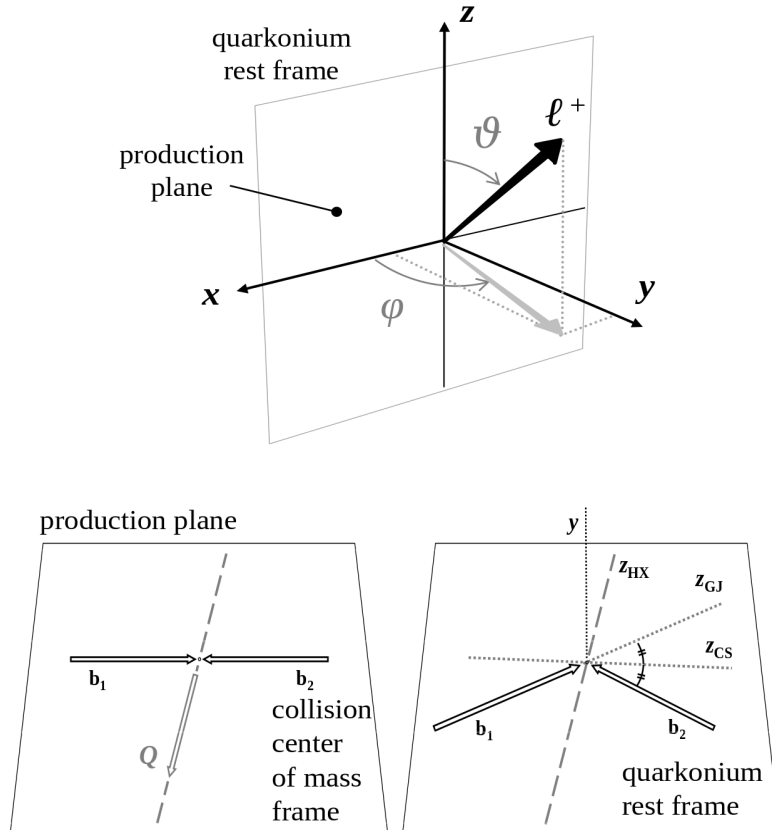


Figure 6.1: Definition of polar (ϑ) and azimuthal angle (φ) of the positive lepton (l^+) (upper plot), definition of production plane and quarkonium rest frame (bottom left, bottom right) [60]. b_1 and b_2 refer to the two colliding proton beams.

The most common frames are:

1. the *center of mass helicity frame (HX)* with the z axis pointing into the direction of the quarkonium momentum.
2. the *Collins-Soper frame (CS)* where the z axis coincides with the relative velocity of the two colliding beams.
3. the *perpendicular helicity frame (PX)* with the z axis being perpendicular to the z axis in the CS frame.
4. the *Gottfried-Jackson frame (GJ)* where the z axis is in the direction of the momentum of one of both colliding beams.

In Fig. 6.1 the concept of the quarkonium rest frame, used for further polarization measurements, is illustrated. In the case of a two body decay $Q \rightarrow \mu^+\mu^-$, the

angular distribution of the decay is defined by the direction of one of the decay products (μ^+ in most of the cases). The average angular distribution of a vector particle in any rest frame is generally written as [62] [63]

$$\mathcal{W}(\cos \vartheta, \varphi | \vec{\lambda}) = \frac{3/(4\pi)}{3 + \lambda_\vartheta} \left(1 + \lambda_\vartheta \cdot \cos^2 \vartheta + \lambda_\varphi \cdot \sin^2 \vartheta \cdot \cos 2\varphi + \lambda_{\vartheta\varphi} \cdot \sin 2\vartheta \cdot \cos \varphi \right), \quad (6.1)$$

where ϑ and φ are the polar and azimuthal angles; λ_ϑ , λ_φ and $\lambda_{\vartheta\varphi}$ are so the called polarization or anisotropy parameters, parametrizing the angular distributions. The three parameters $\lambda_\vartheta, \lambda_\varphi$ and $\lambda_{\vartheta\varphi}$ depend on the choice of the polarization frames, but together they have to fulfill the following properties [64], which are graphically outlined in Fig. 6.2:

$$|\lambda_\varphi| \leq \frac{1}{2}(1 + \lambda_\vartheta),$$

$$\lambda_\vartheta^2 + \lambda_{\vartheta\varphi}^2 \leq 1, \quad (6.2)$$

$$(1 + 2\lambda_\varphi)^2 + 2\lambda_{\vartheta\varphi} \leq 1 \text{ for } \lambda_\varphi \geq 1/3 \text{ and } |\lambda_{\vartheta\varphi}| \leq \frac{1}{2}(1 - \lambda_\varphi) \text{ else.}$$

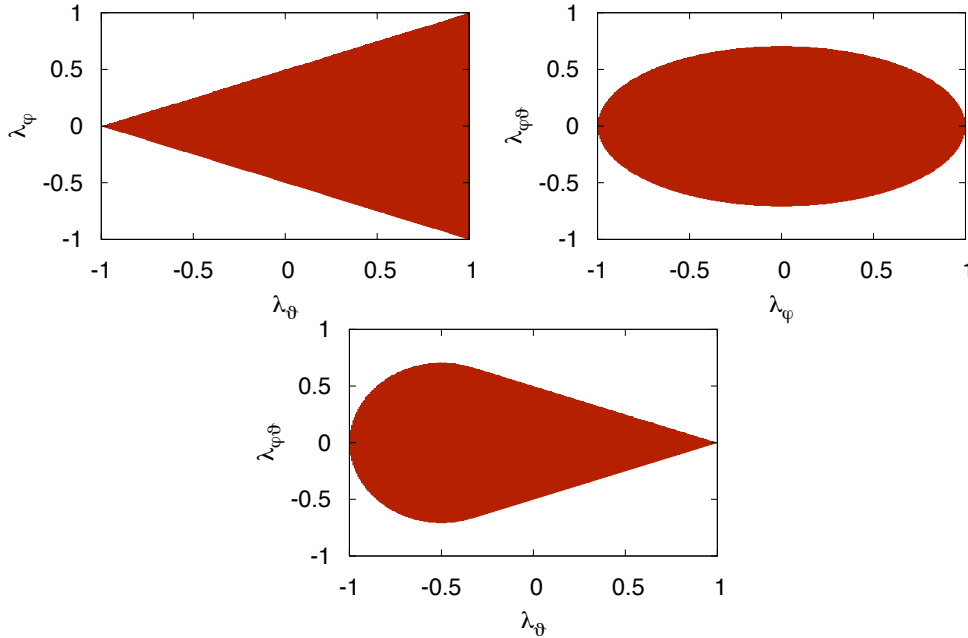


Figure 6.2: Graphical representation of Eqs. 6.2, 6.2 and 6.3.

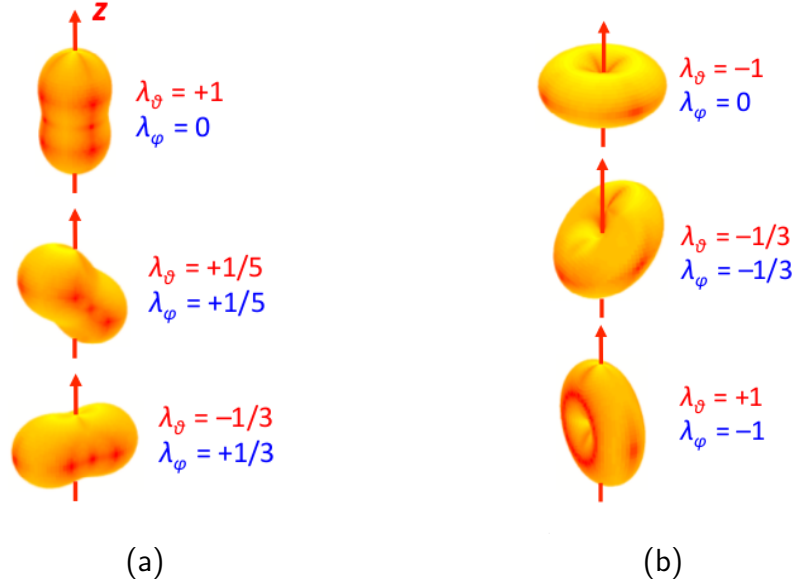


Figure 6.3: Values of λ_ϑ and λ_φ for fully transversely (a) and fully longitudinally (b) polarized states.

Figure 6.3 shows how the polarization parameters λ_ϑ and λ_φ change with the angular decay distributions. The plots display a fully transversely (a) and a fully longitudinally polarized quarkonium state (b), respectively. The λ parameters are frame dependent and therefore change their values when moving from one frame to the next. Measuring only the λ_ϑ parameter, as was done in studies before the LHC era, gives ambiguous results. Therefore, the full angular decay distribution, i.e. all three λ parameters, have to be determined. Moreover it is useful to determine λ_ϑ , λ_φ and $\lambda_{\vartheta\varphi}$ in at least two different frames, in order to cross-check and evaluate the analysis strategy.

Furthermore, a frame independent polarization variable can be calculated from the polarization parameters [64]:

$$\tilde{\lambda} = \frac{\lambda_\vartheta + 3\lambda_\varphi}{1 - \lambda_\varphi} \quad (6.3)$$

$\tilde{\lambda}$ is ideally suited for making cross-checks and comparing results which are measured in different frames. It depicts the average intrinsic polarization of the quarkonium and is equal to +1 for a fully transverse angular decay distribution and -1 in case of longitudinal polarization. This fact can easily be examined by applying Eq. 6.3 to the different states in Fig. 6.3. In particular for small polarization parameters, $\tilde{\lambda}$ often reveals more significant polarization effects than the frame dependent parameters.

6.2 The Quarkonium Polarization Puzzle

In 2000 and 2007, the Tevatron experiment CDF published measurements of prompt J/ψ polarization from $p\bar{p}$ collisions at $\sqrt{s} = 1.8$ GeV and $\sqrt{s} = 1.96$ GeV, respectively [65][66]. Resulting α dependences of p_T are shown in Fig. 6.4, where the polarization parameter α corresponds to λ_θ in the HX frame. While the analysis of Run I (Fig. 6.4 (a)) indicates a significant transverse polarization for $p_T < 14$ GeV, the analysis of Run II (Fig. 6.4 (b)) indicates a slightly longitudinal polarization. The results are compared to NRQCD (COM) predictions and the k_t factorization approach, respectively. In case of quarkonium production, the k_t factorization model is usually applied within the CSM [51]. It states that parton distributions for initial-state hadrons depend on the parton transverse momentum fraction as well as on the parton longitudinal momentum fraction. The two models also predict quite different results over the p_T range covered by CDF. On the one hand the k_t factorization model foresees a strong longitudinal polarization, and on the other hand NRQCD foresees a zero to slightly transverse polarization.

The results of the two CDF measurements are incompatible over a large fraction of the covered p_T range. These discrepancies have not yet been explained satisfactorily. Furthermore, the polar anisotropy parameter has only been measured in one reference frame, not allowing to interpret the results unambiguously. These inconsistencies have strongly motivated a new and more complete measurement of quarkonium polarization, especially in high p_T regions, where the model predictions are more reliable and differ more significantly from each other. At high p_T a full transverse polarization of directly produced quarkonia is for example a limit prediction of the NRQCD factorization approach. LHC delivers data up to much higher p_T regions. Moreover, due to very high statistics, polarization measurements of several different (and also excited) quarkonium states (e.g. χ_{bJ} , χ_{cJ}) can be conducted.

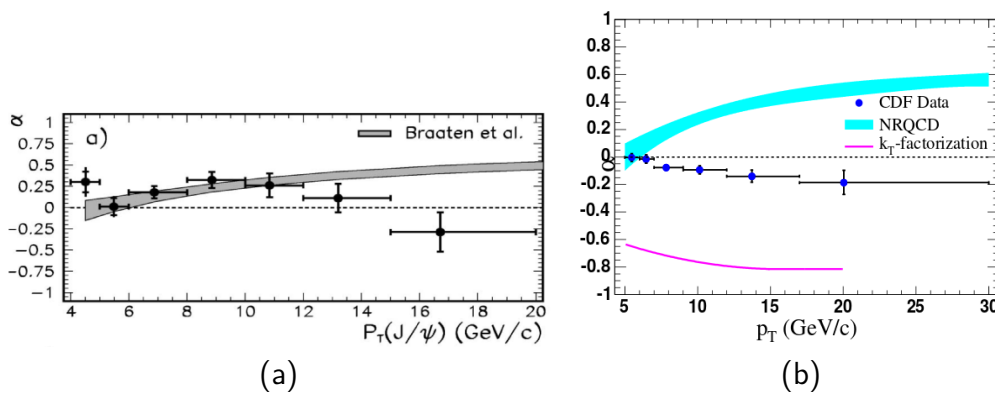


Figure 6.4: J/ψ polarization measurements conducted by CDF Tevatron Run I ($\sqrt{s} = 1.8$ GeV) and Run II ($\sqrt{s} = 1.96$ GeV). α corresponds to the λ_θ parameter as function of p_T . The results are compared to theoretical models [65][66].

6.3 Measurement of χ_{cJ} Polarization

CMS is currently measuring the polarization of prompt χ_{c1} and χ_{c2} charmonium states using data collected in pp collisions at $\sqrt{s} = 8$ TeV. The χ_{cJ} states are reconstructed via their radiative decays $\chi_{c1,2} \rightarrow J/\psi + \gamma$. The resulting photon γ in turn is measured through pair conversion in the tracker. Its momentum resolution allows the two states to be separated with good accuracy.

Recent studies showed [67] that the angular distribution of n^3P_J quarkonia is very similar to the dilepton angular distribution of n^3S_1 quarkonia decaying into two leptons. The accessible momenta at the CMS detector are large enough to make the bias of this approximation negligible. Hence, the polarization measurements of the J^{++} states can be conducted in exactly the same way as the measurement of the 1^{--} states. Those states, which have an invariant mass close to the mass of the required J^{++} state but are accompanied by a photon originating from the dilepton vertex, have to be identified.

The $J/\psi + \gamma$ data provide the following inputs for the measurement of the polarization:

- The muon four-vectors p_μ of the selected events
- The fraction of total background events
- The $(\cos\vartheta, \varphi)$ 2D distribution of the total background events in one frame (PX frame)
- The 3D total background distribution as function of the dimuon transverse momentum p_T , the absolute value of the dimuon rapidity $|y|$ and the invariant dimuon mass M .

The most important external inputs to the analysis are the single muon detection efficiencies and the dimuon efficiency corrections due to correlations.

The used event sample includes on the one hand prompt and non-prompt χ_{cJ} mesons, and on the other hand $J/\psi + \gamma$ combinatorial background as well as a small fraction of $\mu\mu + \gamma$ combinatorial background. The goal of this analysis is to measure the polarization of prompt χ_{cJ} events. Non-prompt χ_{cJ} mesons originate from decays of B^+ , B^0 and B^s mesons, as well as from Λ_b baryon decays. Due to their longer lifetime, these hadrons usually cover a distance of the order of 0.1 mm before decaying into χ_{cJ} mesons. Thus, given the lifetime distribution the non-prompt χ_{cJ} mesons can be easily distinguished from prompt events. The used variable is the so called *pseudo-proper lifetime* l , which is defined as [68]

$$l = l^\Psi = \frac{L_{xy} \cdot M^\Psi}{p_T^\Psi}, \quad (6.4)$$

where M^Ψ is the dimuon mass, p_T^Ψ the scalar dimuon transverse momentum and L_{xy} the most probable transverse decay length in the laboratory frame. The attribute *pseudo-proper* reflects the fact that not the proper lifetime of a beauty hadron is measured, since the full decay is not completely reconstructed. However, since l^Ψ is only used to distinguish between prompt and non-prompt mesons, it can be used without constraints.

In order to exclude both underlying continuous $J/\psi + \gamma$ and $\mu\mu + \gamma$ background contributions, signal regions within an appropriate mass window around the known invariant masses of $M^{\chi_{1s}} = 3.51066 \pm 0.00007$ GeV and $M^{\chi_{2s}} = 3.5562 \pm 0.00009$ GeV are defined [69]. The mass distribution of the χ_{c1} and χ_{c2} peaks is simulated with a Crystal Ball function [70] taking into account both detector resolution and the radiative tail resulting from the final state radiation. Eight different mass and lifetime regions are defined as shown in Fig. 6.5:

- 4 regions in M^χ containing both the background-enriched left-sideband (LSB) and the background-enriched right-sideband (RSB) as well as the two signal regions around $M^{\chi_{1s}}$ and $M^{\chi_{2s}}$ (SR1 and SR2).
- 2 regions in l^Ψ , the prompt-signal-enriched (PR) as well as the non-prompt signal-enriched (NP) region.

A fraction of events with the same $(p_T, y, M, \cos \vartheta, \varphi)$ distribution as the background model is removed from the data sample on an event-by-event basis.

The polarization parameters are calculated applying Bayesian statistics. While the a-priori probability density is uniform for all λ parameters, events of the two prompt-signal-enriched regions are used to calculate the posterior probability density (PPD) of the prompt χ_{cJ} polarization parameters ($\vec{\lambda}$) for each kinematic bin,

$$\mathcal{P}(\vec{\lambda}) = \prod_i \mathcal{E}(\vec{p}_1^{(i)}, \vec{p}_2^{(i)}), \quad (6.5)$$

where \mathcal{E} is the probability density as a function of the two muon momentum vectors in event i . In order to obtain $\mathcal{P}(\vec{\lambda})$, the likelihood function $\mathcal{L}(\vec{p}_1, \vec{p}_2)$ is used:

$$\mathcal{L}(\vec{p}_1, \vec{p}_2) = \mathcal{W}(\cos \vartheta, \varphi | \vec{\lambda}) \epsilon_{\mu\mu}(\vec{p}_1, \vec{p}_2), \quad (6.6)$$

where $\mathcal{W}(\cos \vartheta, \varphi | \vec{\lambda})$ is the dimuon angular distribution defined in Eq. 6.1 and $\epsilon_{\mu\mu}$ the dimuon efficiency.

Dimuon efficiency corrections are applied for every event

$$\epsilon_{\mu\mu}(\vec{p}_1, \vec{p}_2) = \epsilon_{\mu 1}(\vec{p}_1) \cdot \epsilon_{\mu 2}(\vec{p}_2) \cdot \epsilon_{Vtx}(\cos \vartheta, \varphi) \cdot \rho(\vec{p}_1, \vec{p}_2), \quad (6.7)$$

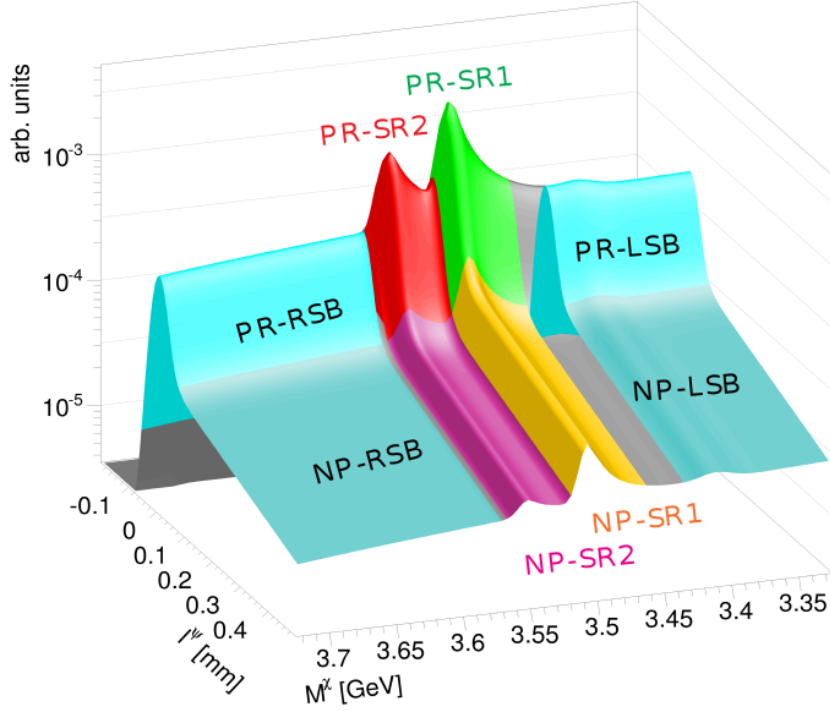


Figure 6.5: χ mass-lifetime model divided into 8 different regions. See text for further explanations [71].

where $\epsilon_{\mu 1}(\vec{p}_1)$ and $\epsilon_{\mu 2}(\vec{p}_2)$ are the single muon detection efficiencies as functions of the single muon transverse momentum p_T and the absolute value of the single muon pseudorapidity $|\eta|$. $\epsilon_{Vtx}(\cos \vartheta, \varphi)$ is the efficiency of the dimuon vertexing module as a function of $\cos \vartheta$ and φ and $\rho(\vec{p}_1, \vec{p}_2)$ expresses the correlation between both muons as a function of dimuon p_T , dimuon $|y|$, $\cos \vartheta$ and φ . The total dimuon efficiency is not a simple product of the single muon detection efficiencies; it must also take into account correlations induced to the muons in those cases where the detector is insensitive to the presence of a muon pair. The efficiencies are corrected on an event-by-event basis. For the χ_{cJ} polarization analysis the dimuon efficiencies are provided in the PX frame. The muon efficiencies are always calculated for the J/ψ meson. The difference in mass is a second order effect for the muon efficiencies of the other quarkonium states and therefore neglected. A detailed efficiency consideration is given in Chap. 7.

6.4 Recent CMS Results

CMS recently measured the polarization of the $\Upsilon(nS)$ and the prompt $\psi(nS)$ states using data collected in pp collisions at $\sqrt{s} = 7$ TeV. The dataset corresponded to an

integrated luminosity of 4.9fb^{-1} [72][73]. In case of the $\psi(nS)$ states, studies of the two-dimensional mass-lifetime distribution have been used to subtract continuum background and non-prompt events, respectively (similar to the χ_{cJ} polarization measurements). Fig. 6.6 shows an example of the projection of the invariant dimuon mass and the projection of the pseudo-proper decay length for a J/ψ state.

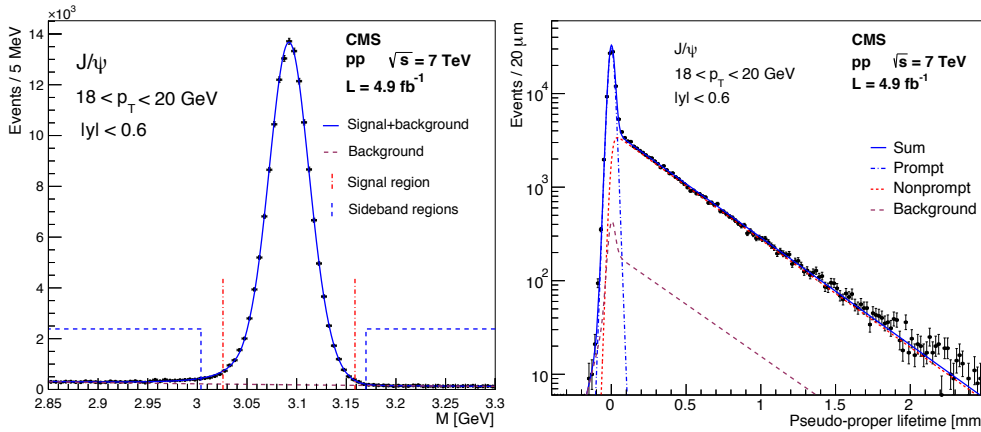


Figure 6.6: Dimuon invariant-mass (a) and lifetime distribution (b) in the J/ψ region for $18 < p_T < 20$ GeV and absolute rapidity < 0.6 [72].

In case of the $\Upsilon(nS)$ states, which have larger masses than B mesons, the invariant dimuon mass is also used to subtract continuum background, but no lifetime considerations are needed (Fig 6.7).

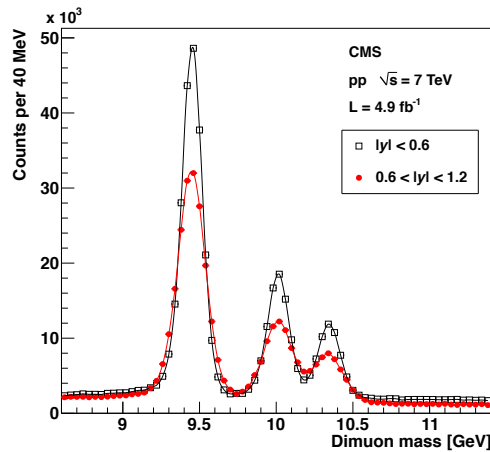


Figure 6.7: Dimuon mass distribution in the $\Upsilon(nS)$ region for two rapidity bins [73].

The polarization parameters have been calculated applying Bayesian statistics (Sec. 6.3) with the 2011 single muon efficiencies and dimuon efficiency corrections as most important external input parameters. The studies have been conducted for the polarization parameters λ_ϑ , λ_φ , $\lambda_{\vartheta\varphi}$ and $\tilde{\lambda}$ in the CS, the HX and the PX frame. Fig. 6.8

shows the results of $\tilde{\lambda}$ for the $\psi(nS)$ and $\Upsilon(nS)$ states. No evidence of strong polarization was seen for any polarization parameter in the explored kinematic regions for any of the states under study.

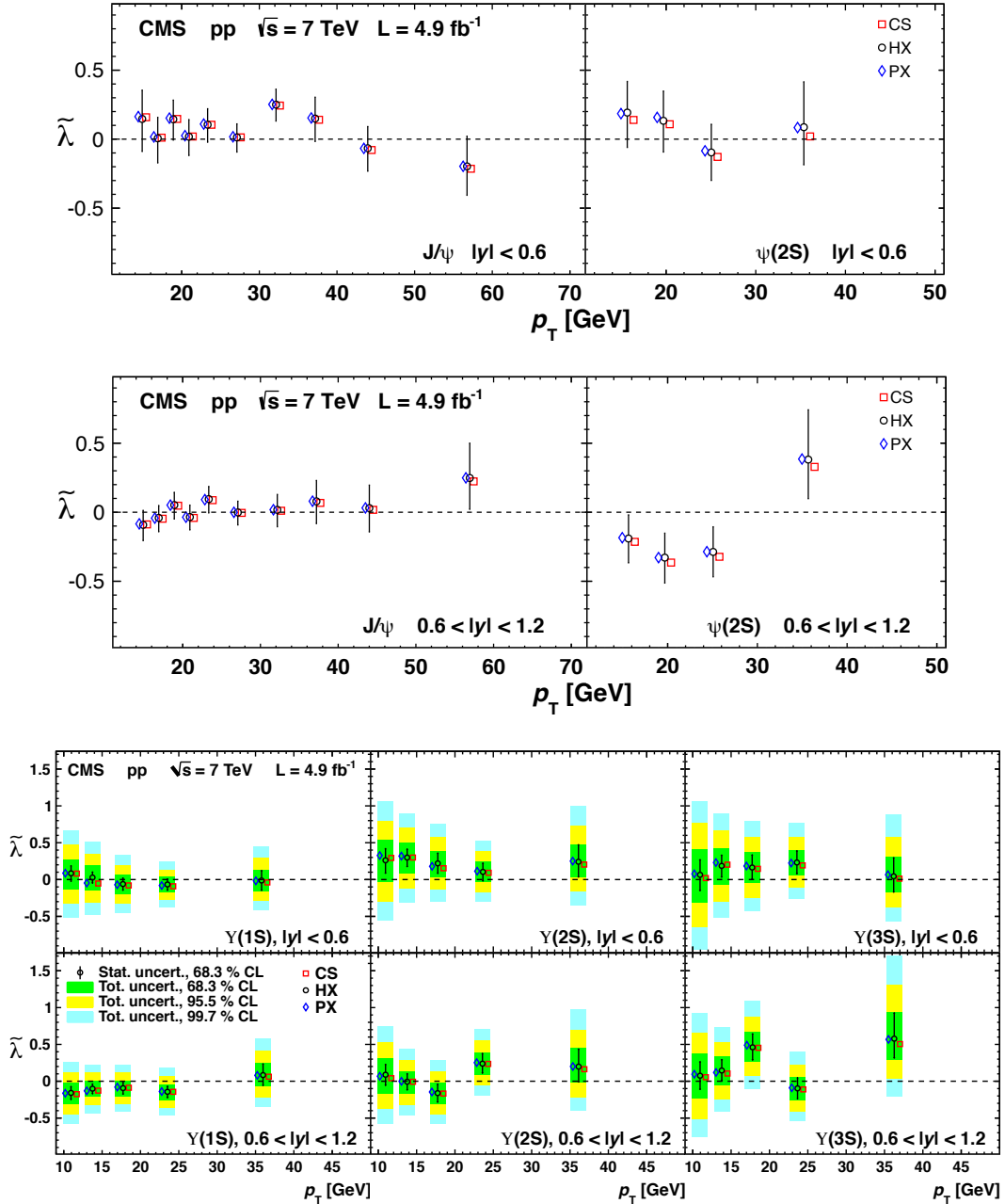


Figure 6.8: Values of $\tilde{\lambda}$ for the J/ψ (top), for the $\psi(2S)$ (middle) and for $Y(1S)$, $Y(2S)$ and $Y(3S)$ (bottom) [72][73].

7 Tag and Probe Efficiencies

7.1 Tag and Probe Method

The Tag and Probe (TnP) approach is often used to determine object efficiencies from huge data sets. Well known di-object resonances (e.g. J/ψ) are reconstructed as pairs in a way that one object passes tight identification criteria (tag) and the other one passes looser criteria (probe). Hereby, the combined mass of tag and probe (muons in this case) has to be consistent with the di-object resonance (J/ψ). Amongst all probes additional criteria are applied, which if fulfilled yield so called *passing probes*. Otherwise they are referred to as *failing probes*. Efficiencies are now obtained by calculating the fraction of *passing probes* and *all probes*:

$$\epsilon = \frac{N_{\text{passing probes}}}{N_{\text{all probes}}} = \frac{N_{\text{passing probes}}}{N_{\text{passing probes}} + N_{\text{failing probes}}} \quad (7.1)$$

In a first step, the TnP dataset is prepared using the official CMS TnP producer, which provides an output with one entry per (tag+probe) pair containing important variables, e.g. invariant dimuon mass. Next, the pairs are split up into certain p_T and $|\eta|$ bins. The mass distributions for passing and failing probes for each bin are fitted simultaneously exploiting probability density functions (PDF). The PDFs used in the following analysis are Crystal Ball functions for the signal and an exponential for the description of the background. For further information on producing and fitting TnP pairs see [74][75]. Figure 7.1 shows an example of a simultaneous TnP fit.

The detection efficiency of the measured muon should not be influenced in any way by the existence of a second muon and, thus, the whole working procedure has to be applied very carefully in order not to bias the measurements.

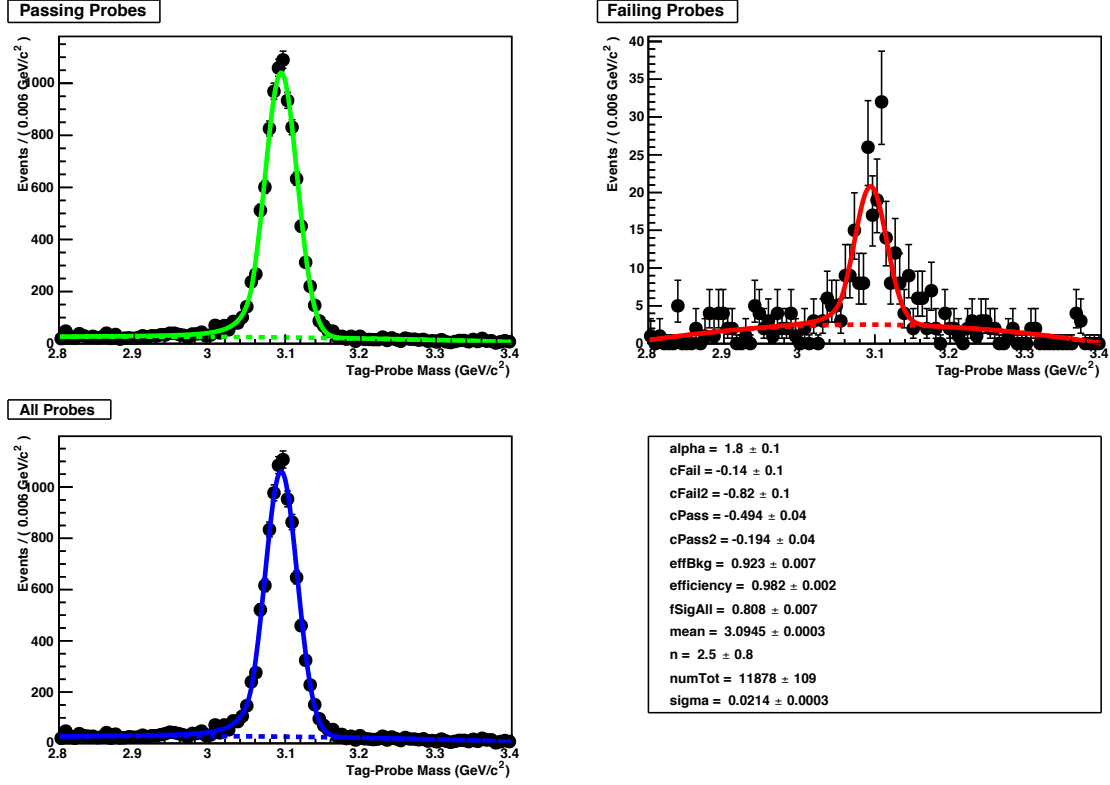


Figure 7.1: Example of a simultaneous fit to passing and failing probes in the $10 \text{ GeV} < p_T < 12.5 \text{ GeV}$ and $0.0 < |\eta| < 0.2$ bin. The lower right plot contains variables for passing and failing probe and the deduced efficiency.

The *total single muon efficiency* $\epsilon_{tot}(\mu)$ (also denoted *efficiency product* in this thesis) is studied as a product of five sequential detection efficiencies:

$$\epsilon_{tot}(\mu) = \epsilon_{Track}(\mu) \cdot \epsilon_{MuonID}(\mu) \cdot \epsilon_{MuQual}(\mu) \cdot \epsilon_{L1\cdot L2}(\mu) \cdot \epsilon_{L3}(\mu) \quad (7.2)$$

with

- $\epsilon_{Track}(\mu)$ being the offline muon tracking efficiency in the silicon tracker,
- $\epsilon_{MuonID}(\mu)$ being the offline reconstruction (or identification) efficiency in the muon chambers with respect to the silicon detector track,
- $\epsilon_{MuQual}(\mu)$ being the efficiency of muon tracking quality cuts with respect to offline reconstructed muons without any quality cuts,
- $\epsilon_{L1\cdot L2}(\mu)$ being the combined L1·L2 trigger efficiency with respect to an offline reconstructed muon with quality cuts,

- $\epsilon_{L3}(\mu)$ being the L3 trigger efficiency with respect to all previous efficiencies.

The offline muon tracking efficiency has been extensively studied by the muon POG (Physics Object Group) and will not be discussed further here. The offline muon tracking efficiency for MC is set to a default value of 0.995. The efficiencies for data are derived with the help of the scale factors shown in Tab. 7.1.

η_{min}	η_{avg}	η_{max}	ϵ	err
-2.4	-2.237	-2.1	98.69	± 0.07
-2.1	-1.840	-1.6	99.48	± 0.02
-1.6	-1.397	-1.2	99.67	± 0.02
-1.2	-1.043	-0.9	99.74	± 0.02
-0.9	-0.747	-0.6	99.80	± 0.01
-0.6	-0.449	-0.3	99.80	± 0.01
-0.3	-0.249	-0.2	99.72	± 0.02
-0.2	0.000	0.2	99.63	± 0.01
0.2	0.249	0.3	99.78	± 0.02
0.3	0.449	0.6	99.77	± 0.01
0.6	0.747	0.9	99.76	± 0.01
0.9	1.043	1.2	99.68	± 0.02
1.2	1.397	1.6	99.59	± 0.03
1.6	1.839	2.1	99.70	± 0.02
2.1	2.237	2.4	98.36	± 0.08

Table 7.1: Data/MC scale factors of the offline muon tracking efficiency for different $|\eta|$ bins.

Muon pairs can be classified as *seagull* and *cowboy* dimuons. Dimuons are called seagulls if the magnetic field bends them away from each other, and cowboys if the magnetic field bends them towards each other, respectively. Studies conducted in 2011 revealed differences between the efficiencies of cowboys and seagulls at L1-L2. Thus, the efficiencies are calculated separately for cowboys and seagulls as well as for all dimuons. Furthermore, potential effects on the polarization analysis, arising from deviations between seagull and cowboy dimuons, are studied in Chap.9.

7.2 Used Datasets, Filters and Triggers

The following efficiencies are calculated for 2012 data collected in pp collisions at a center of mass energy $\sqrt{s} = 8$ GeV. The data set corresponds to an integrated luminosity of 20.7 fb^{-1} (about 4 times more than in 2011). Additionally, Monte Carlo (MC) samples are processed in a way that 19 million J/ψ events are exposed

to the full detector simulation, providing realistic running conditions, e.g. run dependent HLT menus and trigger settings, data taking conditions, pileup and reflection of the increase in luminosity.

The efficiency of dimuon triggers cannot be determined in an unbiased way with the TnP method without the usage of special triggers. These so called efficiency triggers can be viewed as single muon triggers additionally requiring a track. In cases where a tracking related efficiency is studied, the efficiency trigger requires a L2 muon instead of a track. Special efficiency *dimuon* triggers are the **HLT_MuX_TrackY_Jpsi** triggers and the **HLT_MuX_L2MuY_Jpsi** triggers (*HLT_MuX_L2Mu3_Jpsi*), with one part (leg) requiring a muon and the other leg either a silicon track or a L2 muon. *HLT_Mu5_Track2_Jpsi* as well as *HLT_Mu5_Track3p5_Jpsi* and *HLT_Mu7_Track7_Jpsi* are made for studying the same efficiencies, but cover different p_T regions. The first two are heavily prescaled, but cover low p_T regions where the efficiencies have not reached their saturation values. Table 7.2 summarizes the p_T range of the different **HLT_MuX_TrackY_Jpsi** triggers.

Trigger	p_T range
HLT_Mu5_Track2_Jpsi	$2 < p_T < 4$ GeV
HLT_Mu5_Track3p5_Jpsi	$4 < p_T < 7.5$ GeV
HLT_Mu7_Track7_Jpsi	$p_T > 7.5$ GeV

Table 7.2: p_T ranges of the different **HLT_MuX_TrackY_Jpsi** triggers.

Troubles faced by **HLT_MuX_TrackY_Jpsi** triggers are their impurity, since there is no guarantee for the second leg (being a silicon leg) to become a second muon. While **HLT_MuX_TrackY_Jpsi** triggers are used for unbiased studies of offline muon reconstruction and L1·L2 efficiencies, **HLT_MuX_L2MuY_Jpsi** triggers ensure evaluation of muon quality and L3 trigger efficiencies.

For single muon efficiency studies the following binnings in p_T and $|\eta|$ are chosen:

- single muon p_T : 2., 2.25, 2.5, 2.75, 3., 3.25, 3.5, 3.75, 4., 4.25, 4.5, 4.75, 5., 5.5, 6., 6.5, 7., 7.5, 8., 8.5, 9., 9.5, 10., 12.5, 15., 17.5, 20., 22.5, 25., 27.5, 30., 35., 40., 50., 70.
- single muon $|\eta|$: 0., 0.2, 0.3, 0.6, 0.8, 1., 1.2, 1.4, 1.6, 1.8, 2.

Efficiency studies are performed for so called **soft muons**; they are defined as [76]:

- The tracks of the innermost silicon tracker are extrapolated and matched to the muon segments in the DTs or CSCs. A matching requires that the distance between the extrapolated and detected muons is less than 3 cm or that the pull distribution, which describes the statistical properties of the standard score, is within the value 3, in the local best-measured coordinate.
- In order to resolve ambiguities and remove duplicates, the best geometrical matching of silicon tracker and the muon segments is chosen.

7.3 Offline Muon Reconstruction Efficiency

The offline muon reconstruction (or identification) efficiency, $\epsilon_{\text{MuonID}}(\mu)$, is the probability of identifying an offline muon track in the muon chambers, preconditioned by its match in the silicon tracker. Tags are given by muons matching to the *Mu* leg of the *HLT_MuX_TrackY_Jpsi* trigger. The probes are general tracks with a match to the *Track* leg of the efficiency trigger part. Passing probes are requested to be arbitrated tracker muons, which have a match to the muon segments in the DTs or CSCs. In contrast to the remaining three sequential efficiencies – $\epsilon_{\text{MuQual}}(\mu)$, $\epsilon_{L1.L2}(\mu)$ and $\epsilon_{L3}(\mu)$ – no quality requirements can be applied to all the probes to reduce the background. The signal for failing probes is rather poor as shown in Fig. 7.2 and, thus, it is difficult to obtain reliable data driven efficiencies. Efficiencies derived in MC are not affected by this since the simulations only contains signal events. Hence, for calculations of the efficiency product MC based results are taken, but corrected with data/MC scaling factors.

Figure 7.3 shows a comparison of the data driven and MC based offline muon reconstruction efficiencies for different bins in $|\eta|$. The plateau is reached after a steep turn-on at ~ 6 GeV. To better visualize differences between data and MC, the ratio data/MC has been calculated (see Fig. 7.4). The difference between data and MC in the turn-on region arises from a small difference between the extrapolated tracks, which is amplified by a large variation of the efficiencies throughout the individual bins [15].

The efficiency was also studied for cowboy and seagull dimuons. As expected, neither the data-driven efficiencies shown in Fig. 7.5 nor the MC based efficiencies depicted in Fig. 7.6 show differences between cowboy and seagull dimuons. Plots showing the data and MC comparison for cowboys and seagulls can be found in Appendix A.

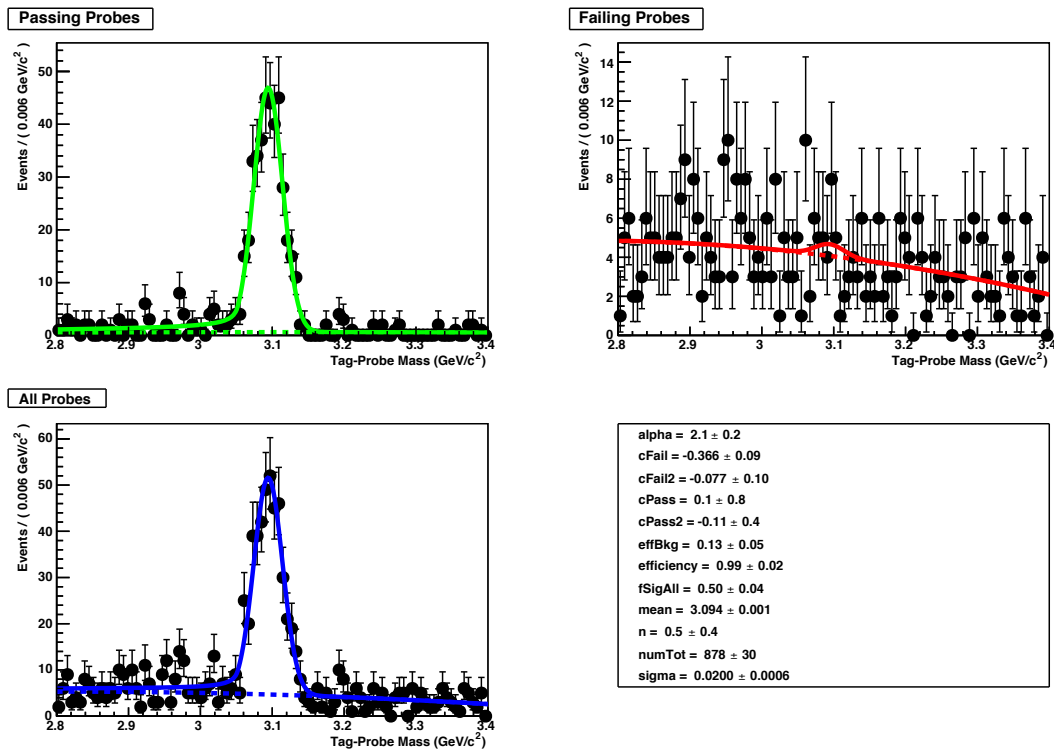


Figure 7.2: Simultaneous fit to passing and failing probes in the $0.0 < |\eta| < 0.2$ and $10 \text{ GeV} < p_T < 12.5 \text{ GeV}$ bin. The lower right plot contains variables for passing and failing probe and the deduced efficiency.

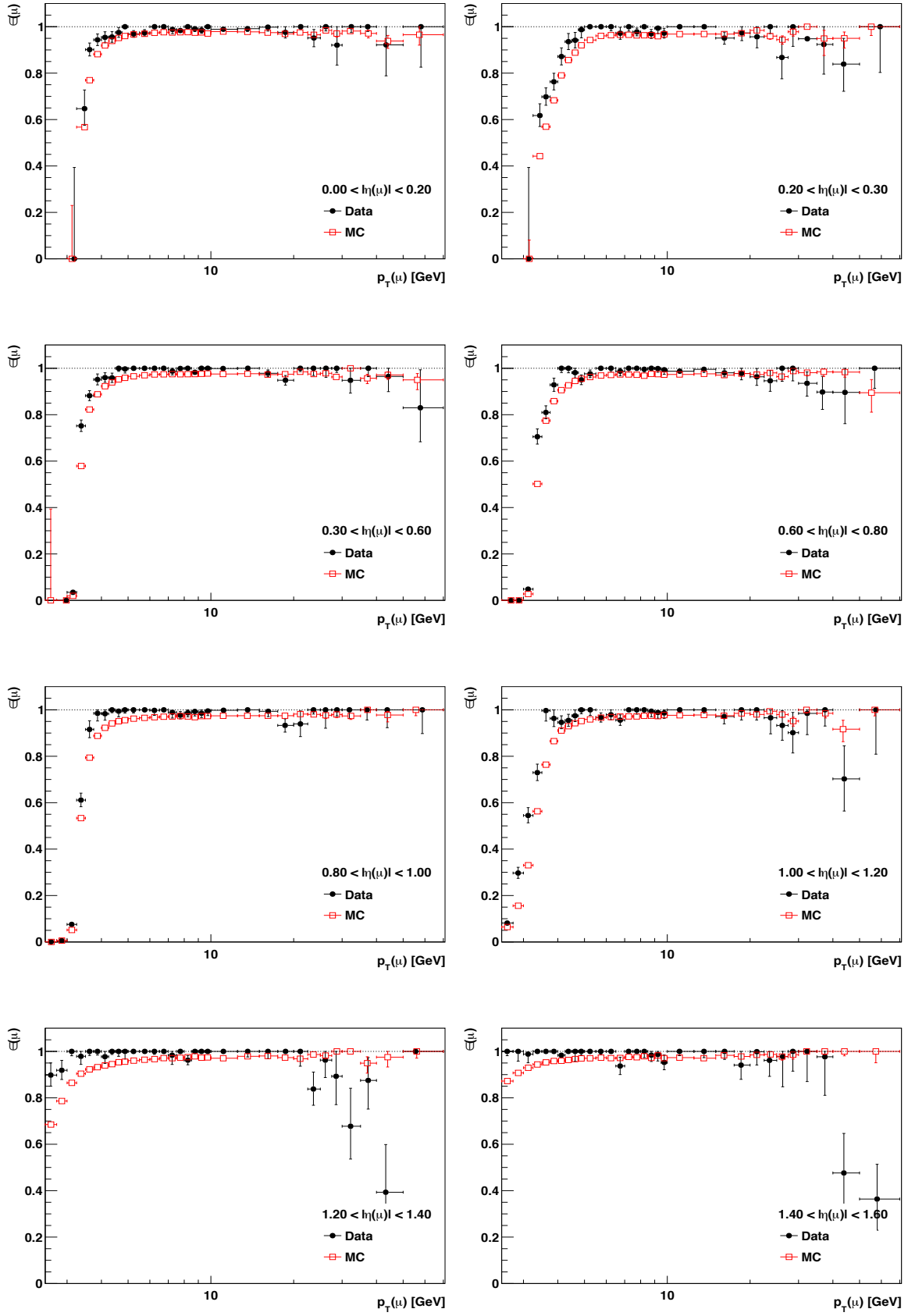


Figure 7.3: Offline muon reconstruction efficiencies as a function of p_T for several $|\eta|$ bins calculated for all dimuon pairs.

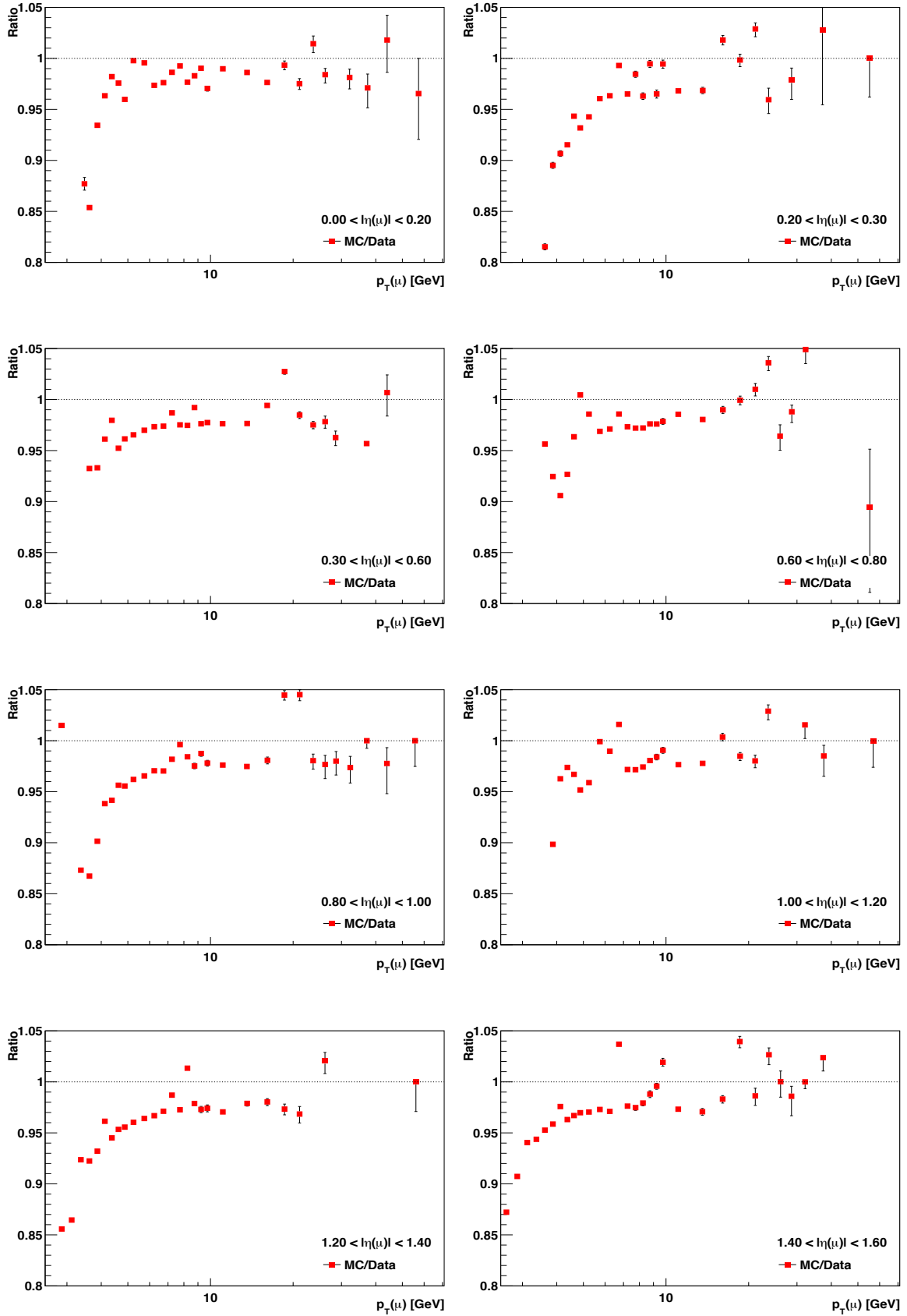


Figure 7.4: Ratio data/MC for offline muon reconstruction efficiencies as a function of p_T for several $|\eta|$ bins. Error bars correspond to the first moment of the MC driven efficiencies.

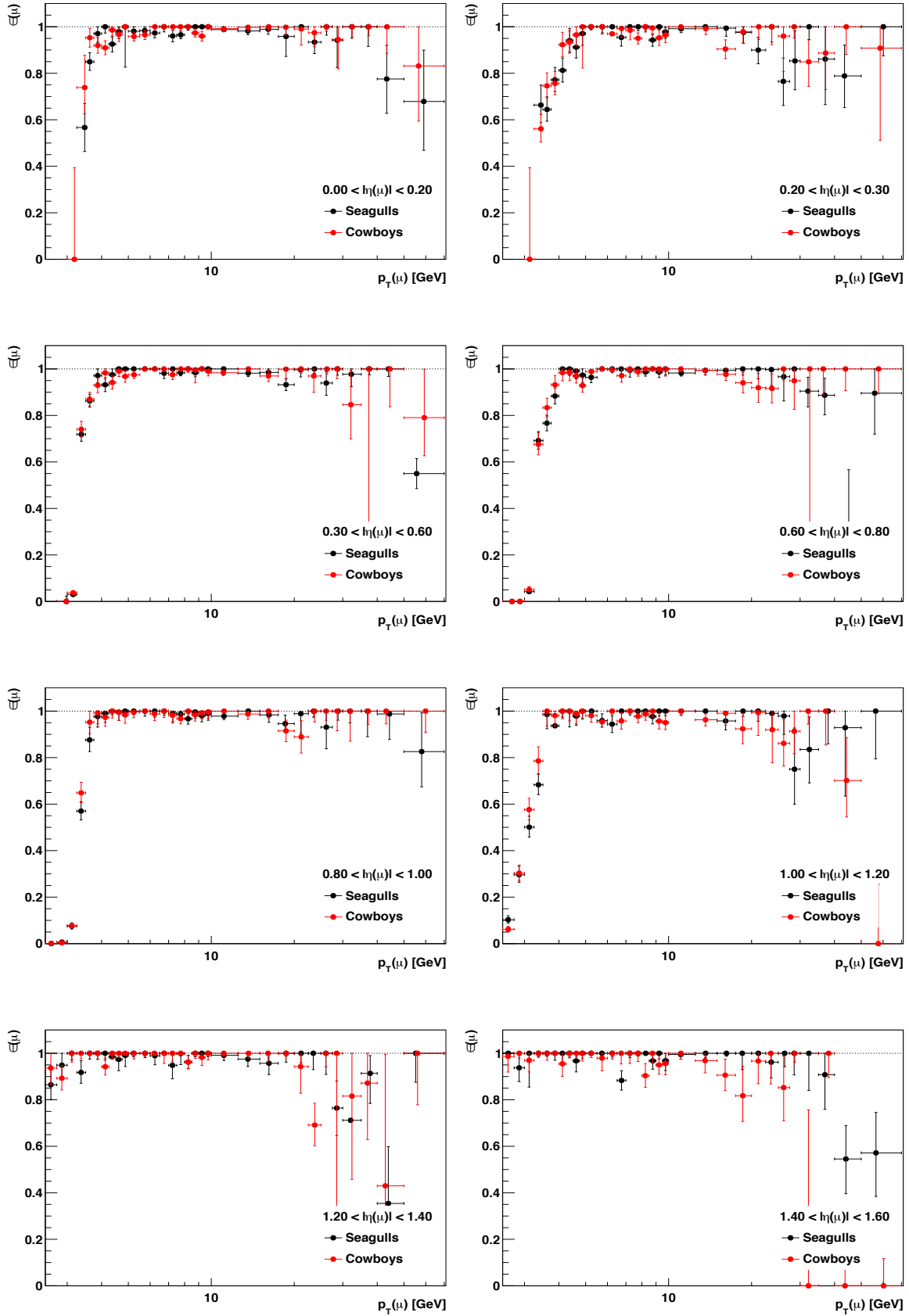


Figure 7.5: Data-driven offline muon reconstruction efficiencies calculated for seagull and cowboy dimuons as a function of p_T for several $|\eta|$ bins.

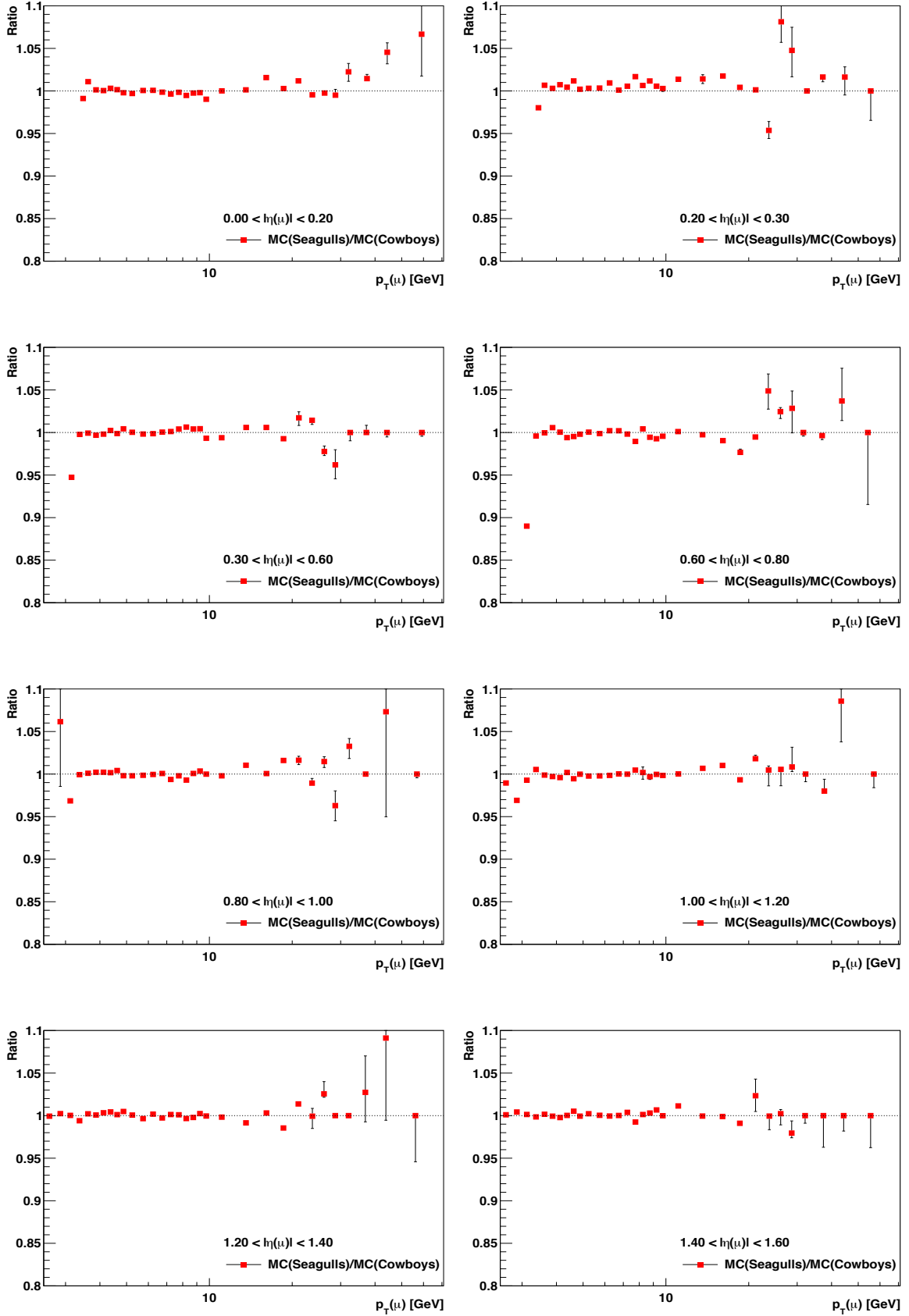


Figure 7.6: Ratio of MC driven offline muon reconstruction efficiencies calculated for seagull dimuons over the one calculated for cowboy dimuons as a function of p_T for several $|\eta|$ bins. The error bars correspond to the first moment of the respective fraction.

7.3.1 Scale Factor

As explained above, the MC based offline muon reconstruction efficiencies are used to calculate the total single muon efficiency. To correct for differences in data and MC, data/MC scale factors calculated in broader $|\eta|$ bins are applied. The offline muon reconstruction scaling factors are obtained for:

- the central barrel region $|\eta| < 0.9$ excluding $0.2 < |\eta| < 0.3$
- the overlap region $0.9 < |\eta| < 1.2$
- the endcap region $1.2 < |\eta| < 2.0$
- $0.2 < |\eta| < 0.3$

Due to the partly non-instrumented region of the barrel detector (see Fig. 3.2), the $0.2 < |\eta| < 0.3$ bin is excluded and calculated separately. To get rid of statistical fluctuations, the scale factor is parametrized with a $\frac{1}{p_\alpha}$ function at low p_T and with a constant at high p_T . The scale factor fitted with the described function is shown in Fig. 7.7.

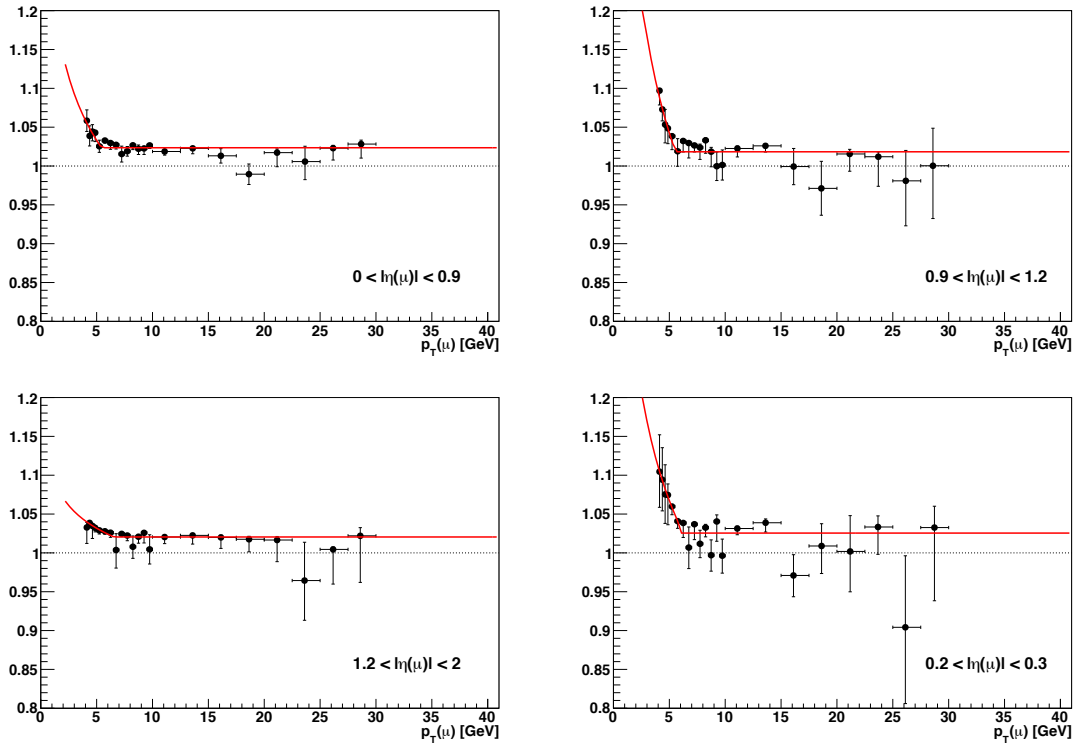


Figure 7.7: Data/MC scale factors as a function of p_T for different $|\eta|$ bins fitted with a $\frac{1}{p_\alpha}$ function at low p_T and with a constant at high p_T .

7.4 Efficiency of the Muon Tracking Quality Cuts

The efficiency of the muon tracking quality cuts measures the probability of an offline reconstructed muon to pass mandatory quality cuts. While tags have a match to the $Mu5$ leg of the $HLT_Mu5_L2Mu2_Jpsi$ trigger, probes are passing probes from the previous step. Hence, they have already fulfilled all required conditions for the offline muon reconstruction efficiency. The passing probes are required to fulfill all the criteria of a soft muon.

Figure 7.8 shows the data-driven and MC based efficiencies of the muon tracking quality cuts. The effect of the tracking related selection cuts is quite small: the resulting dimuon inefficiency is $\sim 3\%$, and is practically independent of dimuon p_T and $|\eta|$. MC driven efficiencies are consistently higher by $\sim 1\%$. Figure 7.9 shows the comparison between data-driven efficiencies for seagull and cowboy dimuons. As expected, no differences are found.

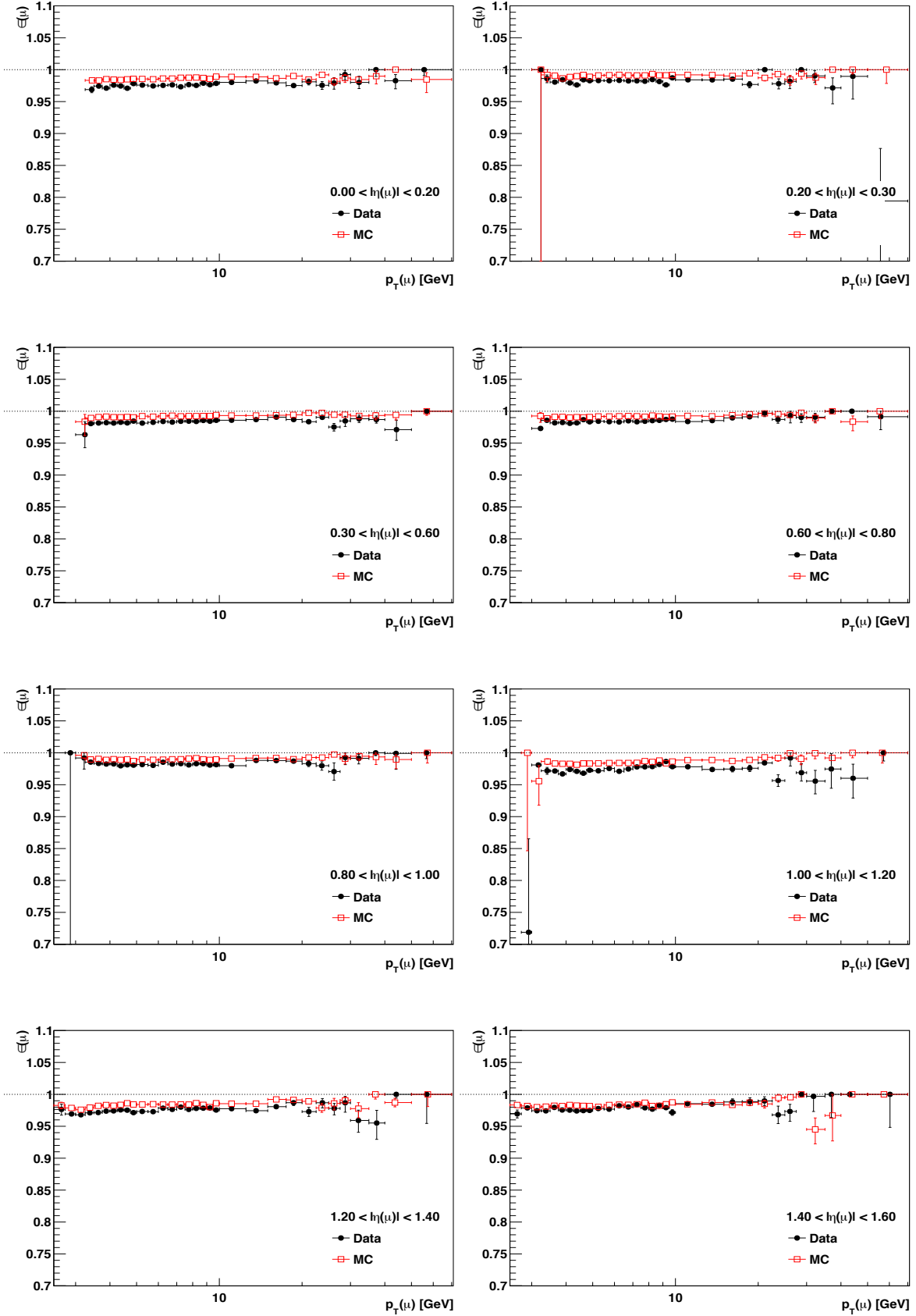


Figure 7.8: Efficiencies of the muon tracking quality cuts as a function of p_T for several $|\eta|$ bins calculated for all dimuon pairs.

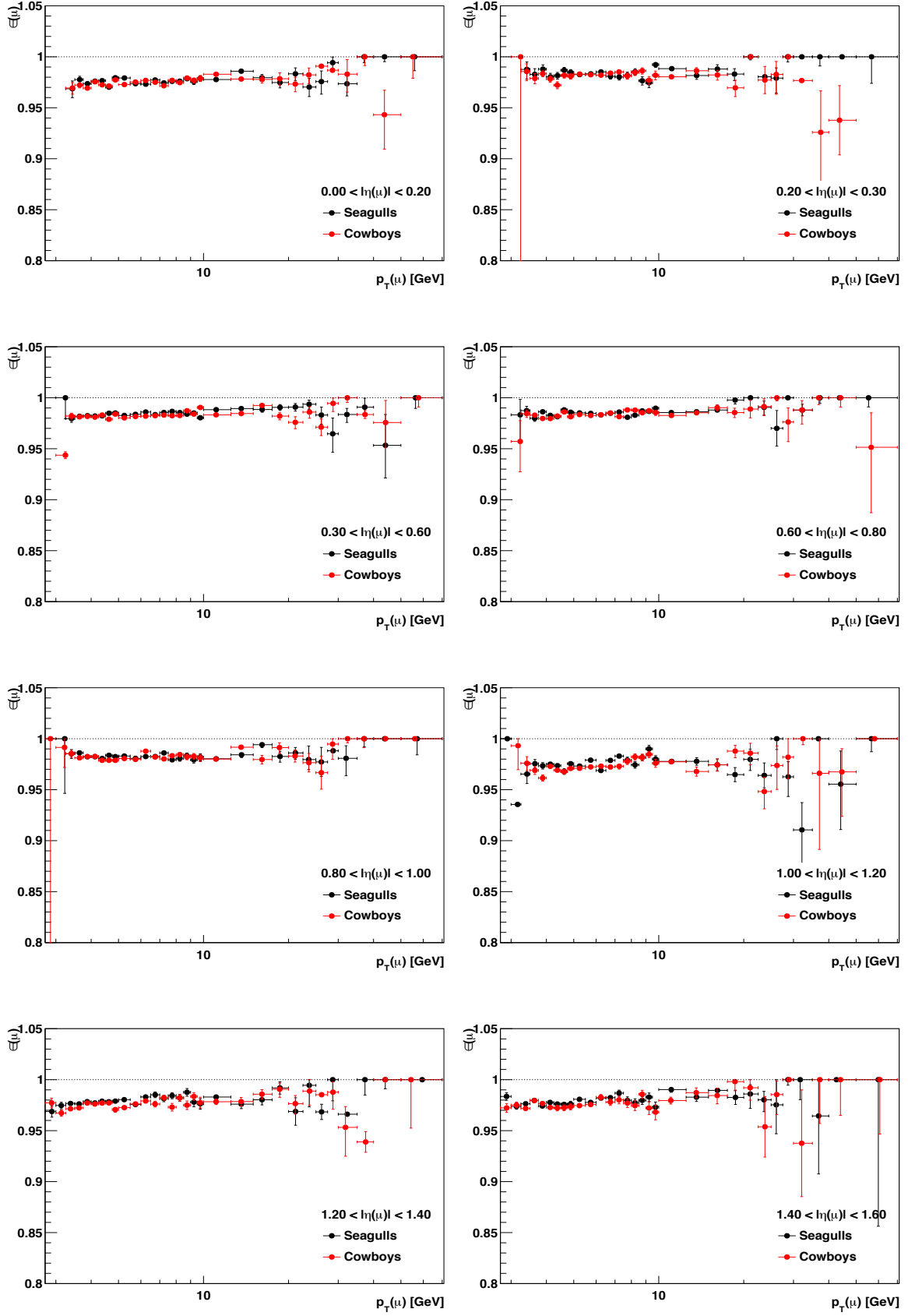


Figure 7.9: Data-driven efficiencies of the muon tracking quality cuts for seagull and cowboy dimuons as a function of p_T for several $|\eta|$ bins.

7.5 L1·L2 Efficiency

The setup of the L1·L2 trigger efficiency is similar to the offline muon reconstruction efficiency and uses HLT_MuX_TrackY_Jpsi triggers, in which tags are matched to the Mu5 leg or the Mu7 leg, respectively. The probes are matched to the online track of the efficiency trigger and have to fulfill all the criteria of a soft muon. Furthermore, passing probes are requested to pass the L2 filter of the dimuon trigger. As already mentioned in Sec. 7.1, due to L1·L2 trigger inefficiencies, differences for seagull and cowboy dimuons are expected, as seen in 2011 [77]. Figures 7.11 and 7.12 show the efficiencies for seagull and cowboy dimuons. Cowboy dimuons have slightly worse efficiencies compared to seagull dimuons, as shown in Fig. 7.13. This fact is confirmed by MC seagull/cowboy dimuon ratios (Fig. 7.14). MC efficiencies suggest a drop for cowboys at higher p_T regions which is only poorly reproduced with data due to lack of statistics. However, MC samples provide good statistics and, thus, reliable efficiencies even for high p_T regions.

Figure 7.10 depicts the efficiencies for all dimuons. Seagull and cowboy dimuons reach the plateau at approximately $p_T = 6$ GeV. Data driven efficiencies have enough statistical accuracy and are sufficiently smooth. The turn-on curve reveals disagreements of data and MC, most pronounced at forward $|\eta|$. Up to $|\eta| = 1.4$ small deviations at mid p_T regions emerge.

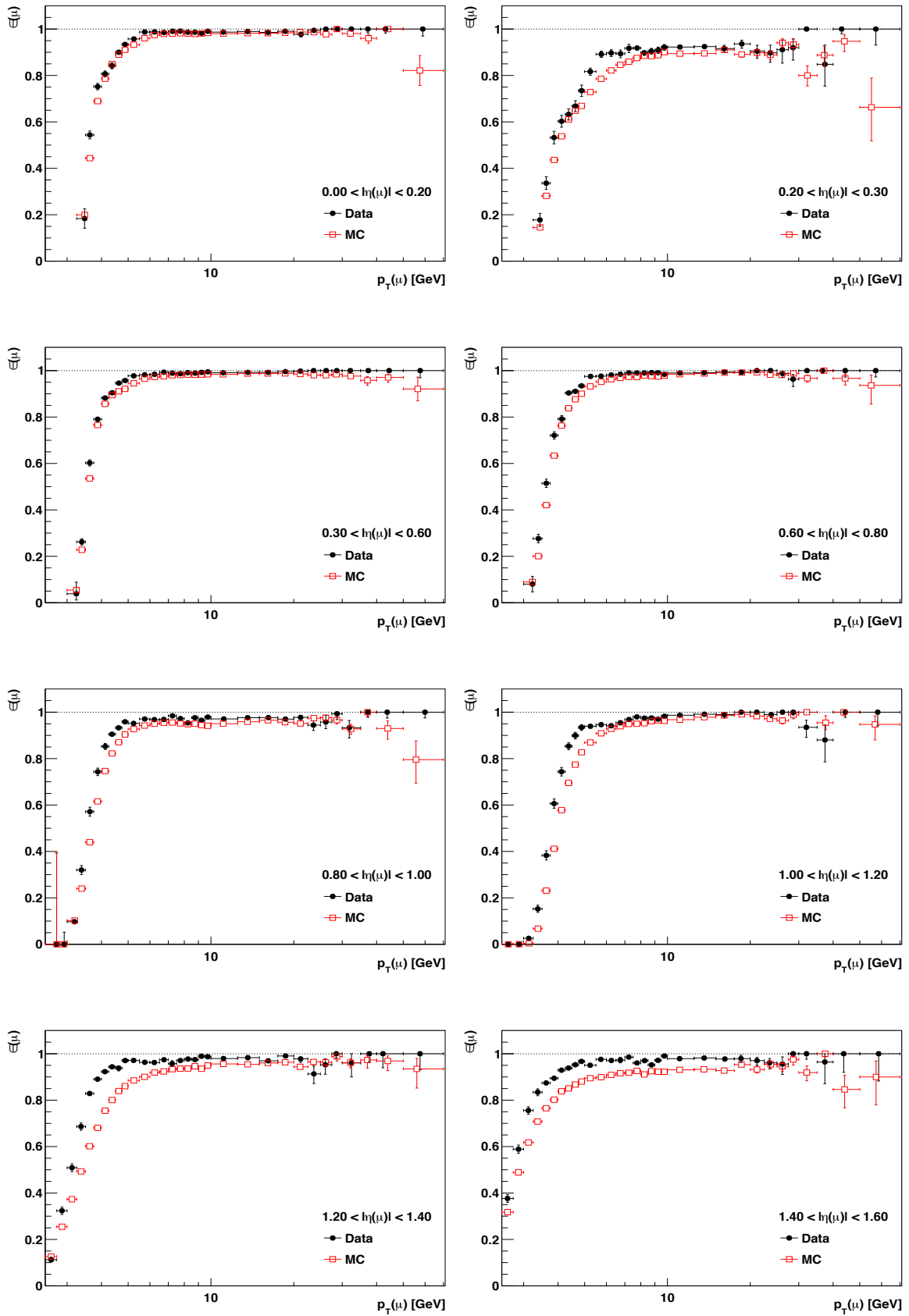


Figure 7.10: L1·L2 efficiencies as a function of p_T for several $|\eta|$ bins calculated for all dimuon pairs.

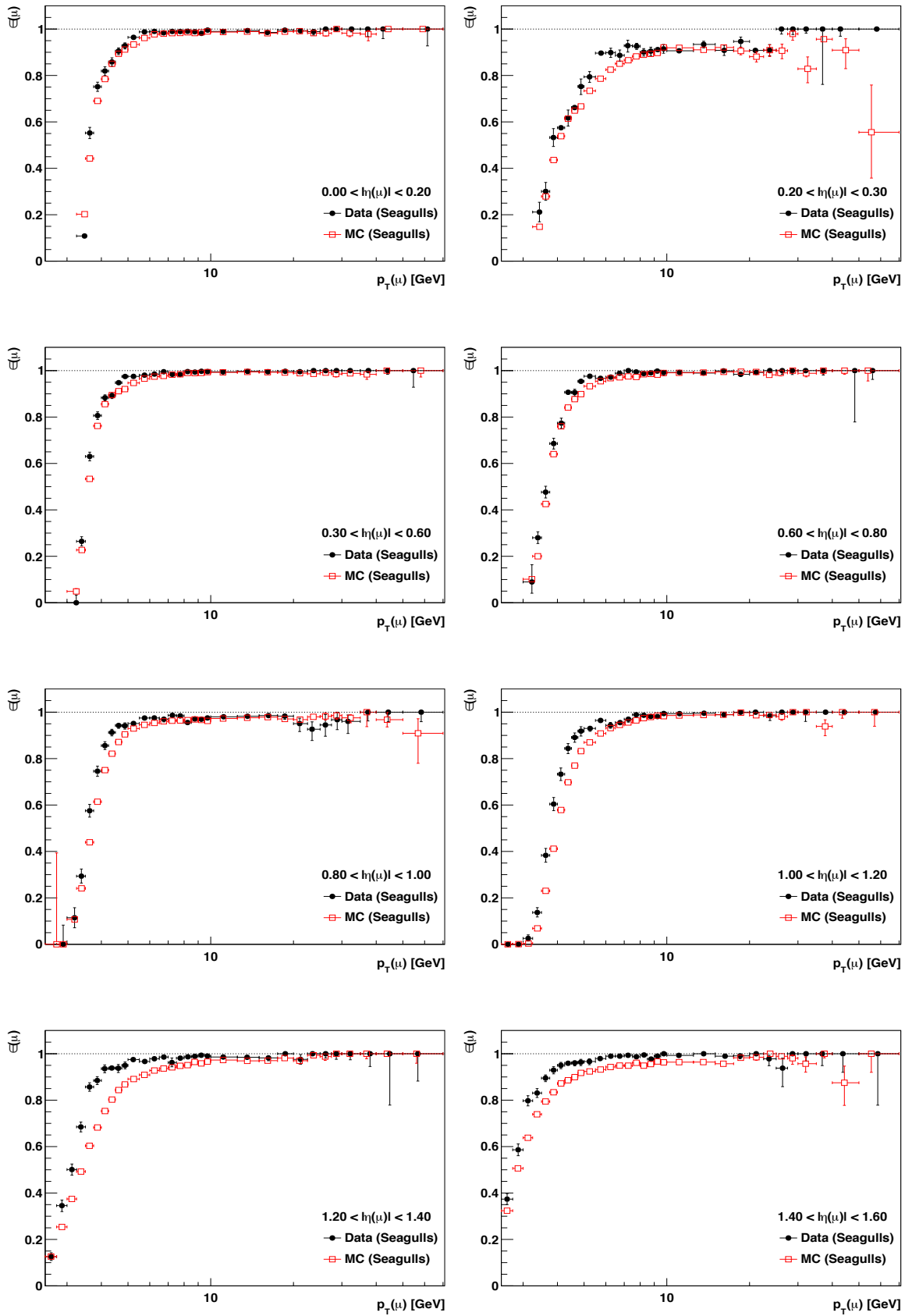


Figure 7.11: L1-L2 efficiencies as a function of p_T for several η bins calculated for seagull dimuons.

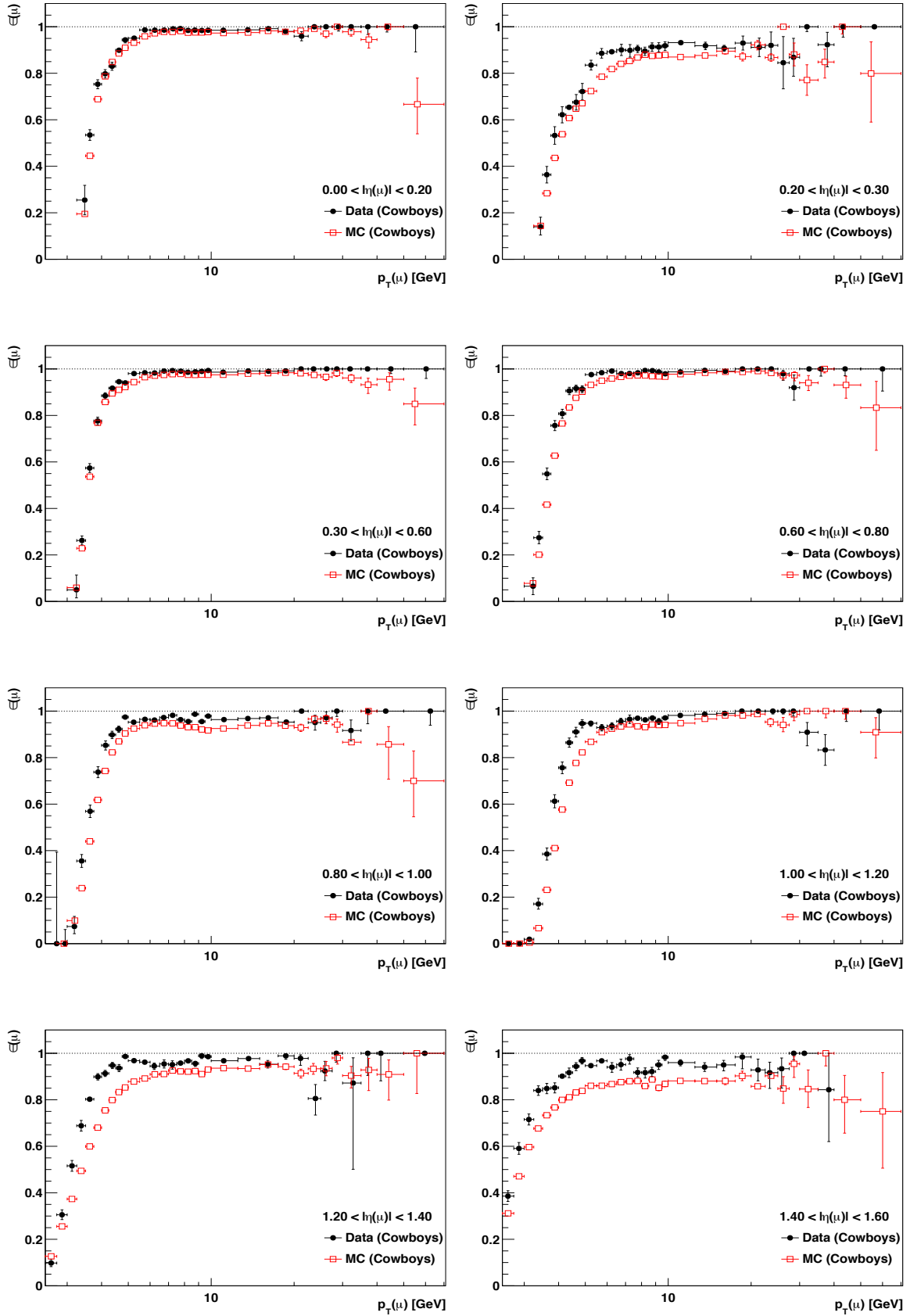


Figure 7.12: L1·L2 efficiencies as a function of p_T for several η bins calculated for cowboy dimuons.

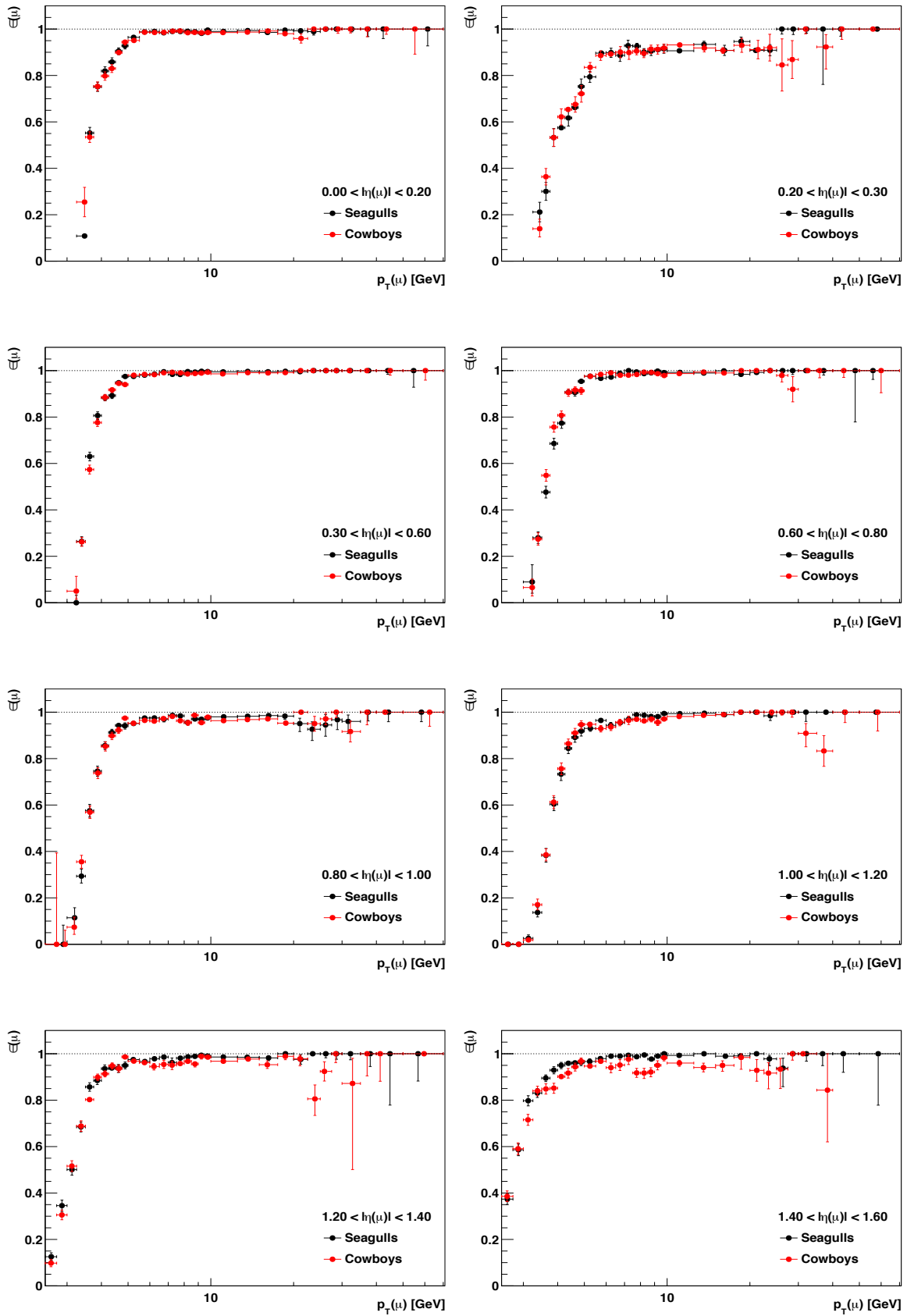


Figure 7.13: Data-driven L1·L2 efficiencies for seagull and cowboy dimuons as a function of p_T for several $|\eta|$ bins.

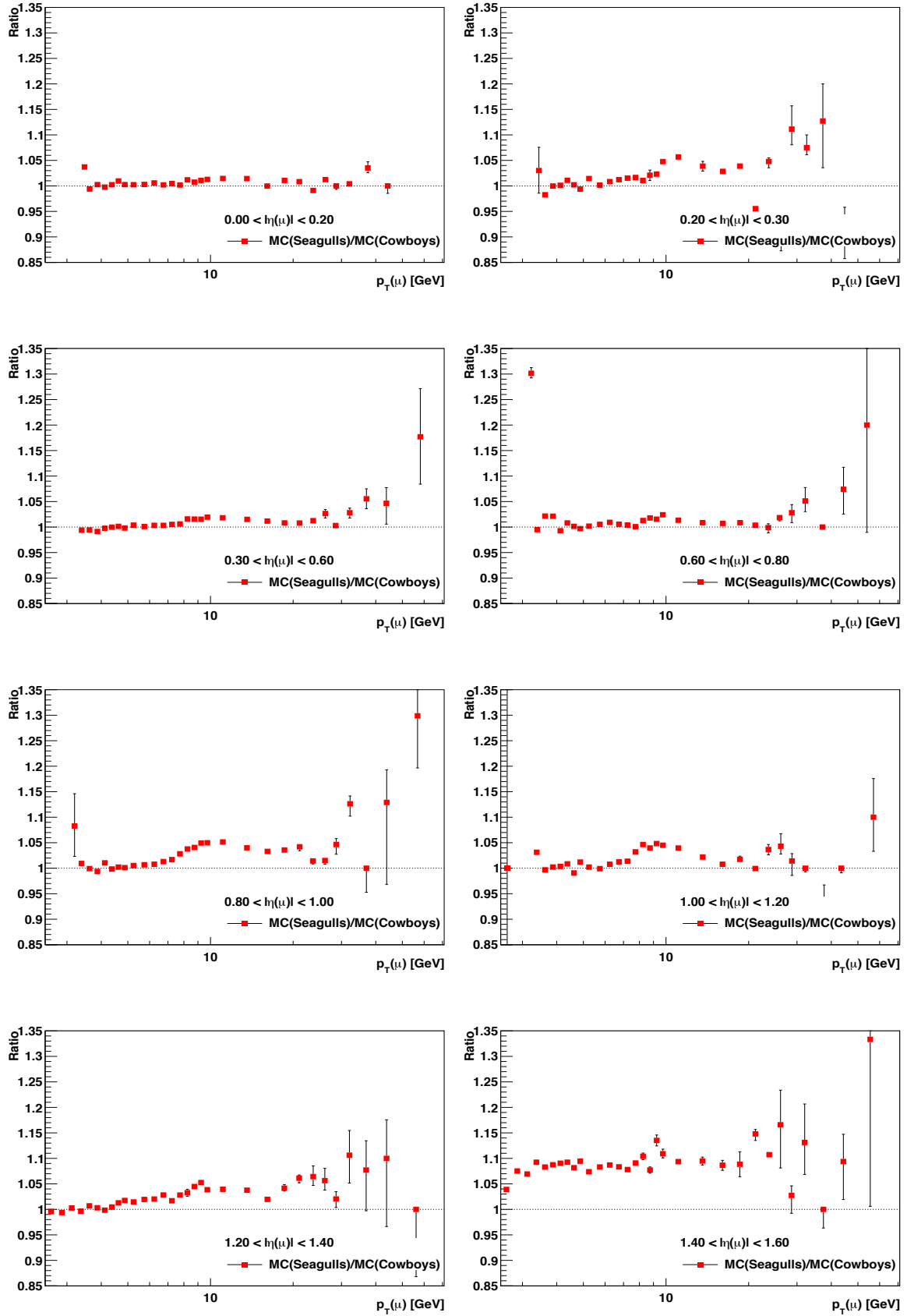


Figure 7.14: Ratio of MC driven L1·L2 efficiencies calculated for seagull dimuons over the one calculated for cowboy dimuons as a function of p_T for several $|\eta|$ bins. The error bars correspond to the first moment of the respective fraction.

7.5.1 Forward $|\eta|$ Region

For $|\eta| > 1.4$ the muons from cowboy pairs show decreased efficiencies from $p_T > 8$ GeV onwards. The MC based ratios of efficiencies also confirm a strong difference between seagull and cowboy dimuons (Fig. 7.15).

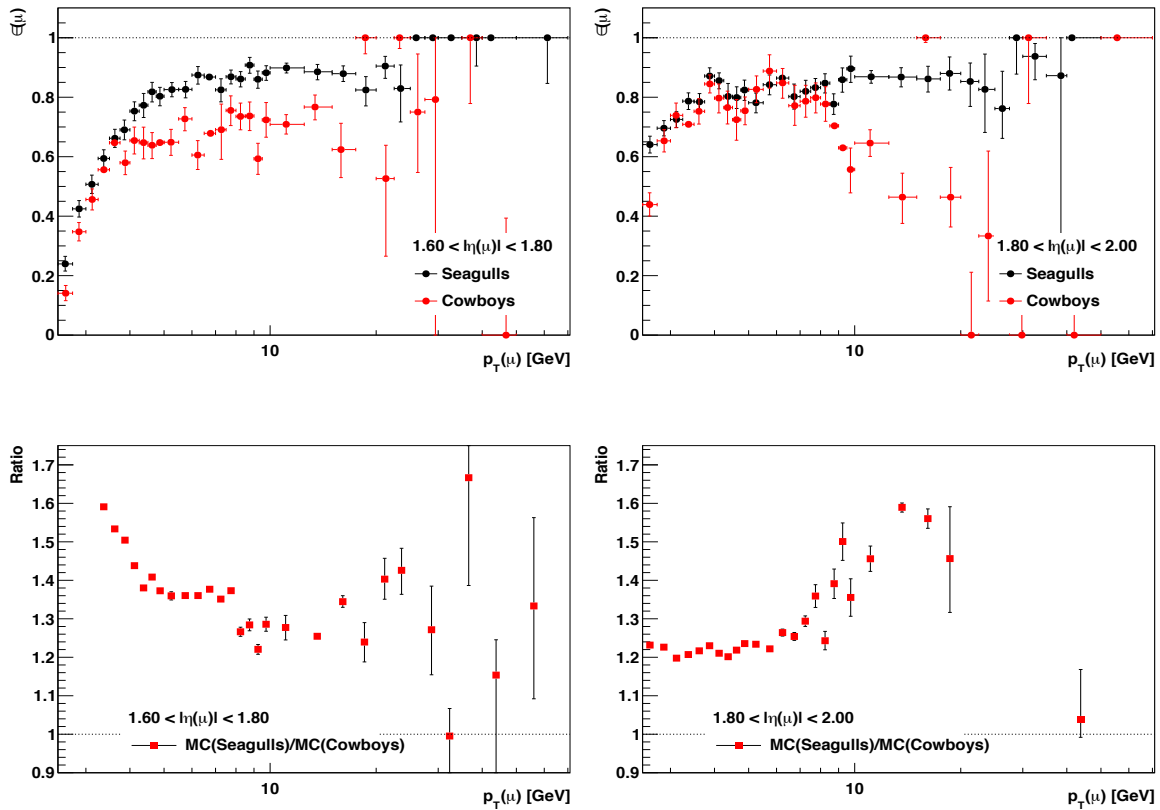


Figure 7.15: Data-driven L1·L2 efficiencies for seagull and cowboy dimuon as a function of p_T in forward $|\eta|$ bins (top). Ratio of MC driven L1·L2 efficiencies calculated for seagull dimuons over the one calculated for cowboy dimuons as a function of p_T in forward $|\eta|$ bins (bottom). The error bars correspond to the first moment of the respective fraction.

7.6 L3 Efficiency

The L3 trigger efficiency gives the probability of L2 muons passing the L3 reconstruction step. While tag muons are matched to the Mu5 leg of the *HLT_Mu5_L2Mu3_Jpsi* trigger, probe muons are matched to the L2Mu3 leg. Furthermore, probe muons have to be soft muons. The match of the passing probe muons is performed to a L3 muon which has previously passed the L2 filter, mentioned above, and has a transverse momentum $p_T > 3$ GeV. This setup does not include a test on the L3 related cuts on the vertex probability, which is therefore studied as a separate efficiency, namely the *dimuon vertex efficiency* discussed in Sec. 7.8.

Figure 7.16 shows the L3 efficiencies calculated for all dimuons. More plots can be found in Appendix A. The L3 efficiencies show a rather fast turn-on curve, reaching the plateau of close to 100% in most bins at $p_T \sim 5 - 6$ GeV. There are significant deviations between data and MC in the turn-on region (worse than for L1-L2 efficiencies).

η differential efficiencies show a drop in the efficiency around $|\eta| = 1$. Therefore, studies were conducted using very fine bins in η . The results are shown in Fig. 7.17. Up to ~ 4 GeV, muons display different efficiencies depending on their dimuon type. In the $0.2 < |\eta| < 0.3$ region, this discrepancy continues up to 8 GeV. The drop in efficiency around $|\eta| = 1$ is possibly related to the pileup dependence of the L3 in the overlap region. This effect is known and will be corrected for data taking in 2015. Figures 7.18 and 7.19 show the dependence of the L3 efficiencies on the $+\eta$ or $-\eta$ regions for seagull and cowboy dimuons. There is a small difference in efficiency for $+\eta$ and $-\eta$ at very low p_T , which is not reproduced for higher values of p_T .

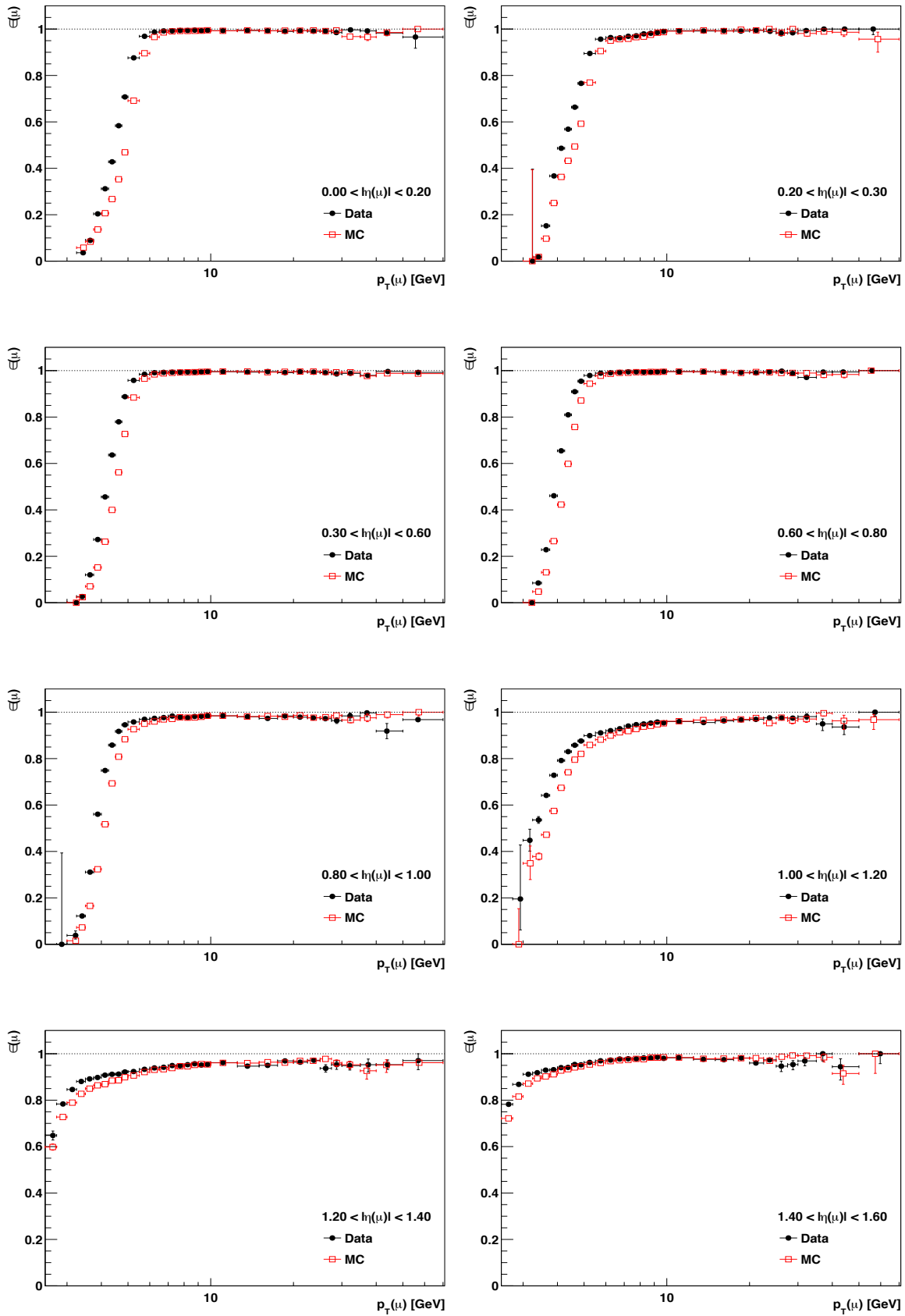


Figure 7.16: L3 efficiencies as a function of p_T for several $|\eta|$ bins calculated for all dimuon pairs.

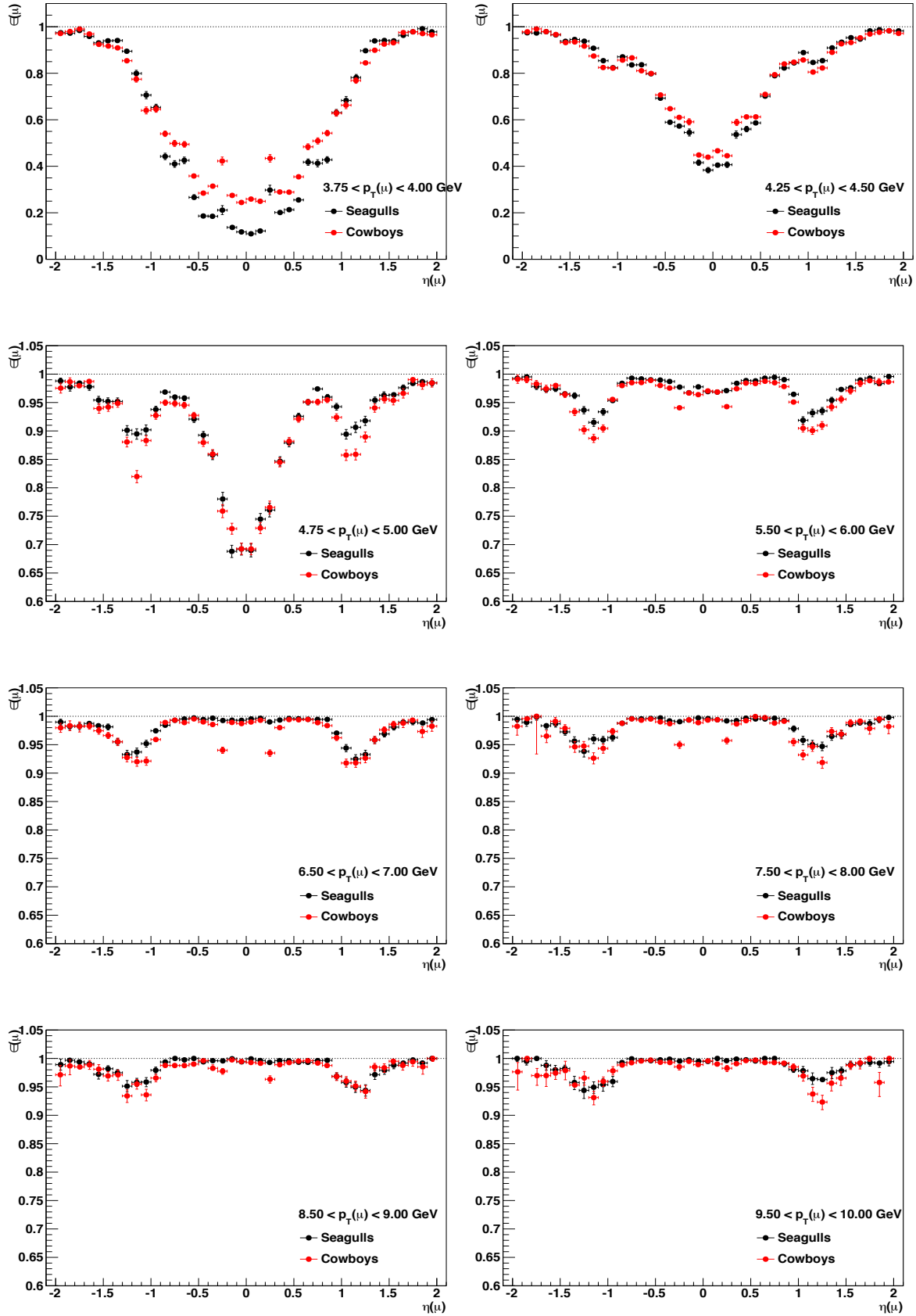
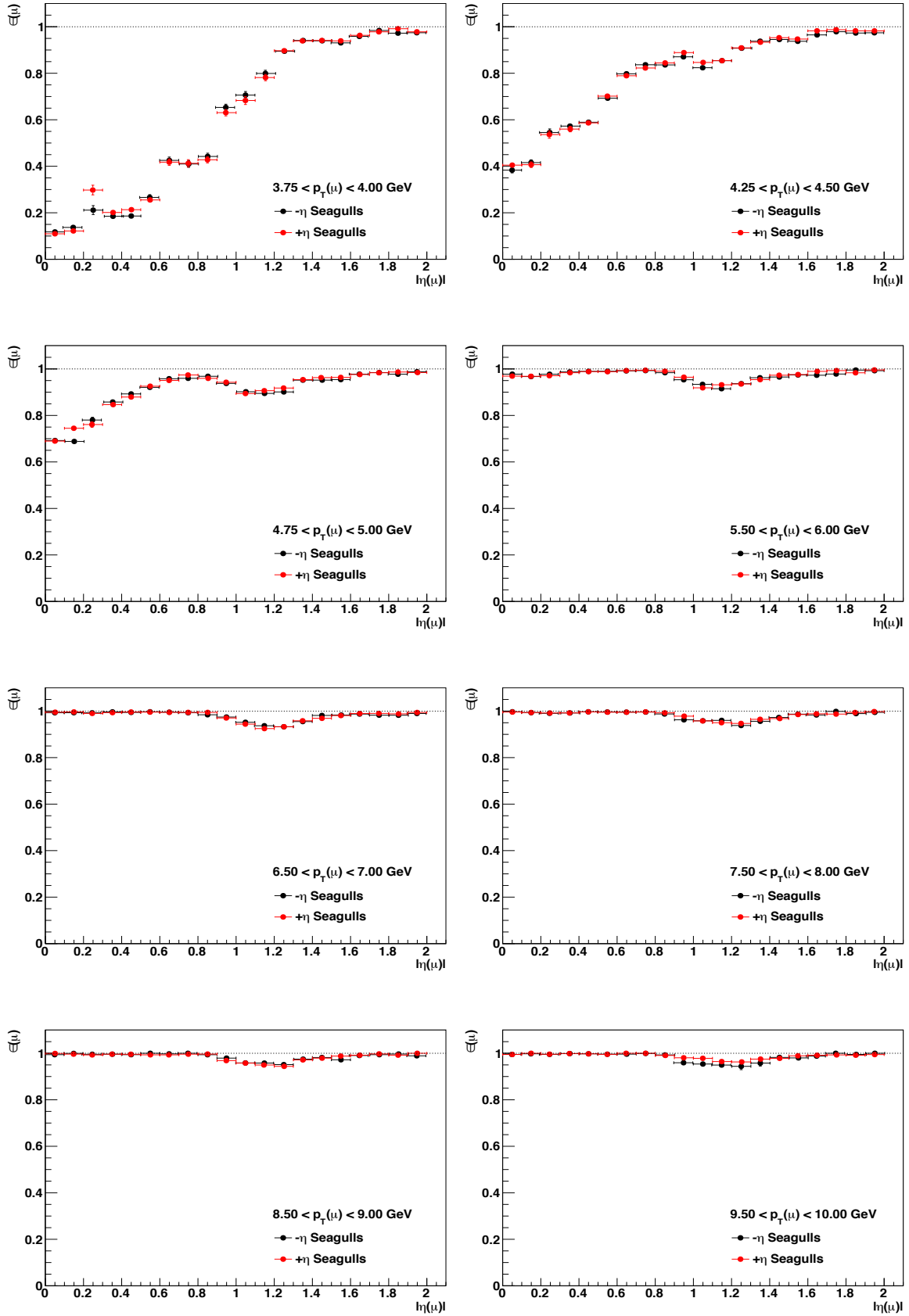


Figure 7.17: L3 efficiencies for seagull and cowboy dimuons as a function of η for several p_T bins.

Figure 7.18: L3 efficiencies for seagull dimuons as a function of $\pm\eta$ for several p_T bins.

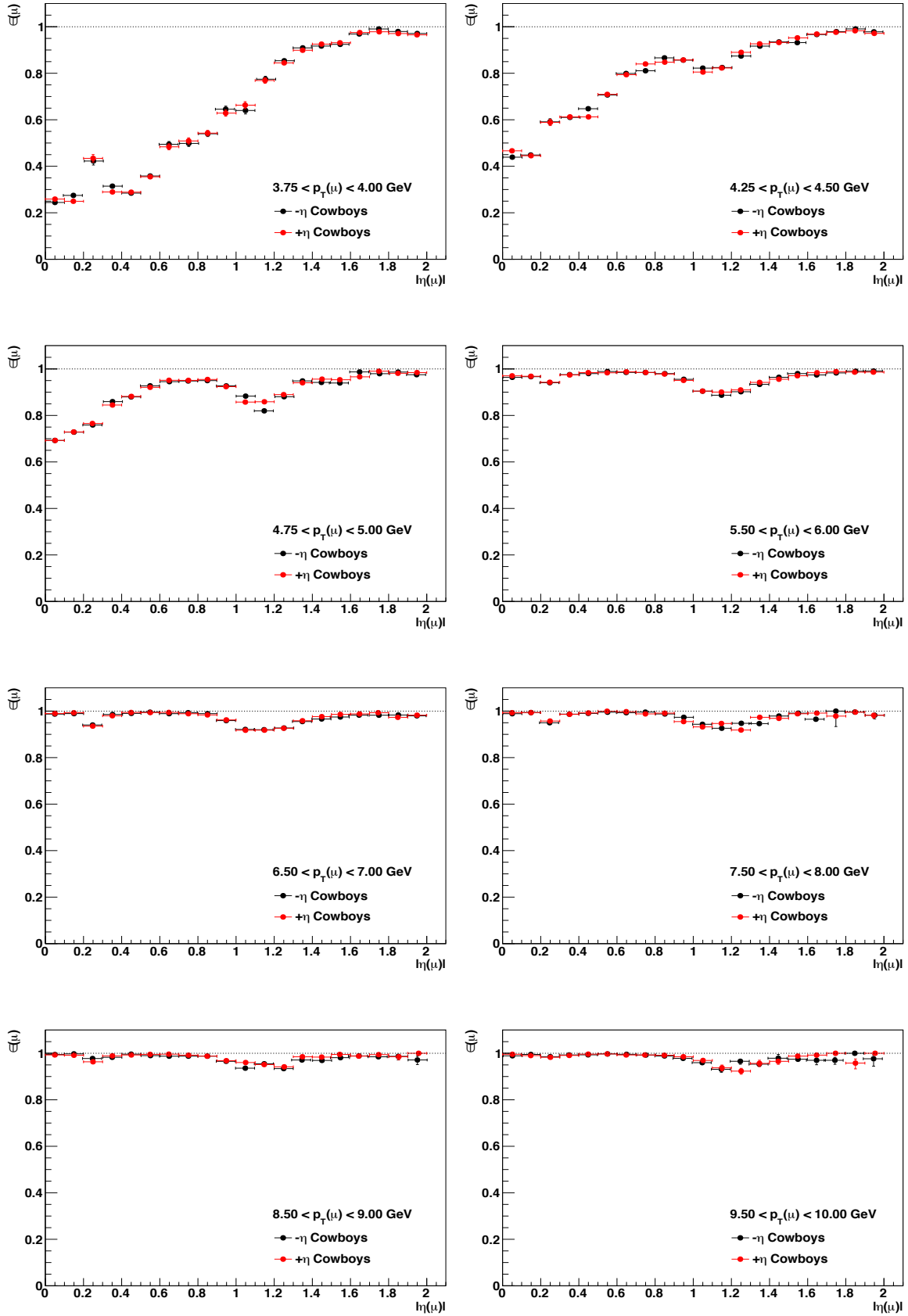


Figure 7.19: L3 efficiencies for cowboy dimuons as a function of $\pm\eta$ for several p_T bins.

7.7 Total Single Muon Efficiency

As already mentioned in Sec. 7.1, the total single muon efficiency is defined as:

$$\epsilon_{tot}(\mu) = \epsilon_{Track}(\mu) \cdot \epsilon_{MuonID}(\mu) \cdot \epsilon_{MuQual}(\mu) \cdot \epsilon_{L1\cdot L2}(\mu) \cdot \epsilon_{L3}(\mu) \quad (7.3)$$

MC based efficiencies are always used in case of the offline muon reconstruction efficiency.

Figure 7.20 shows the total single muon efficiency for all dimuons. The plateau is reached at approximately 6 GeV and the efficiencies have a constant value of about 90 % afterwards. Figures 7.21 and 7.22 show the total single muon efficiencies for seagull and cowboy dimuons. In general, data and MC efficiencies are quite consistent except for more pessimistic MC efficiencies in low p_T and higher η regions ($\eta > 0.6$). This results from deviations in the turn-on curves of the L1·L2 and L3 efficiencies. Figure 7.23 shows the comparison between seagull and cowboy dimuons. Differences between seagull and cowboy dimuons result from the differences at L1·L2; MC seagull/cowboy dimuon ratios reflect deviations in the turn-on curve as well as in mid and high p_T regions (see Fig. 7.24).

Possible impacts on the polarization analysis resulting from different efficiencies of seagull and cowboy dimuons are discussed in Chap. 9.

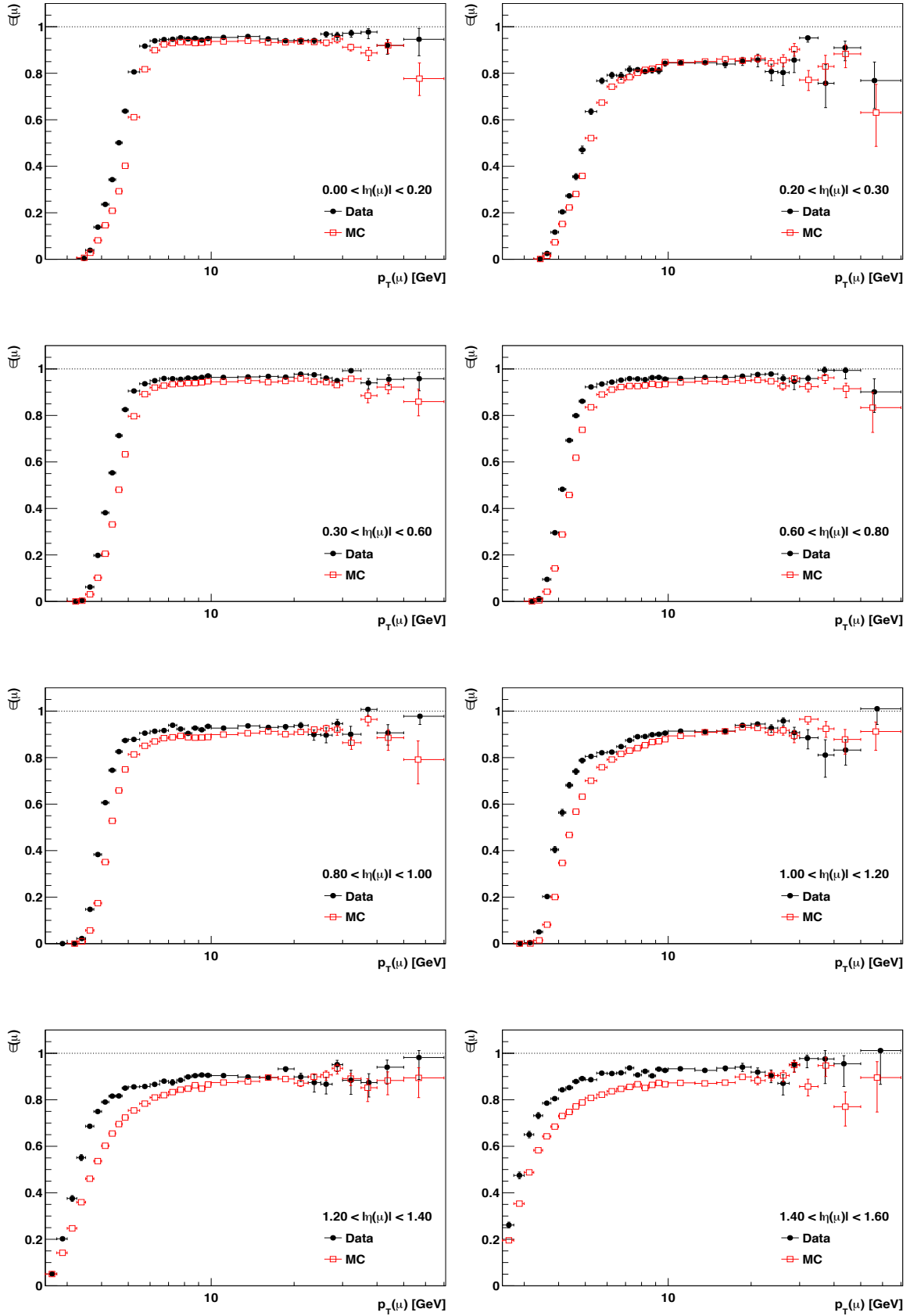


Figure 7.20: Total single muon efficiencies as a function of p_T for several $|\eta|$ bins calculated for all dimuon pairs.

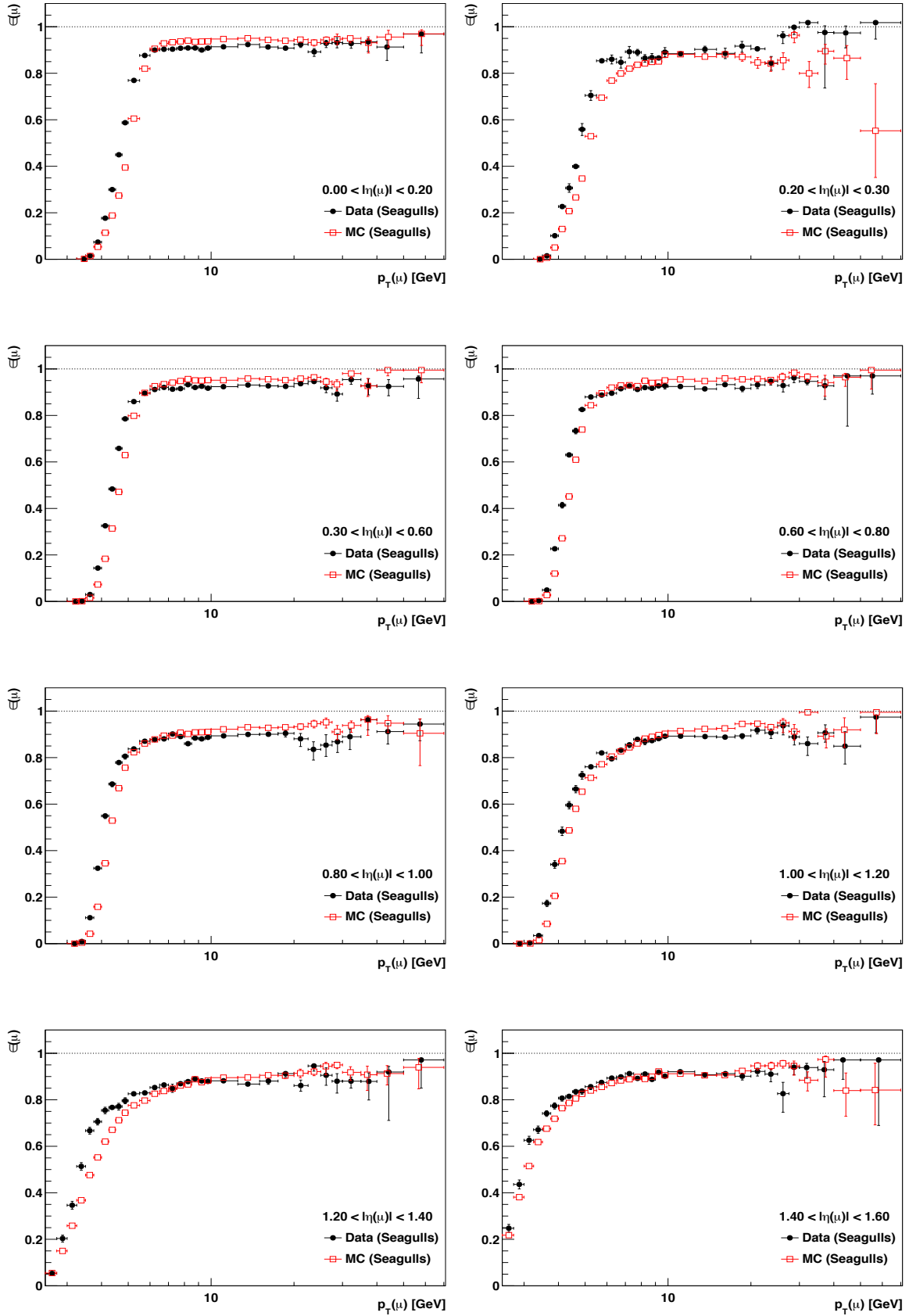


Figure 7.21: Total single muon efficiencies as a function of p_T for several $|\eta|$ bins calculated for seagull dimuons.

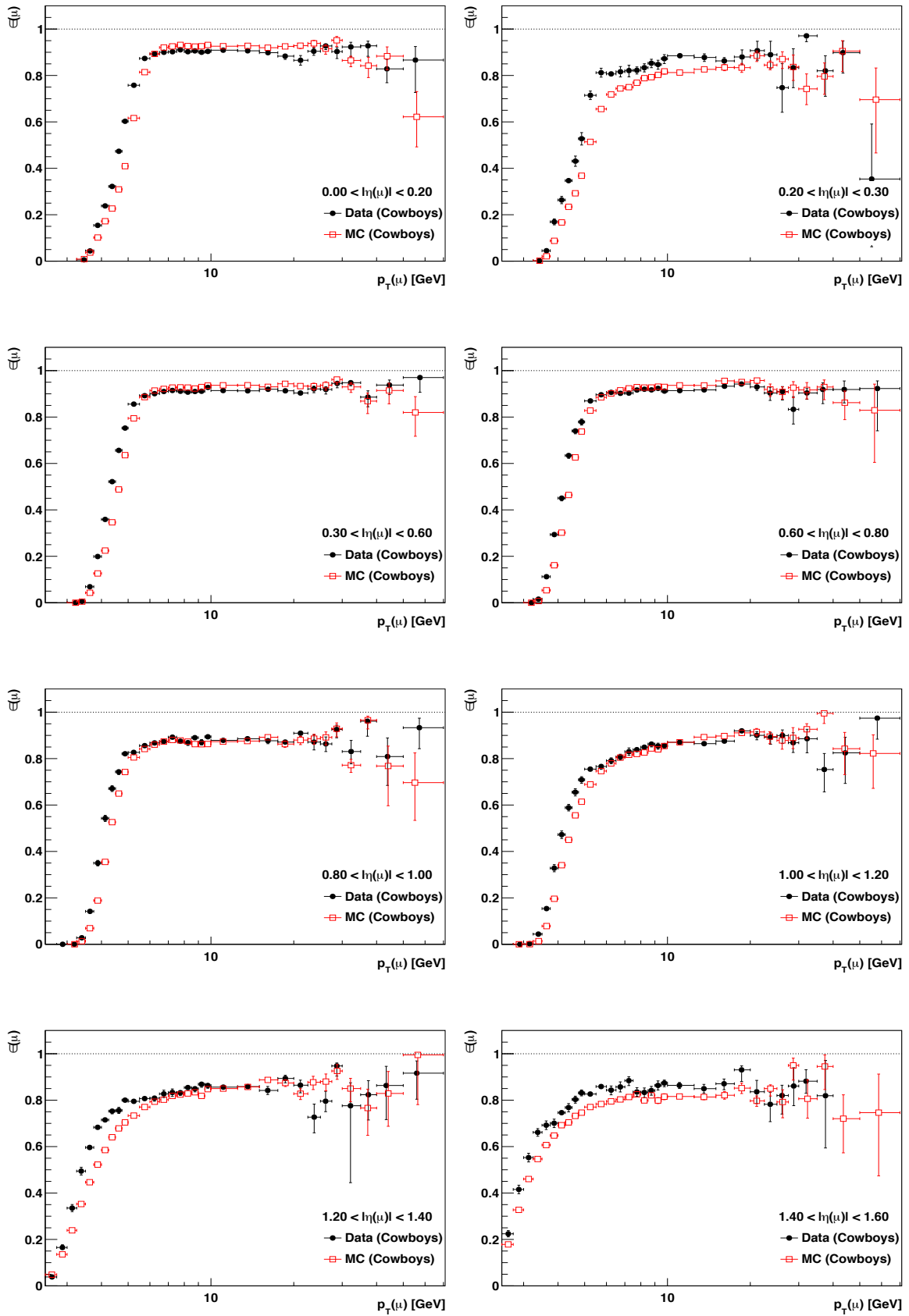


Figure 7.22: Total single muon efficiencies as a function of p_T for several $|\eta|$ bins calculated for cowboy dimuons.

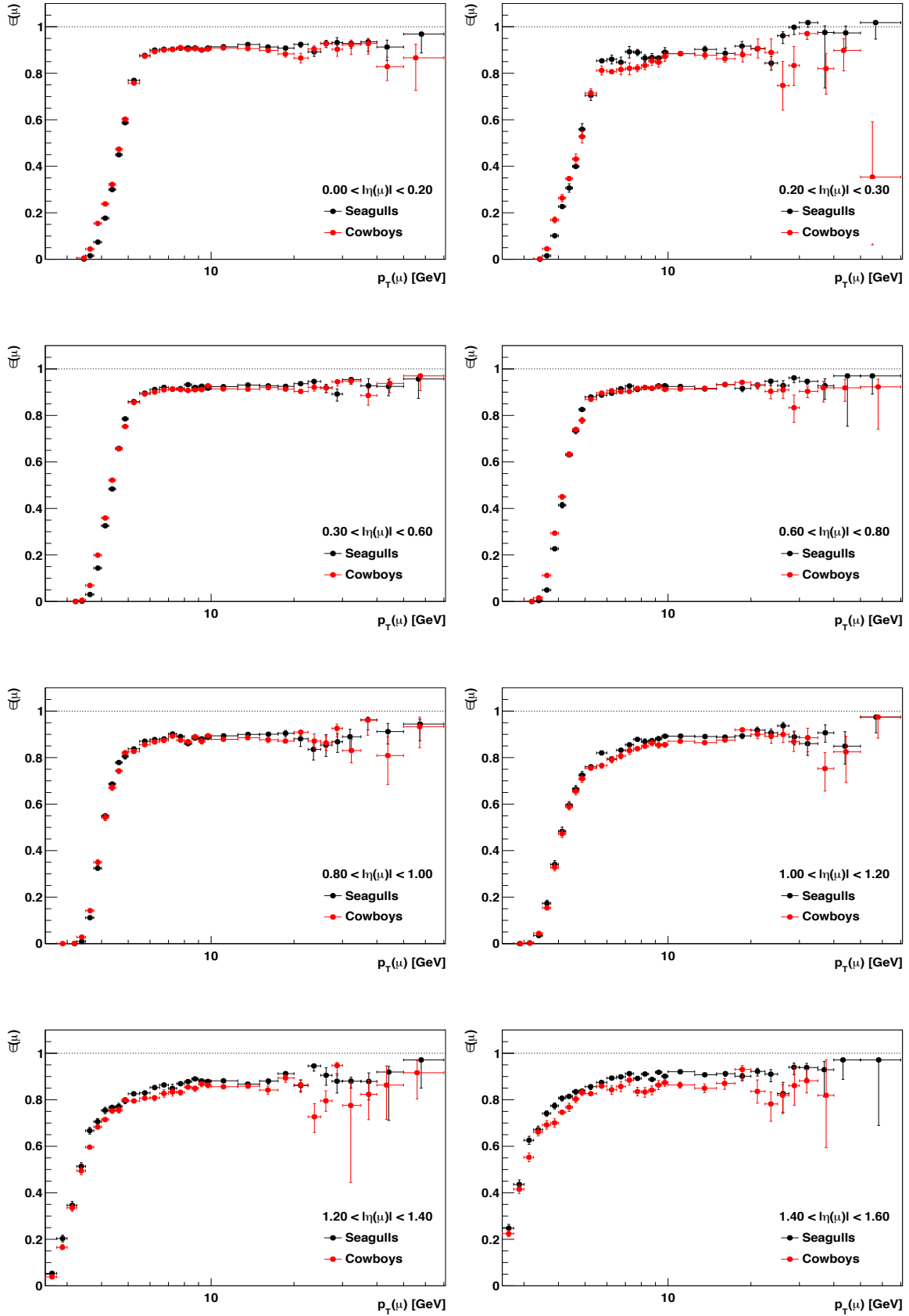


Figure 7.23: Data-driven total single muon efficiencies for seagull and cowboy dimuons as a function of p_T for several $|\eta|$ bins.

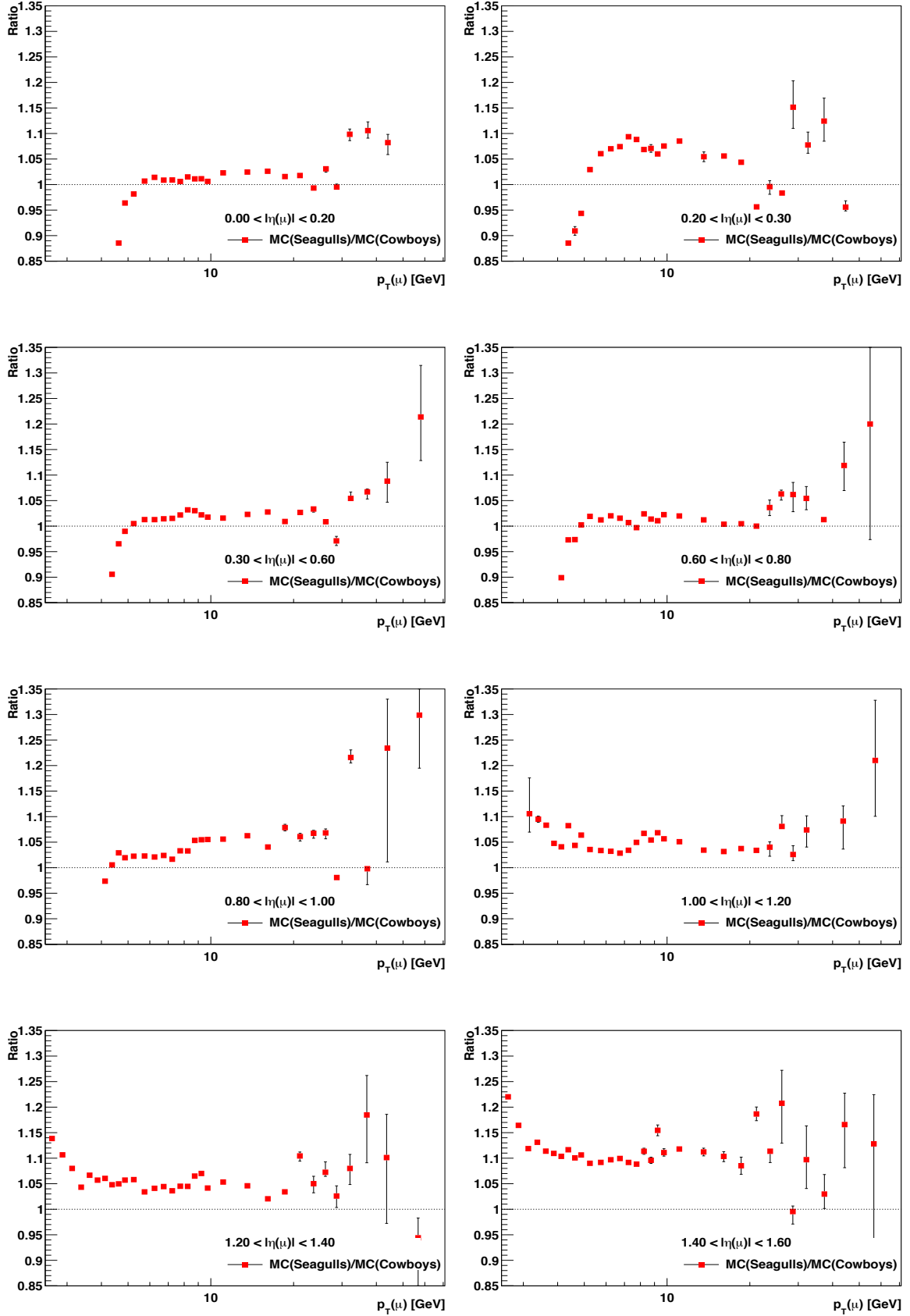


Figure 7.24: Ratio of MC based total single muon efficiencies for seagulls over the one for cowboys as function of p_T for several $|\eta|$ bins. The error bars correspond to the first moment of the respective fraction.

7.7.1 The MC-truth Approach

MC-truth efficiencies are calculated using the TnP framework, but instead of using a simultaneous fit, the number of passing and failing probes is simply divided in order to obtain efficiencies (*cut and count method*). This method only provides reliable results using MC because the MC does not have background events. The MC-truth efficiencies are used to check the TnP fitting procedure. A very good agreement between the MC based TnP and the MC-truth efficiencies is reached for all $|\eta|$ and p_T bins, as shown in Fig. 7.25.

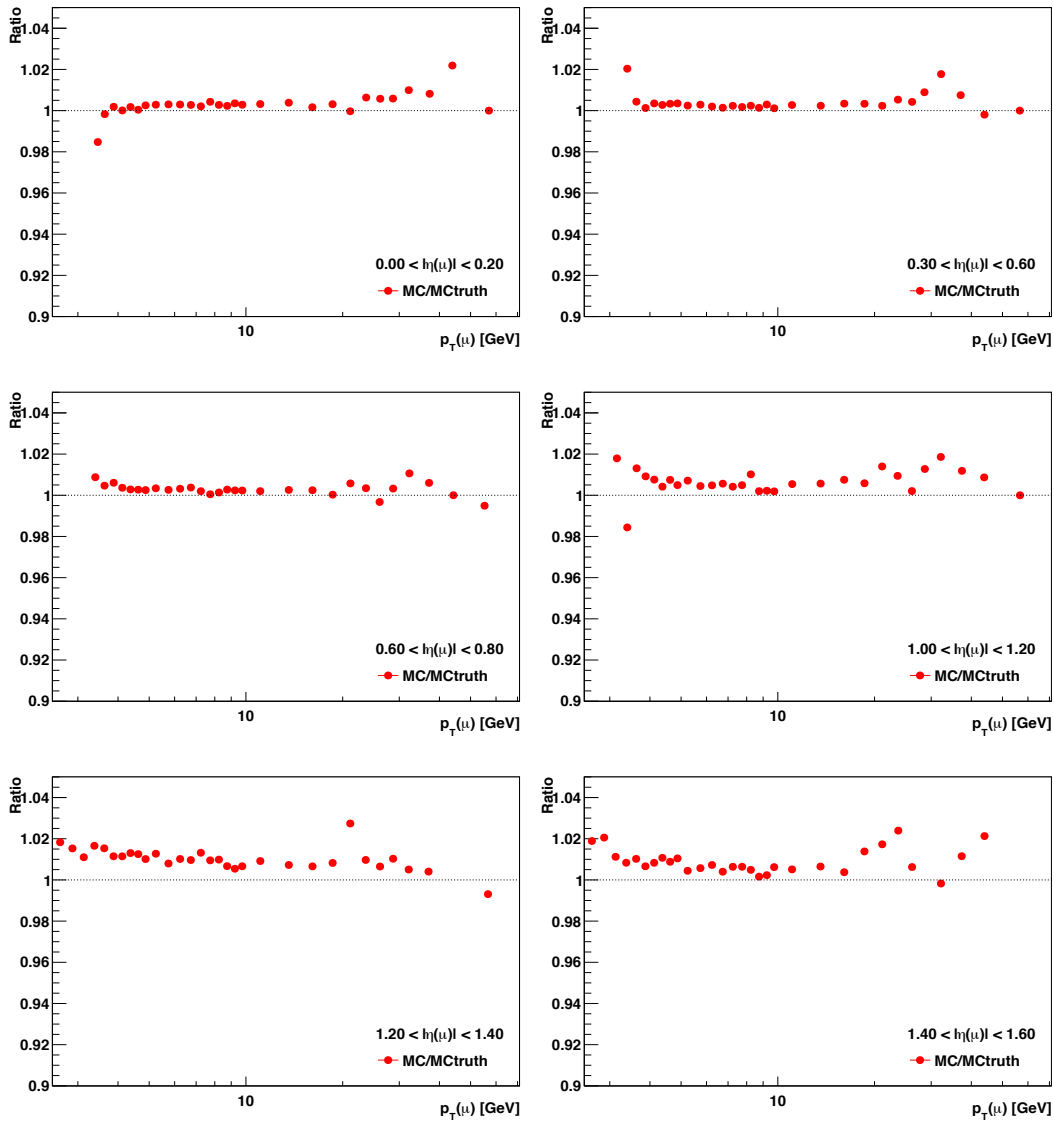


Figure 7.25: Ratio of MC based TnP efficiencies over MC-truth total single muon efficiencies calculated for all dimuons as function of p_T for several $|\eta|$ bins.

7.7.2 Pileup Studies

In data taken in 2012 at pp collisions at a center of mass energy $\sqrt{s} = 8$ GeV and a peak instantaneous luminosity of $\sim 7.67 \cdot 10^{33} \text{ cm}^2\text{s}^{-1}$, a non negligible amount of pileup interactions appeared. This is reflected in a distribution of the number of reconstructed vertices in the data sample, as shown in Fig. 7.26. The peak of the distributions shifts slightly with the run periods as the instantaneous luminosity is increased. The MC sample has a slightly shifted peak and a slightly different distribution at low p_T . The small difference in the data and MC samples shown in this figure is also responsible for the difference between data and MC in the efficiencies. If the MC would be reweighted according to data, this should be gone. In order to investigate possible pileup dependent inefficiencies, pileup studies for all four sequential efficiencies $\epsilon_{MuonID}(\mu)$, $\epsilon_{MuQual}(\mu)$, $\epsilon_{L1-L2}(\mu)$, $\epsilon_{L3}(\mu)$ are conducted. Only dimuons in the p_T range $7.5 \text{ GeV} < p_T < 70 \text{ GeV}$ and $|\eta|$ range $0.0 < |\eta| < 2.0$ are tested to disentangle inefficiencies coming from the turn-on region. The following binning in vertex numbers is chosen for the studies:

- number of vertices = 1, 3, 5, 7, 9, 11, 13, 15, 17, 19, 21, 23, 25, 27, 29, 31.

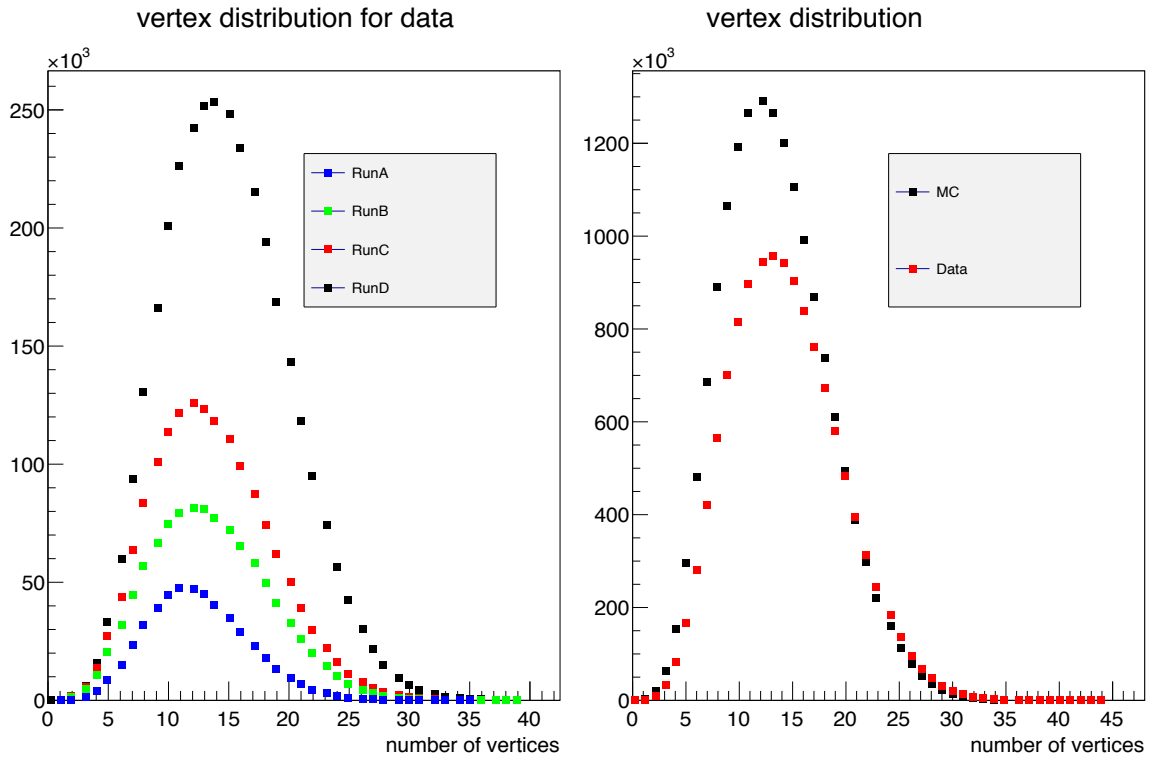


Figure 7.26: Distribution of the number of vertices for the different run periods in 2012 (left) and for all run periods in comparison to the MC simulation (right).

The efficiencies as a number of vertices are depicted in Fig. 7.27. The offline muon reconstruction efficiency shows no pileup dependence at all. The efficiency of muon quality cuts has a negligible dependence on the number of vertices on data. The L1·L2 efficiency shows a slight increase of $\sim 0.5\%$ between no pileup and 30 incident vertices. The decrease of the L3 efficiency as a function of the number of vertices is due to an error in the reconstruction algorithm in the overlap region and will be corrected for data taking in 2015. However, the pileup dependence is not negligible on L3 as for the efficiency of the muon quality cuts. Thus, the effect of low pileup and high pileup events on the polarization is discussed in Chap.9. Except for the efficiency of the tracking quality cuts, the MC based efficiency is lower than the data-driven one.

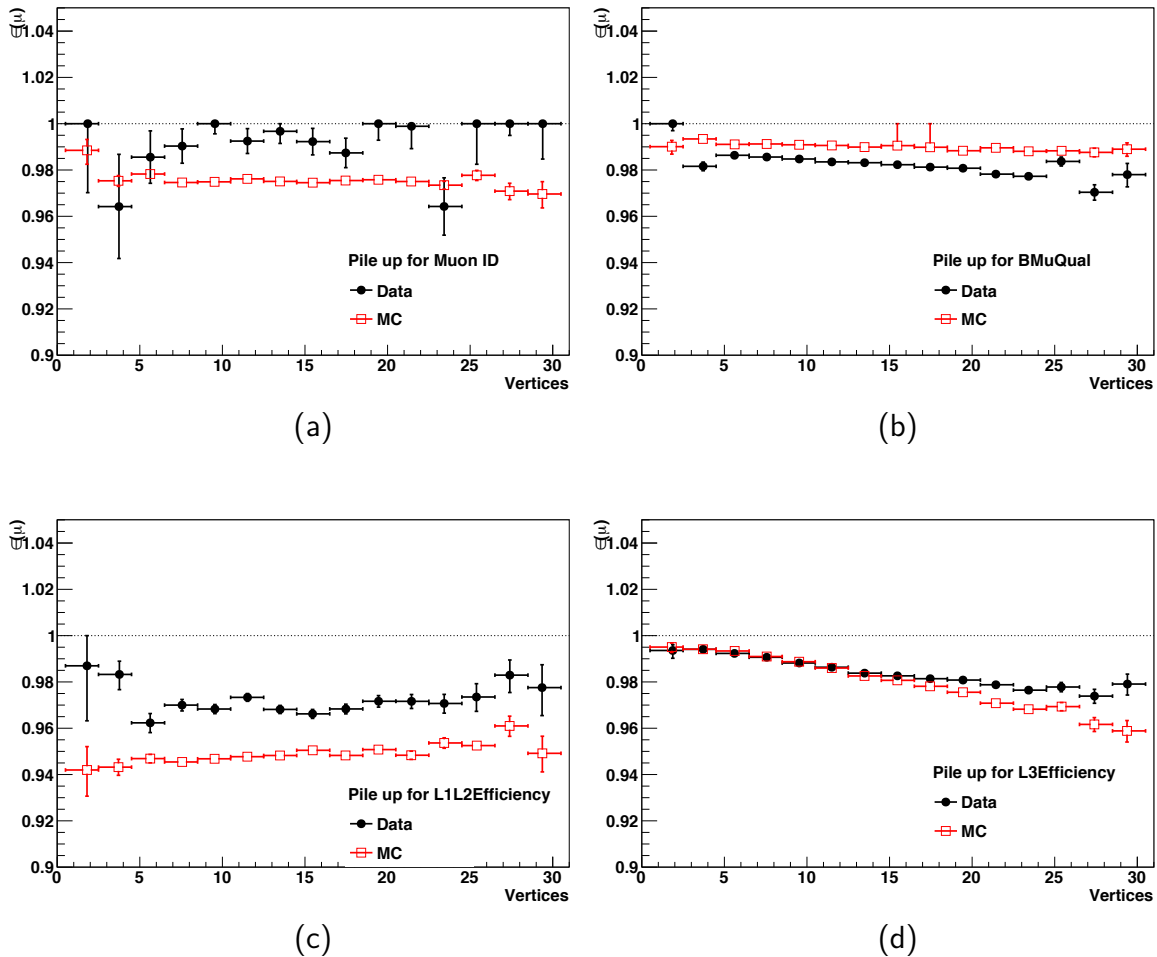


Figure 7.27: Offline muon reconstruction efficiency (a), efficiency of the muon quality cuts (b), L1·L2 efficiency (c) and L3 efficiency (d) as a function of the number of vertices for $7.5 \text{ GeV} < p_T < 70 \text{ GeV}$ and $|\eta| < 2.0$.

7.8 Dimuon Vertex Efficiencies

The last L3 filter which is used in all quarkonium triggers applies a cut on the dimuon vertex probability, and is called *dimuon vertexing module*. As a dimuon efficiency is determined instead of a single muon efficiency in this case, a slightly different procedure has to be applied. Instead of one muon being the tag and the other muon being the probe, the muon pair itself becomes the probe. As precondition dimuon pairs have to pass a special trigger that applies all the cuts of the dimuon trigger except for the dimuon vertexing module. Additionally, they have to be L3 muons and pass all the criteria of a soft muon. Passing probes then need to pass the last filter of the dimuon trigger path. Furthermore, both muons have to fulfill the following cuts that define a region where the single muon efficiencies are reliable:

$$\begin{aligned}
 |\eta| < 1.2 &\rightarrow p_T < 4.5 \text{ GeV} \\
 1.2 < |\eta| < 1.4 &\rightarrow p_T < 3.5 \text{ GeV} \\
 1.4 < |\eta| < 1.6 &\rightarrow p_T < 3.0 \text{ GeV}
 \end{aligned}
 \tag{7.4}$$

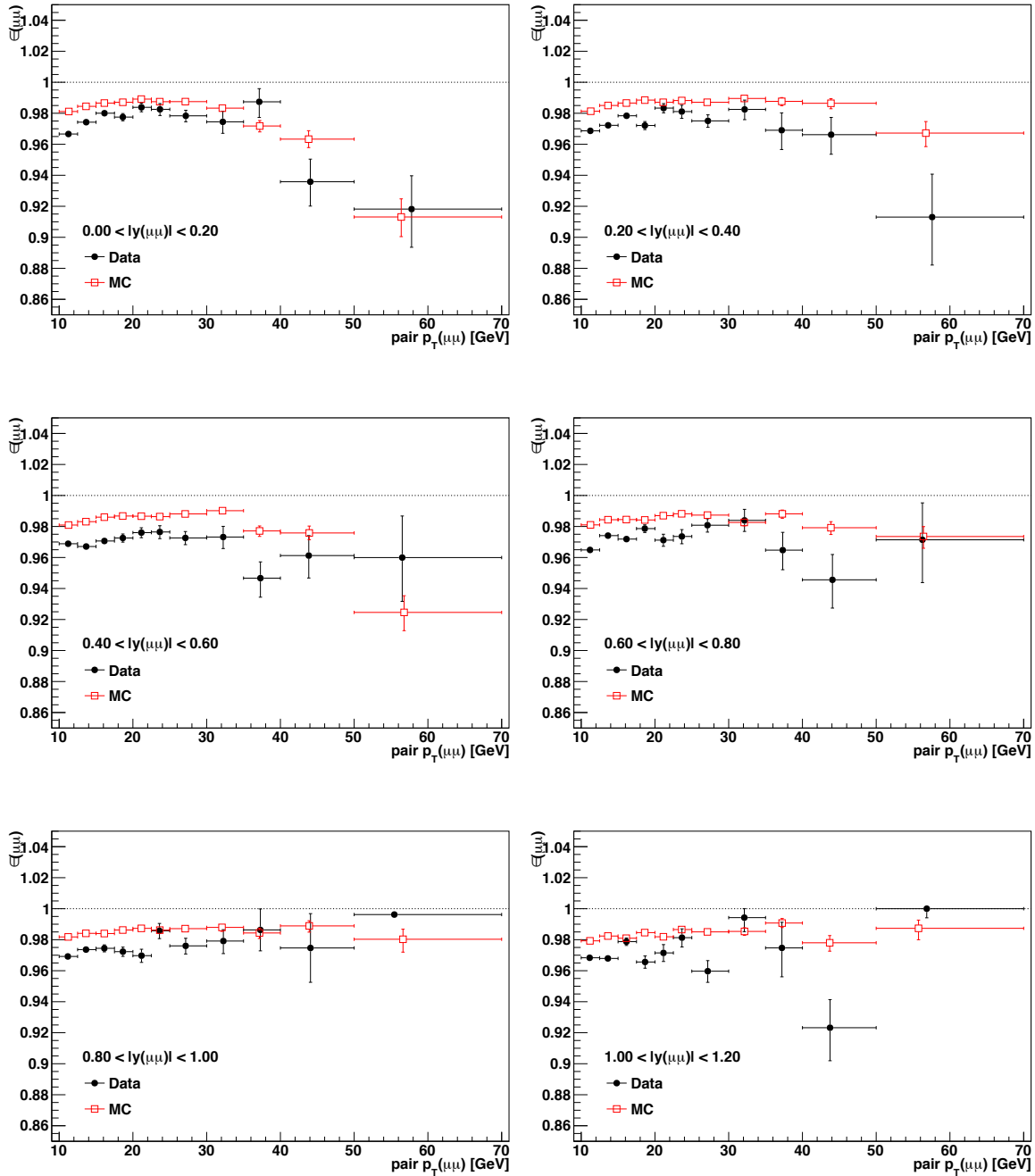
As muon pair efficiencies are investigated, a binning depending on dimuon p_T and dimuon $|y|$ is chosen:

- dimuon p_T : 10., 12.5, 15., 17.5, 20., 22.5, 25., 30., 35., 40., 50., 70.
- dimuon $|y|$: 0., 0.2, 0.4, 0.6, 0.8, 1., 1.2

In order to better see modulations of the efficiencies on the polarization, the dimuon vertex efficiencies are also calculated as a function of $\cos(\vartheta)$ and φ in the PX frame.

- $\cos(\vartheta)$: -1, -0.75, -0.5, -0.25, 0, 0.25, 0.5, 0.75, 1.
- φ : -180, -135, -112.5, -90, -77.5, -45, 0, 45, 77.5, 90, 112.5, 135, 180

The dimuon vertex efficiencies as a function of p_T and in different $|y|$ bins are shown in Fig. 7.28. The MC based efficiencies show the same trend as the data-driven ones, but are about 2% higher. The highest p_T bin ($50 < p_T < 70$ GeV) reflects an efficiency decrease for both data and MC. This study has also been conducted for seagull and cowboy dimuons separately. The results can be found in Appendix A. Figure 7.29 shows the $\cos(\vartheta)$ and φ differential vertex efficiencies in the PX frame. The efficiencies are relatively flat in $\cos(\vartheta)$ and φ , although two slight modulations at $\varphi_{PX} \sim \pm 50^\circ$ emerge. However, the effect of the dimuon vertex efficiency on the polarization was shown to be small and does not introduce any fake polarization.

Figure 7.28: Vertex efficiency as a function of dimuon p_T for several bins of dimuon $|y|$.

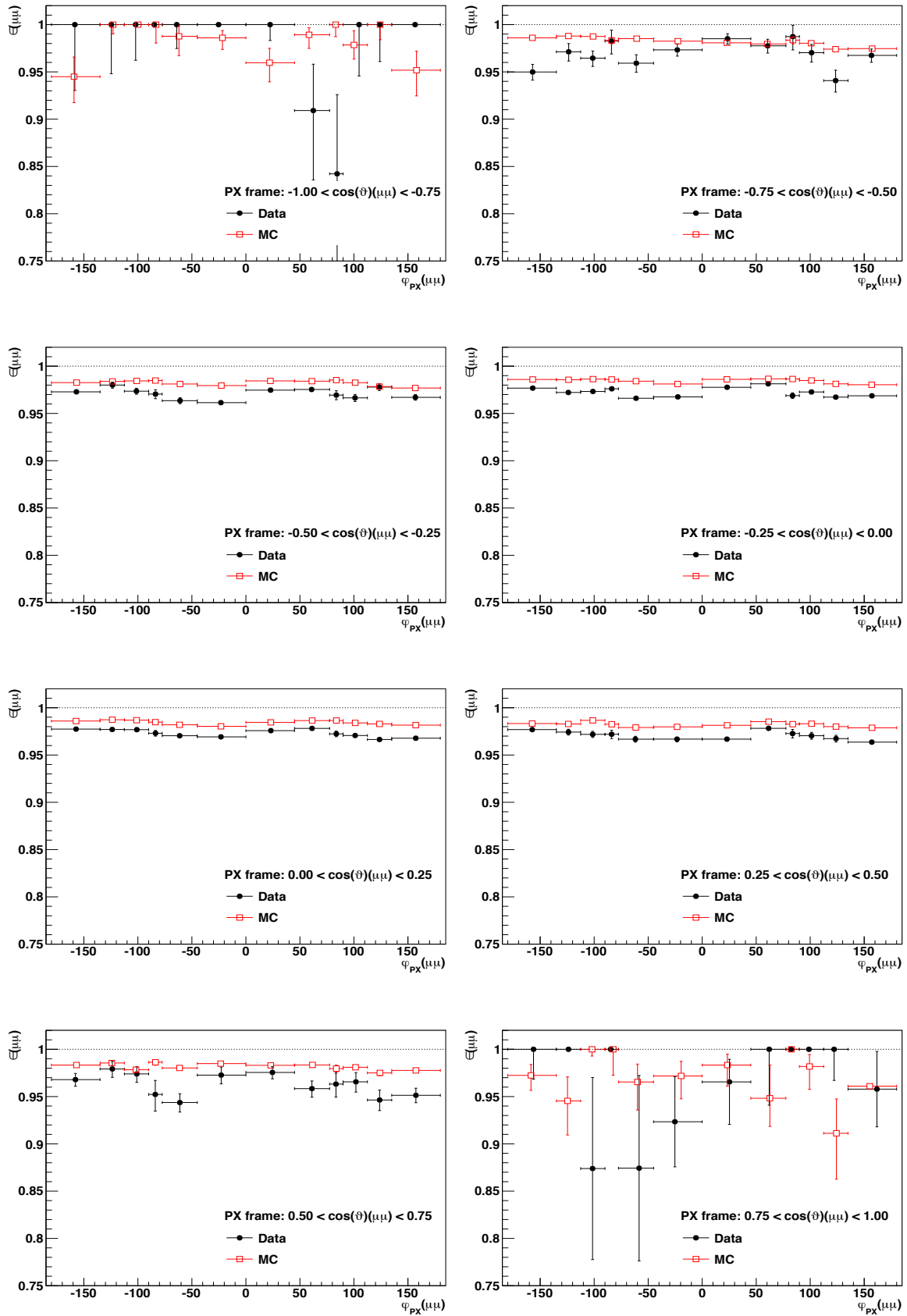


Figure 7.29: Vertex efficiency as a function of φ for several bins of $\cos\theta$ in the PX frame.

8 Muon Pair Correlations

The total dimuon detection efficiency cannot be calculated as a simple product of single muon efficiencies due to muon pair correlations. Instead, muon pair correlations as well as dimuon vertex efficiencies have to be included. It can be written as Eq. 6.7:

$$\epsilon_{\mu\mu}(\vec{p}_1, \vec{p}_2) = \epsilon_{\mu 1}(\vec{p}_1) \cdot \epsilon_{\mu 2}(\vec{p}_2) \cdot \epsilon_{Vtx}(\cos \vartheta, \varphi) \cdot \rho(\vec{p}_1, \vec{p}_2), \quad (8.1)$$

where $\epsilon_{\mu 1}(\vec{p}_1)$ and $\epsilon_{\mu 2}(\vec{p}_2)$ stand for the single muon detection efficiencies as function of p_T and $|\eta|$. $\epsilon_{Vtx}(\cos \vartheta, \varphi)$ is the efficiency of the dimuon vertex module as a function of $\cos \vartheta$ and φ , and $\rho(\vec{p}_1, \vec{p}_2)$ is the so called ρ factor describing the muon pair correlations. Muons that are too close to each other in the phase space cannot be distinguished by the dimuon trigger and are thus seen as one single muon and not recorded. This effect becomes dominant at high p_T .

A special trigger was designed to measure dimuon correlations. It requires a single muon and a muon track. It is therefore de facto a single muon trigger and not affected by dimuon correlations. It was running for the first time during the end of data taking in 2012. Analyses using data taken before 2012 had to rely on MC simulations to be able to calculate the muon pair correlations. The ρ factor was defined as:

$$\rho = \frac{\epsilon_{\mu\mu}^{MCtruth}}{\epsilon_{\mu 1}^{totMC} \cdot \epsilon_{\mu 2}^{totMC}} \quad (8.2)$$

However, due to different detector and trigger effects between 2011 and 2012 run periods, this is not a completely valid comparison.

The data-driven ρ factor will be used to validate the ρ factor which will be calculated with 2012 MC simulations as outlined above.

8.1 Data-driven Determination of the ρ Factor

The calculation of the data-driven ρ factor is based on the *HLT_Mu15_TkMu5_Onia* (short Onia) trigger path that requires a muon with $p_T > 15$ GeV (Mu15 leg) and a tracker muon with $p_T > 5$ GeV (TkMu5 leg). This trigger, which selects events in a very broad mass window (2-12 GeV), is not affected by muon pair correlations and should therefore trigger on all events, even those that are not recorded by the *HLT_Dimuon8_Jpsi* (short Dimuon8) trigger path.

For the calculation of the ρ factor only events are taken into account which have at least fired the Onia trigger. Hence, every event triggered by the Dimuon8 trigger is also triggered by the Onia trigger, but not vice versa. Furthermore, it is assured that only events are selected, which have fired both legs of the Onia trigger just once. This allows the ρ factor to be expressed as the fraction

$$\rho = \frac{\text{events triggered by the Onia and the Dimuon8 trigger}}{\text{events triggered only by the Onia trigger}}, \quad (8.3)$$

ignoring the proper efficiency corrections for now. The Onia trigger provides an unbiased data sample for analysing Dimuon8 inefficiencies. Single muon cuts are applied to both muons:

$$\begin{aligned} |\eta| < 1.2 &\rightarrow p_T < 4.5 \text{ GeV} \\ 1.2 < |\eta| < 1.4 &\rightarrow p_T < 3.5 \text{ GeV} \\ 1.4 < |\eta| < 1.6 &\rightarrow p_T < 3.0 \text{ GeV} \end{aligned} \quad (8.4)$$

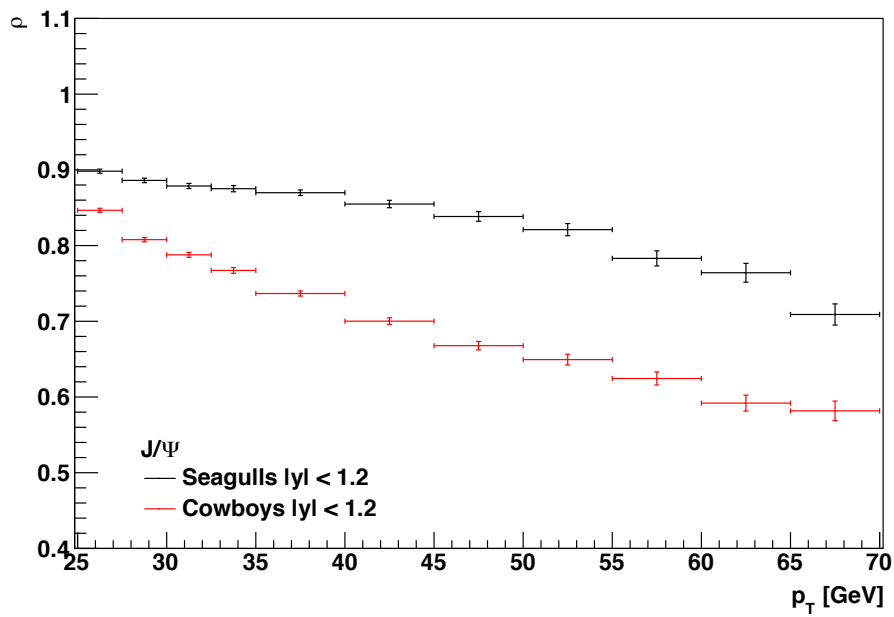
Additionally, the momentum of the lower p_T muon is required to be larger than 5 GeV and the momentum of the higher p_T muon to be larger than 15 GeV, respectively. The selected mass window is $2.9 \text{ GeV} < M_{Dimuon} < 3.25 \text{ GeV}$.

The following p_T and $|y|$ binning is used throughout all calculations:

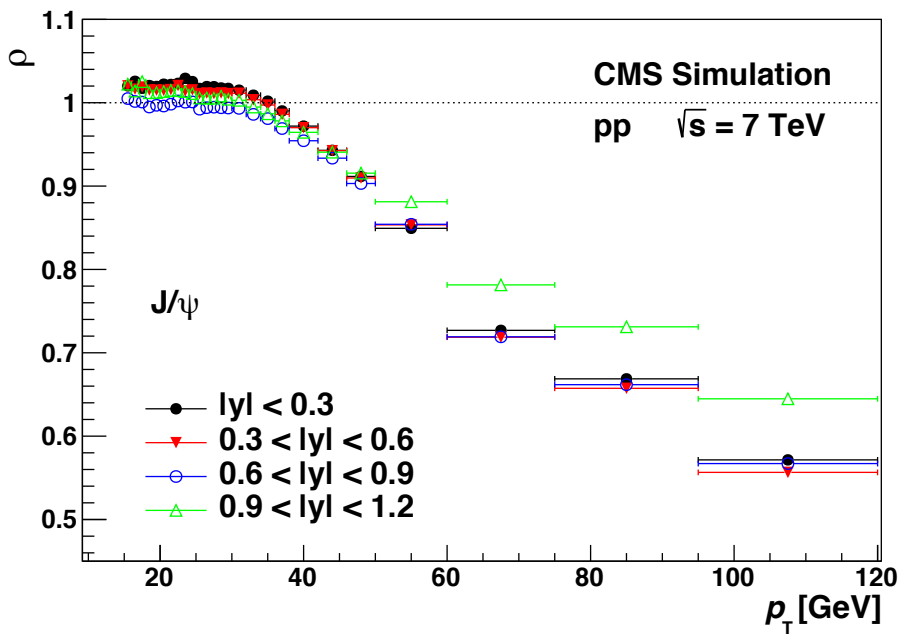
- dimuon p_T : 25., 27.5, 30., 32.5, 35., 40., 45., 50., 60., 70.
- dimuon $|y|$: 0., 0.2, 0.4, 0.6, 0.8, 1., 1.2,

Additionally, the calculations are performed integrated in $|y|$.

The ρ factor calculated without any efficiency corrections for seagull and cowboy dimuons only is shown in Fig. 8.1a. Reliable calculations can only be conducted for $p_T > 25 \text{ GeV}$ to stay away from trigger thresholds. The ρ factor for cowboy dimuons differs from the one for seagull dimuons in both shape and value. Since cowboy dimuons are closer in phase space, the stronger muon pair correlations are expected. The ρ factor calculated with 2011 MC simulations for seagulls only is shown in Fig. 8.1b. The muon pair correlations start at around 35 GeV yielding the ρ factor to drop from 1 at 35 GeV to around 0.6 at 100 GeV. The shape and relative difference between 30 and 70 GeV are similar to the data-driven ρ factor for seagull dimuons. Error calculations are conducted based on the Poissonian error of all events taken by the Onia trigger.



(a)



(b)

Figure 8.1: ρ factor calculated without any efficiency corrections for seagull and cowboy dimuons (a). 2011 MC ρ factor for seagull dimuons (b) [78].

Weighted ρ Factor

In order to get the correct ρ factor, the efficiency corrections have to be applied:

$$\rho_{\text{corrected}} = \rho \cdot \frac{1}{\underbrace{\frac{\epsilon_{\mu 15+D8}^{\mu 1} \cdot \epsilon_{Tk\mu 5+D8}^{\mu 2}}{\epsilon_{\mu 15}^{\mu 1} \cdot \epsilon_{Tk\mu 5}^{\mu 2}}}}_{C}} \cdot \frac{1}{\epsilon_{Vtx}(p_T, |y|)} \quad (8.5)$$

$$C = \frac{\epsilon_{\mu 15}^{\mu 1} \cdot \epsilon_{Tk\mu 5}^{\mu 2}}{\epsilon_{\mu 15+D8}^{\mu 1} \cdot \epsilon_{Tk\mu 5+D8}^{\mu 2}}, \quad (8.6)$$

where ρ stands for the ρ factor without efficiency corrections, C refers to the efficiency correction due to single muon efficiencies and $\epsilon_{Vtx}(p_T, |y|)$ stands for the dimuon vertex efficiency as function of dimuon p_T and dimuon rapidity. $\epsilon_{\mu 15+D8}^{\mu 1}$ is the efficiency of the first muon with a required match to the Mu15 leg of the Onia trigger and to the Dimuon8 trigger. $\epsilon_{Tk\mu 5+D8}^{\mu 2}$ is the efficiency of the second muon with a required match to the TkMu5 leg of the Onia trigger and to the Dimuon8 trigger. $\epsilon_{\mu 15}^{\mu 1}$ and $\epsilon_{Tk\mu 5}^{\mu 2}$ are the efficiencies of the two legs of the Onia trigger.

Using

$$\epsilon_{\mu 15+D8}^{\mu 1} = \epsilon_{\mu 15} \quad (8.7)$$

and

$$\epsilon_{Tk\mu 5+D8}^{\mu 2} = \epsilon_{Tk\mu 5}^{\mu 2} \cdot \epsilon_{D8|Tk\mu 5}^{\mu 2}, \quad (8.8)$$

the correction factor C can be written as

$$C = \frac{1}{\epsilon_{D8(2)|Tk\mu 5}^{\mu 2}}, \quad (8.9)$$

where $\epsilon_{D8|Tk\mu 5}^{\mu 2}$ is the *conditional efficiency* that a muon which has a match to the TkMu5 leg of the Onia trigger also has a match to the Dimuon8 trigger. It can be reduced to a TnP problem with the following conditions:

- The tag muon is a soft muon that fires the last filter of the muon part of the Onia trigger.
- The probe is a general track that also passes the last filter of the tracker muon leg of the Onia trigger.
- The passing probe additionally has to fire the Dimuon8 trigger.

The resulting efficiencies are shown in Fig. 8.3. They are very different for seagull and cowboy dimuons. The $|\eta|$ bin between 0.2 and 0.3 shows a very different behavior than the other bins due to the partly non-instrumentized regions of the muon barrel detectors. Therefore, events with muons inside this region are excluded. Up

to 8 GeV, the efficiency is nearly 100% throughout all $|\eta|$ bins, while for higher p_T the efficiency drops. This results from an unexpected excess in the number of triggered tracker muons at approximately 8 GeV – an effect that is not yet completely understood. The conditional efficiencies only correct the lower p_T muon and, thus, only have to cover the region up to 50 GeV.

In contrast to the Dimuon8 trigger, the Onia trigger has no cuts on the vertex probability. Therefore, the dimuon vertex efficiency correction has to be applied on all the events triggered by the Dimuon8 trigger (Sec. 7.8). Since the data-driven vertex efficiencies shows high statistical fluctuations, in particular at high p_T , the MC based efficiencies in connection with a data/MC scale factor are used. Figure 8.2 shows the total efficiency correction, i.e. the product of conditional efficiency and the dimuon vertex efficiency. The corrections are much stronger for cowboy dimuons. The efficiency corrections have to be regarded very carefully for high p_T regions, because the decreasing dimuon vertex efficiency affects the shape of the ρ factor quite heavily.

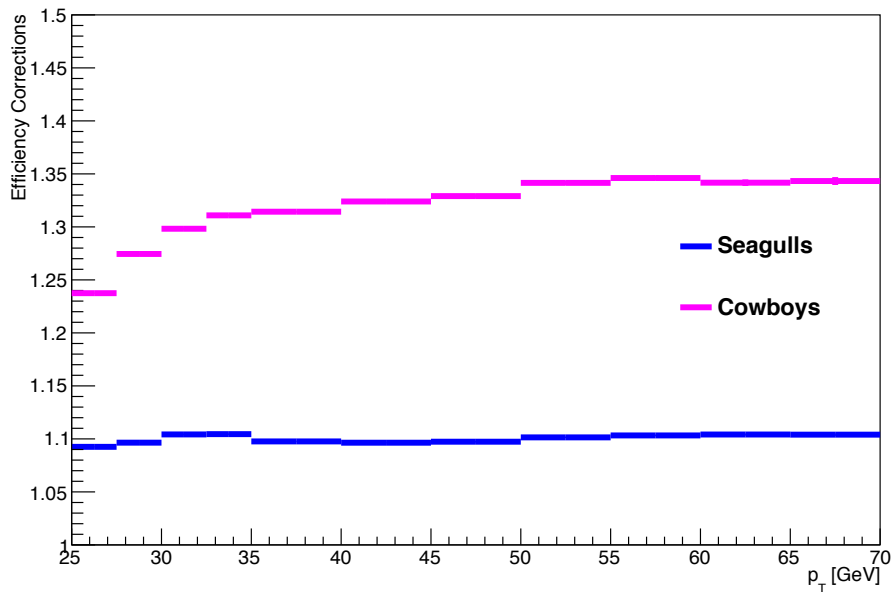


Figure 8.2: Total efficiency corrections for seagull and cowboy dimuons.

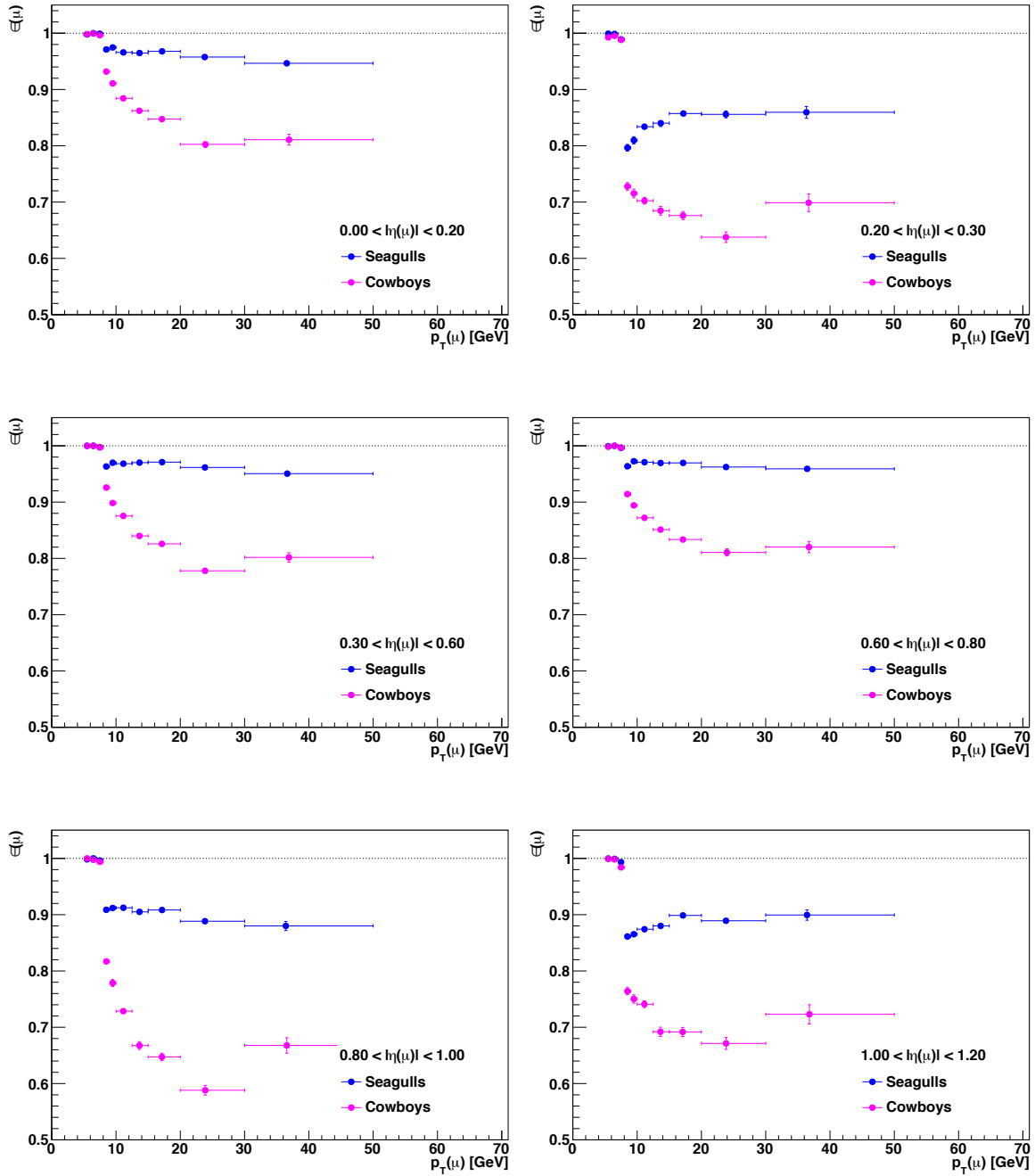


Figure 8.3: Data-driven $L1 \cdot L2 \cdot L3$ efficiency requiring that the muon passed the tracker muon leg of the onia trigger as a function of p_T for several $|\eta|$ bins for seagull and cowboy dimuons.

The error calculation is done using Poissonian statistics [79]. The estimator \hat{p} for the ρ factor that is not corrected for the efficiencies can be written as

$$\hat{p} = \frac{n}{d}, \quad (8.10)$$

where n stands for the unweighted numerator and d stands for the unweighted denominator. The variance for n is

$$Var[n] = \hat{p} \cdot (1 - \hat{p}) \cdot n \quad (8.11)$$

and the standard deviation for n is

$$\sigma(n) = \sqrt{\hat{p} \cdot (1 - \hat{p}) \cdot n} . \quad (8.12)$$

Hence, the resulting standard deviation for $\frac{n}{d_{weight}}$ is written as

$$\sigma\left(\frac{n}{d_{weight}}\right) = \frac{\sqrt{\hat{p} \cdot (1 - \hat{p}) \cdot n}}{d_{weight}}, \quad (8.13)$$

where d_{weight} stands for the denominator with the proper efficiency corrections. The error calculation breaks down for very few events in n . In this case, the estimator is set to its maximal value $\frac{1}{2}$. To have a very conservative error, the following standard deviation is used:

$$\sigma\left(\frac{n}{d_{weight}}\right) = \frac{\sqrt{\hat{p} \cdot (1 - \hat{p}) \cdot n}}{d_{weight}} = \frac{\sqrt{\frac{1}{2} \cdot (1 - \frac{1}{2}) \cdot n}}{d_{weight}} = \frac{\sqrt{n}}{d_{weight}} \cdot \frac{1}{2} \quad (8.14)$$

The ρ factor with the proper efficiency corrections is shown in Fig. 8.4 for seagull dimuons. The result is now very similar to the MC based ρ factor calculated in 2011. The ρ factor is close to unity below 35 GeV and then starts dropping to a value of around 0.8 at 70 GeV. Figure 8.5 shows the efficiency corrected ρ factor in four $|y|$ bins for easier comparison with the 2011 ρ factor. In contrast to 2011, the $0.9 < |y| < 1.2$ bin is much lower than the three other bins. This is closely related to the determination of the dimuon vertex efficiency. The better the determination of this efficiency, the more precisely the ρ factor can be calculated.

The efficiency corrected ρ factors for cowboy dimuons is shown in Figs. 8.6 and 8.7 integrated in $|y|$ and for four $|y|$ bins. The applied efficiency correction is much stronger for cowboys. Therefore, the ρ factor is now similar to the one for seagulls in contrast to what was seen for the ρ factor without any efficiency corrections.

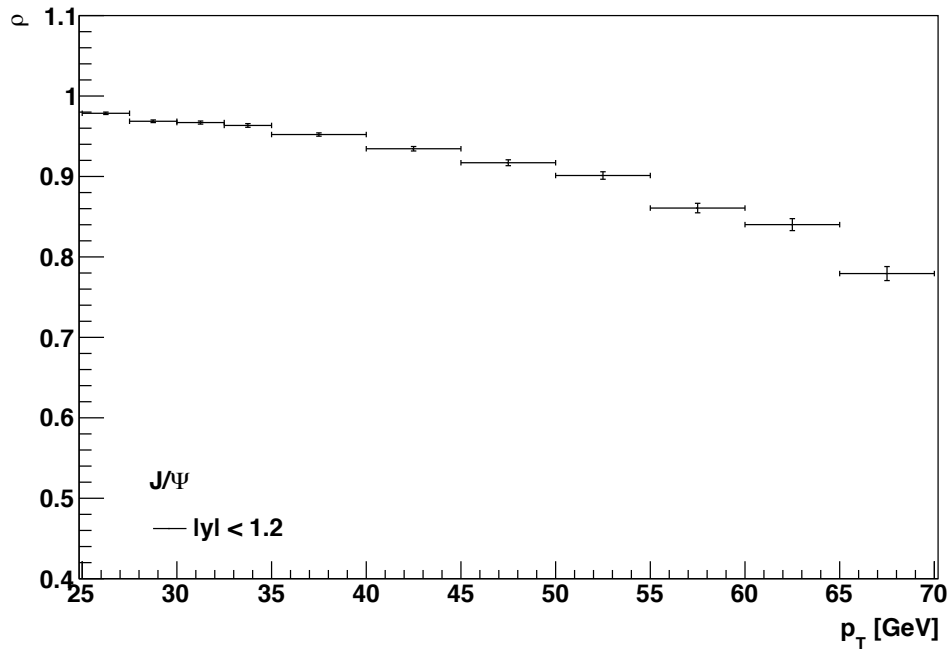


Figure 8.4: Efficiency corrected ρ factor for seagull dimuons as a function of dimuon p_T and integrated $|y|$.

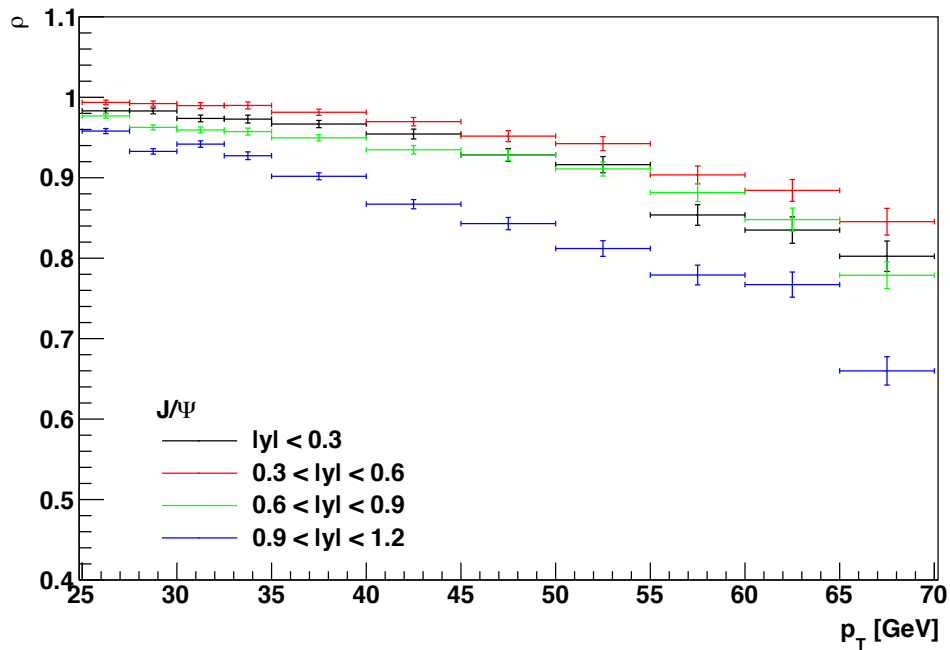


Figure 8.5: Efficiency corrected ρ factors for seagull dimuons as a function of p_T for several bins in $|y|$.

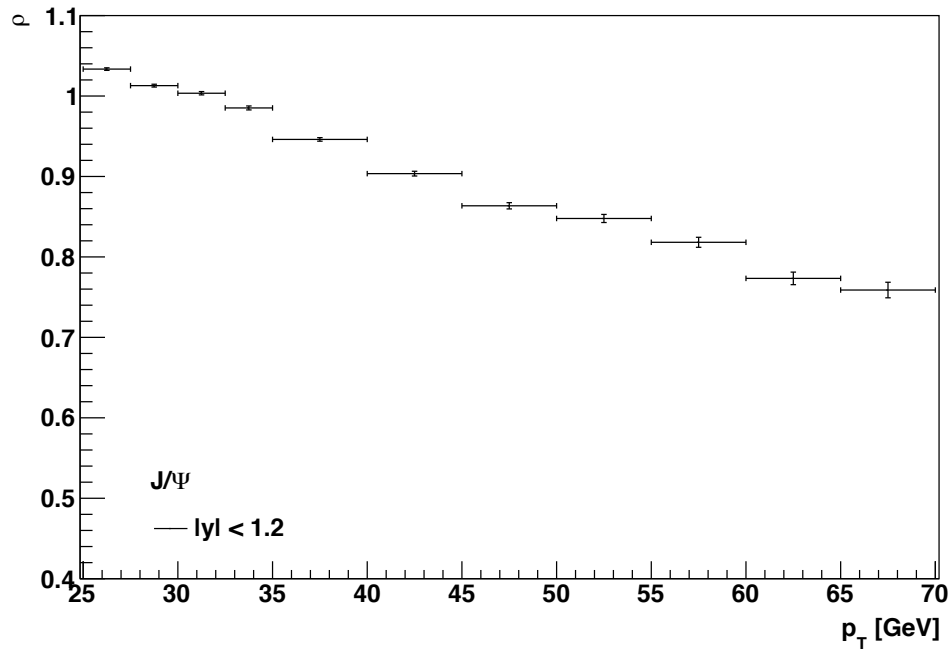


Figure 8.6: Efficiency corrected ρ factor for cowboy dimuons as a function of dimuon p_T and integrated $|y|$.

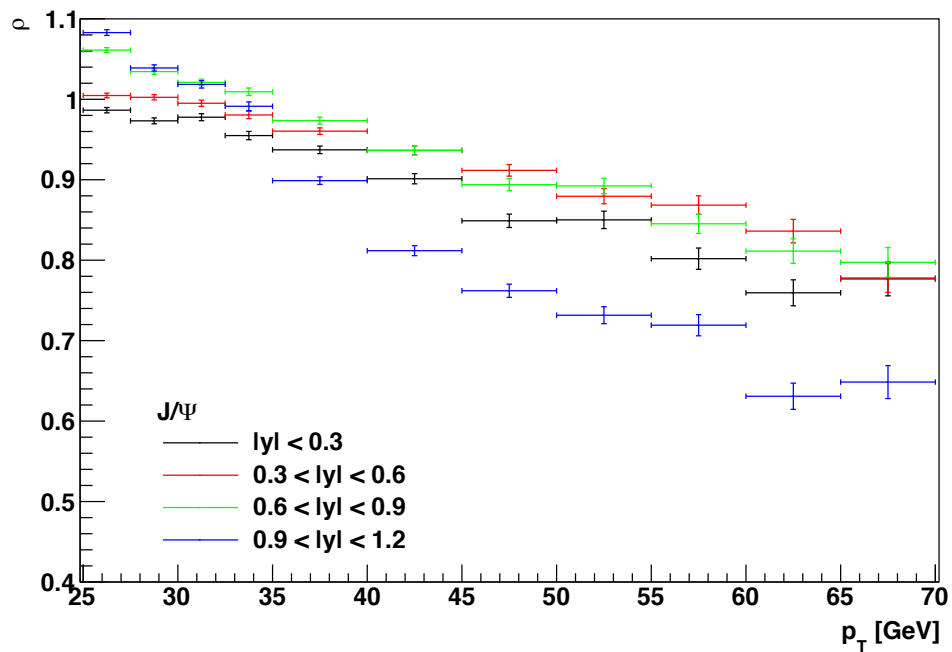


Figure 8.7: Efficiency corrected ρ factors for cowboy dimuons as a function of p_T for several bins in $|y|$.

9 Pseudo-Data Tests

Pseudo-data tests are used on the one hand to check if there is any possible bias coming from the analysis framework. On the other hand, they are used to test the influence of input parameters like the efficiencies. In this context a pseudo-data set is a sample of events generated following the distribution of a certain PDF, parametrized by the parameters P_i ('injected parameters') and characterized by N_{Dim} dimensions, containing a certain number of events N_{Events} . The basic idea of a pseudo-data test is to generate N_{Toy} pseudo-data sets with N_{Events} , use them as input for the fitting framework to be tested, and compare the N_{Toy} sets of estimated parameters ('extracted parameters') with the injected parameters. The generated N_{Toy} pseudo-data sets are supposed to approximate conditions as found in the actual experiment. A significant deviation between the injected and extracted parameters reflects a possible bias. As outlined in Chap.7 the influence of

- seagull and cowboy dimuon efficiencies and the
- pileup dependent L3 efficiency

is discussed in this chapter.

The *standard score* $z(P_i)$ and the respective *error estimates* $\hat{\sigma}_{P_i}$ can be calculated for each parameter P_i individually:

$$z(P_i) = \frac{\hat{P}_i - P_i^{orig}}{\hat{\sigma}_{P_i}} \quad (9.1)$$

In this formula P_i^{orig} refers to the known injected parameters and \hat{P}_i to the maximum likelihood estimates of the N_n parameters P_i . The *pull distribution*, describing the statistical properties of the standard score, indicates whether any bias arises from the fit. The distribution of all standard scores can be fitted individually by a Gaussian function for all parameters in all bins. The expected value of the standard core variable $z(P_i)$ equals 0 and the standard deviation equals 1. Thus, for $N_{Toy} \rightarrow \infty$ and $N_{Events} \rightarrow \infty$ the standard score distribution should approach a Gaussian function with $\mu_z = 0$ and $\sigma_z = 1$ given that no bias exists.

The Gaussian fit itself returns values for μ_z and σ_z ; its accuracy mostly depends on N_{Toy} and N_{Events} . If μ_z deviates significantly from 0, either the returned parameter estimate is biased or the error estimate is wrong. A significant deviation of σ_z from 1 yields unreliable error estimates. While σ_z being significantly larger

than 1 reflects underestimated errors, σ being significantly smaller than 1 reflects overestimated errors [71].

Figure 9.1 shows an example of a pseudo-data test for the variable is λ_ϕ in the PX frame. $N_{Toy} = 50$ pseudo-data sets of $N_{Events} = 50000$ events are generated, reconstructed and fed into the fitting framework. 50 values for λ_ϕ are obtained, one for each pseudo-data set. The distribution of the λ_ϕ parameter generated in 50 pseudo-data sets is shown in Fig. 9.1(a). The expected mean is depicted by the red line. The pull distribution of λ_ϕ is shown in Fig. 9.1(b).

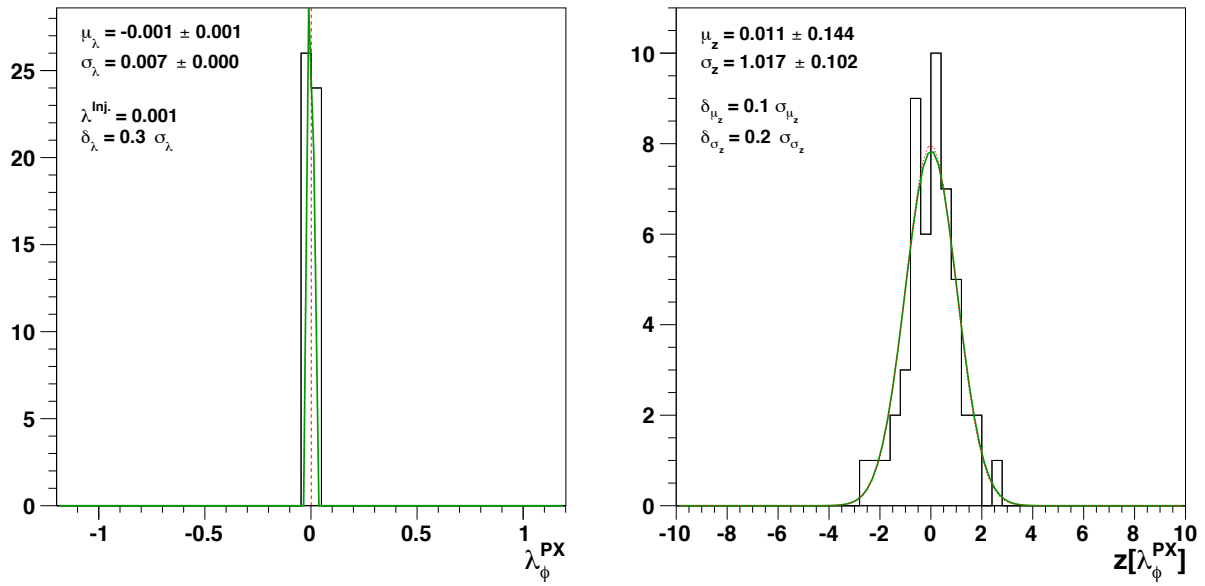


Figure 9.1: Distribution of λ_ϕ (a) and pull distribution (b) in the bin $|y| < 1.2$, $15 < p_T < 30$ GeV for 50 generated pseudo-data sets. Parameter distribution: Solid green line corresponds to an imposed Gaussian fit of the results and dotted red line to the injected parameter. Pull distribution: Solid green line corresponds to an imposed Gaussian fit of the results and dotted red line to the expected parameter distribution.

9.1 Seagull and Cowboy Dimuon Efficiencies

As outlined in Chap. 7 seagull and cowboy dimuon efficiencies differ slightly at $L1 \cdot L2 \cdot L3$. The question is, how much do these deviations influence the outcome of the polarization analysis? To test the influence of the different efficiencies for seagull and cowboy dimuons a pseudo-data test is conducted. MC based efficiencies are taken for consistency. The following tests use:

- $N_{Toy} = 50$ pseudo data-sets
- $N_{Events} = 50000$ generated events per data-set
- unpolarized signals
- no background fraction

Moreover, the same single muon cuts as for calculating the dimuon vertex efficiency and the ρ factor, respectively, are used (Sec. 7.8).

N_{Toy} pseudo-data sets are generated and reconstructed using the total single muon efficiencies calculated for either seagull or cowboy dimuons. Afterwards those pseudo-data sets are used as input for the fitting framework to be tested, which uses total single muon efficiencies calculated for all dimuon pairs to correct for the inefficiencies. The deviation of the different parameters reflects a possible bias triggered by the fact that a cowboy (seagull) dimuon is fitted with efficiencies calculated for all dimuon pairs. This is a *worst-case* scenario, because not every reconstructed dimuon event is a cowboy (seagull) dimuon. This study should rather help to determine the upper limit of biases (on cowboy and seagull dimuons) emerging from the use of combined total single muon efficiencies.

To check whether the pseudo-data test itself introduces a bias, the tests are conducted using the same efficiencies for the generation, reconstruction and fitting of the events (total single muon efficiencies of all dimuons). This is a crucial check of the analysis framework. Even in a *best case* scenario a small systematic uncertainty remains. Thus, in order to check whether biases of pseudo-data tests of seagull and cowboy dimuon inefficiencies are not simply due to systematic uncertainties, pseudo-data tests are conducted with the same input efficiencies for reconstruction and fitting (factorized single muon efficiencies of all dimuons). In Fig. 9.2 pseudo-data test results (of the framework uncertainty test) of the frame invariant parameter $\tilde{\lambda}$ are shown reflecting a small bias for $10 < p_T < 15$ GeV in the CS frame. Compared to the biases of seagull and cowboy pseudo-data tests (see below) the deviations in the remaining bins are negligibly small.

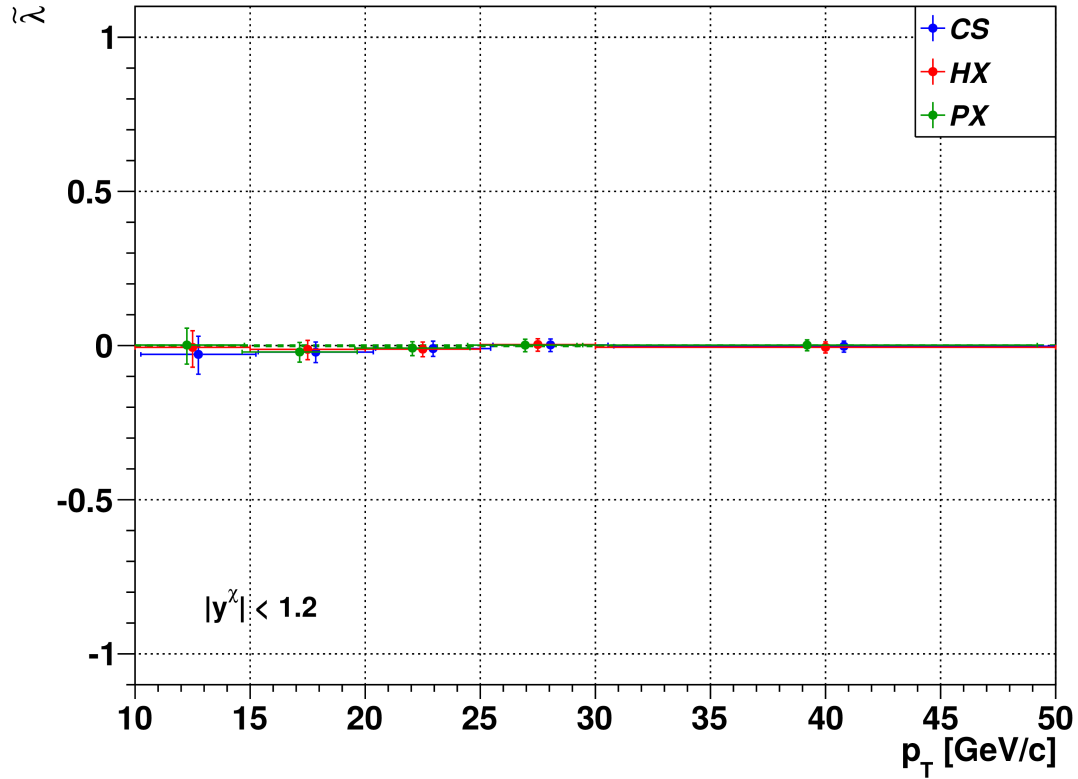


Figure 9.2: Absolute bias of the $\tilde{\lambda}$ parameter introduced by the testing framework (in the CS, HX and PX frames). The error bars correspond to the first moment of the parameter distribution. The dashed green line is the injected value.

Figure 9.3 shows the absolute bias introduced due to the usage of efficiencies calculated for all dimuon pairs to correct pseudo-data sets which are reconstructed with the single muon efficiencies calculated for cowboy dimuons. There is a small bias in mid p_T regions ($15 < p_T < 20$ GeV, $20 < p_T < 25$ GeV) for the polarization parameters λ_{ϑ}^{PX} , λ_{φ}^{PX} , $\lambda_{\vartheta\varphi}^{PX}$ and $\tilde{\lambda}^{PX}$ in the PX frame. Tables 9.1 and 9.2 summarize the means of the distributions of the standard scores and the root mean squares (r.m.s) of the distribution of the standard scores, respectively. The results for the frame invariant parameter $\tilde{\lambda}$ in the PX, HX and CS frame can be found in Appendix B showing a good consistency between the three different reference frames.

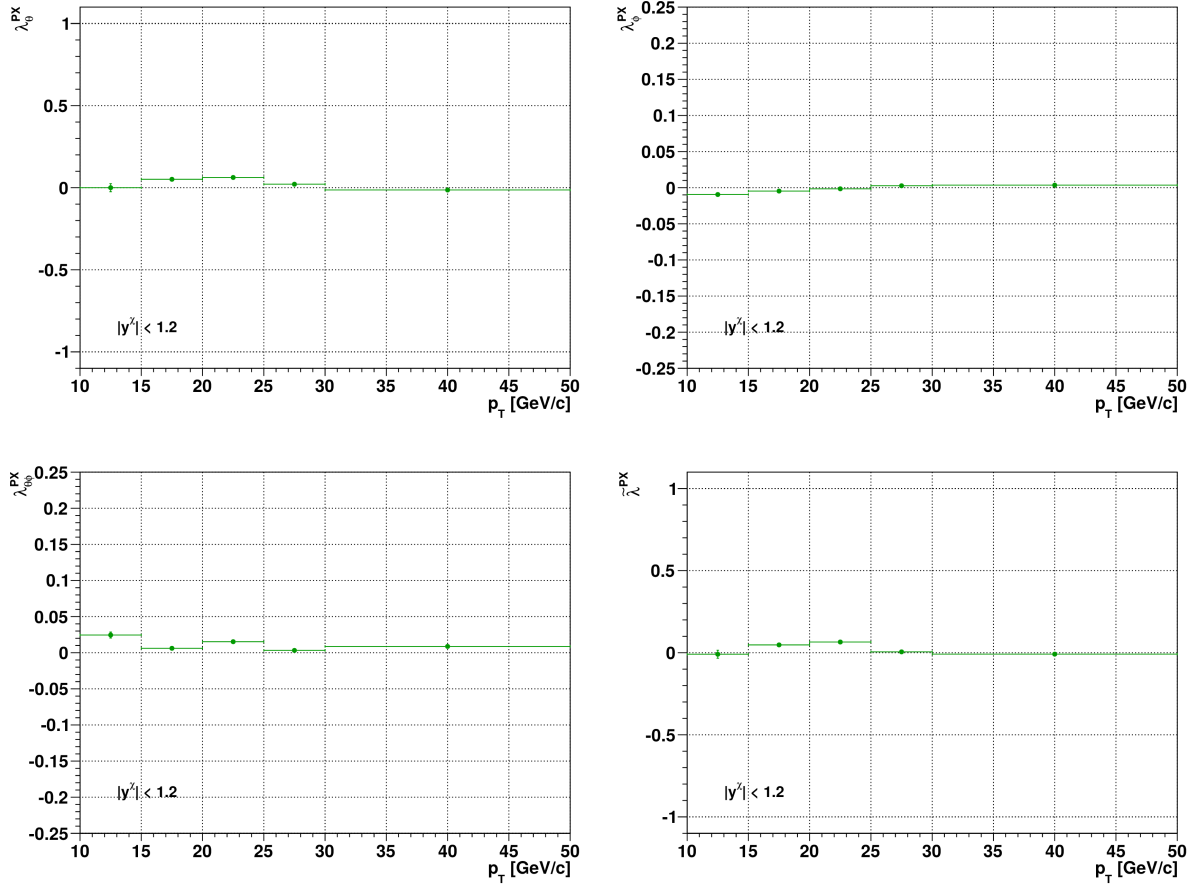


Figure 9.3: The absolute bias of the polarization parameters in the PX frame for the pseudo-data test of the total single muon efficiencies of cowboy dimuons. p_T dependence of the mean of the distribution of the parameter estimates of λ_ϕ^{PX} (top left), λ_φ^{PX} (top right), $\lambda_{\phi\phi}^{PX}$ (bottom left) and $\tilde{\lambda}^{PX}$ (bottom right) in the rapidity region $0 < |y| < 1.2$. The error bars correspond to the first moment of the parameter distribution. The injected value is 0 for all parameters.

p_T [GeV]	$\mu_{z(\lambda_\theta)}$	$\mu_{z(\lambda_\varphi)}$	$\mu_{z(\lambda_{\theta\varphi})}$	$\mu_{z(\tilde{\lambda})}$
CS frame, $0.0 < y < 1.2$				
10–15	0.041 ± 0.191	-0.143 ± 0.185	-0.918 ± 0.180	-0.411 ± 0.188
15–20	-0.420 ± 0.193	0.400 ± 0.201	-0.426 ± 0.198	0.244 ± 0.197
20–25	-1.113 ± 0.184	1.275 ± 0.184	-0.468 ± 0.148	1.021 ± 0.168
25–30	-0.496 ± 0.145	0.534 ± 0.184	-0.253 ± 0.183	0.313 ± 0.173
30–50	0.189 ± 0.208	-0.128 ± 0.152	-0.224 ± 0.169	-0.095 ± 0.180
HX frame, $0.0 < y < 1.2$				
10–15	0.274 ± 0.175	-0.797 ± 0.208	0.949 ± 0.159	0.136 ± 0.173
15–20	0.536 ± 0.203	-0.121 ± 0.170	0.231 ± 0.178	0.453 ± 0.201
20–25	1.255 ± 0.167	0.017 ± 0.148	0.125 ± 0.151	1.137 ± 0.169
25–30	0.608 ± 0.173	-0.061 ± 0.141	0.171 ± 0.184	0.474 ± 0.181
30–50	-0.329 ± 0.171	0.101 ± 0.235	0.273 ± 0.175	-0.108 ± 0.186
PX frame, $0.0 < y < 1.2$				
10–15	0.017 ± 0.186	-0.420 ± 0.184	1.021 ± 0.181	-0.052 ± 0.183
15–20	0.449 ± 0.201	-0.080 ± 0.166	0.433 ± 0.201	0.395 ± 0.199
20–25	1.369 ± 0.199	0.087 ± 0.150	0.462 ± 0.147	1.189 ± 0.167
25–30	0.587 ± 0.204	-0.053 ± 0.138	0.248 ± 0.187	0.427 ± 0.191
30–50	-0.208 ± 0.177	0.083 ± 0.240	0.231 ± 0.169	-0.083 ± 0.193

Table 9.1: Mean of the distribution of the standard score $z(\lambda_i)$: $\mu_{z(\lambda_i)} \pm \sigma_{\mu_{z(\lambda_i)}}$ for the unpolarized pseudo-data test where the pseudo-data sets are reconstructed with the single muon efficiencies calculated for cowboy dimuons.

p_T [GeV]	$\sigma_{z(\lambda_\theta)}$	$\sigma_{z(\lambda_\varphi)}$	$\sigma_{z(\lambda_{\theta\varphi})}$	$\sigma_{z(\tilde{\lambda})}$
CS frame, $0.0 < y < 1.2$				
10–15	1.325 ± 0.135	1.280 ± 0.131	1.250 ± 0.128	1.302 ± 0.133
15–20	1.334 ± 0.136	1.393 ± 0.142	1.368 ± 0.140	1.367 ± 0.140
20–25	1.277 ± 0.130	1.275 ± 0.130	1.027 ± 0.105	1.165 ± 0.119
25–30	1.025 ± 0.102	1.303 ± 0.130	1.294 ± 0.129	1.226 ± 0.123
30–50	1.440 ± 0.147	1.056 ± 0.108	1.170 ± 0.119	1.248 ± 0.127
HX frame, $0.0 < y < 1.2$				
10–15	1.211 ± 0.124	1.439 ± 0.147	1.101 ± 0.112	1.198 ± 0.122
15–20	1.406 ± 0.144	1.181 ± 0.121	1.233 ± 0.126	1.392 ± 0.142
20–25	1.157 ± 0.118	1.026 ± 0.105	1.047 ± 0.107	1.168 ± 0.119
25–30	1.226 ± 0.123	0.997 ± 0.100	1.299 ± 0.130	1.283 ± 0.128
30–50	1.183 ± 0.121	1.625 ± 0.166	1.214 ± 0.124	1.286 ± 0.131
PX frame, $0.0 < y < 1.2$				
10–15	1.290 ± 0.132	1.276 ± 0.130	1.256 ± 0.128	1.271 ± 0.130
15–20	1.396 ± 0.142	1.152 ± 0.118	1.395 ± 0.142	1.382 ± 0.141
20–25	1.380 ± 0.141	1.039 ± 0.106	1.021 ± 0.104	1.155 ± 0.118
25–30	1.445 ± 0.144	0.974 ± 0.097	1.321 ± 0.132	1.349 ± 0.135
30–50	1.224 ± 0.125	1.663 ± 0.170	1.171 ± 0.120	1.338 ± 0.137

Table 9.2: R.m.s. of the distribution of the standard score $z(\lambda_i)$: $\sigma_{z(\lambda_i)} \pm \sigma_{\sigma_{z(\lambda_i)}}$ for the unpolarized pseudo-data test where the pseudo-data sets are reconstructed with the single muon efficiencies calculated for cowboy dimuons.

Figure 9.4 shows the absolute bias introduced due to the usage of efficiencies calculated for all dimuon pairs to correct pseudo-data sets which are reconstructed with the single muon efficiencies calculated for seagull dimuons. There is again a small bias in mid p_T regions ($15 < p_T < 20$ GeV, $20 < p_T < 25$ GeV) for the polarization parameters λ_θ^{PX} , λ_φ^{PX} , $\lambda_{\theta\varphi}^{PX}$ and $\tilde{\lambda}^{PX}$ in the PX frame, which has opposite sign than the bias seen for cowboy dimuons. Tables 9.3 and 9.4 summarize the means of the distributions of the standard scores and the r.m.s of the distribution of the standard scores. The results for the frame invariant parameter $\tilde{\lambda}$ in the PX, HX and CS frame can be found in Appendix B showing again a good consistency between the three different reference frames.

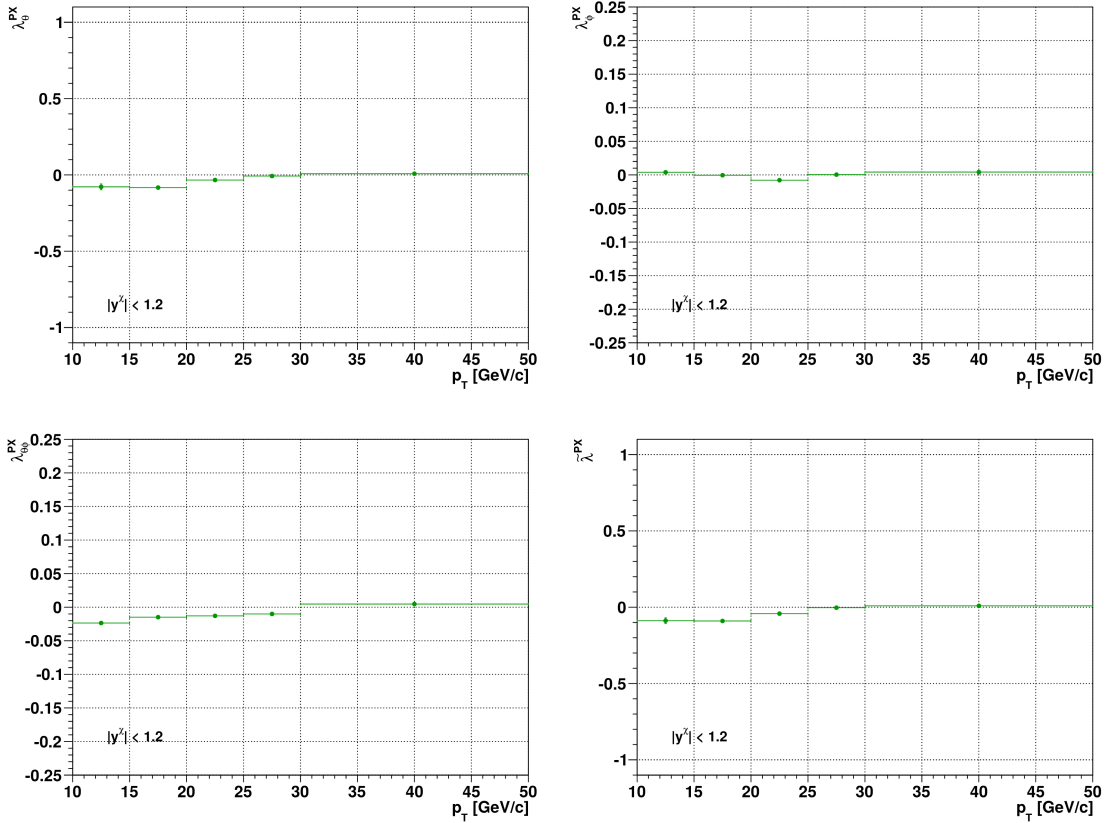


Figure 9.4: The absolute bias of the polarization parameters in the PX frame for the pseudo-data test of the total single muon efficiencies of seagull dimuons. p_T dependence of the mean of the of the distribution of the parameter estimates of λ_θ^{PX} (top left), λ_φ^{PX} (top right), $\lambda_{\theta\varphi}^{PX}$ (bottom left) and $\tilde{\lambda}^{PX}$ (bottom right) in the rapidity region $0 < |y| < 1.2$. The error bars correspond to the first moment of the parameter distribution. The injected value is 0 for all parameters.

p_T [GeV]	$\mu_{z(\lambda_\theta)}$	$\mu_{z(\lambda_\varphi)}$	$\mu_{z(\lambda_{\theta\varphi})}$	$\mu_{z(\tilde{\lambda})}$
CS frame, $0.0 < y < 1.2$				
10–15	0.854 ± 0.141	-0.871 ± 0.135	1.217 ± 0.126	-1.120 ± 0.160
15–20	1.273 ± 0.135	-1.293 ± 0.129	0.634 ± 0.172	-1.326 ± 0.135
20–25	0.741 ± 0.152	-0.870 ± 0.161	0.541 ± 0.128	-0.874 ± 0.165
25–30	0.322 ± 0.143	-0.277 ± 0.156	0.431 ± 0.153	-0.243 ± 0.154
30–50	-0.184 ± 0.152	0.148 ± 0.119	0.193 ± 0.163	0.039 ± 0.128
HX frame, $0.0 < y < 1.2$				
10–15	-1.069 ± 0.163	0.390 ± 0.142	-0.458 ± 0.161	-0.981 ± 0.157
15–20	-1.384 ± 0.146	0.113 ± 0.157	-0.037 ± 0.177	-1.266 ± 0.142
20–25	-0.872 ± 0.187	0.029 ± 0.161	-0.285 ± 0.125	-0.756 ± 0.175
25–30	-0.260 ± 0.156	0.082 ± 0.145	-0.395 ± 0.155	-0.201 ± 0.155
30–50	0.300 ± 0.148	-0.114 ± 0.168	-0.179 ± 0.167	0.117 ± 0.134
PX frame, $0.0 < y < 1.2$				
10–15	-0.800 ± 0.160	0.011 ± 0.144	-1.229 ± 0.136	-0.794 ± 0.155
15–20	-1.285 ± 0.141	-0.040 ± 0.155	-0.651 ± 0.172	-1.228 ± 0.138
20–25	-0.830 ± 0.166	-0.045 ± 0.156	-0.534 ± 0.128	-0.770 ± 0.169
25–30	-0.329 ± 0.180	0.067 ± 0.144	-0.452 ± 0.151	-0.233 ± 0.162
30–50	0.294 ± 0.144	-0.105 ± 0.168	-0.196 ± 0.166	0.137 ± 0.137

Table 9.3: Means of the distribution of the standard score $z(\lambda_i)$: $\mu_{z(\lambda_i)} \pm \sigma_{\mu_{z(\lambda_i)}}$ for the unpolarized pseudo-data test where the pseudo-data sets are reconstructed with the single muon efficiencies calculated for seagull dimuons.

p_T [GeV]	$\sigma_{z(\lambda_\theta)}$	$\sigma_{z(\lambda_\varphi)}$	$\sigma_{z(\lambda_{\theta\varphi})}$	$\sigma_{z(\tilde{\lambda})}$
CS frame, $0.0 < y < 1.2$				
10–15	0.995 ± 0.099	0.954 ± 0.095	0.894 ± 0.089	1.132 ± 0.113
15–20	0.958 ± 0.096	0.916 ± 0.092	1.214 ± 0.121	0.956 ± 0.096
20–25	1.072 ± 0.107	1.140 ± 0.114	0.905 ± 0.091	1.168 ± 0.117
25–30	1.014 ± 0.101	1.102 ± 0.110	1.084 ± 0.108	1.090 ± 0.109
30–50	1.073 ± 0.107	0.844 ± 0.084	1.150 ± 0.115	0.903 ± 0.090
HX frame, $0.0 < y < 1.2$				
10–15	1.155 ± 0.115	1.005 ± 0.100	1.141 ± 0.114	1.108 ± 0.111
15–20	1.034 ± 0.103	1.114 ± 0.111	1.251 ± 0.125	1.006 ± 0.101
20–25	1.322 ± 0.132	1.135 ± 0.114	0.882 ± 0.088	1.238 ± 0.124
25–30	1.105 ± 0.110	1.025 ± 0.103	1.099 ± 0.110	1.093 ± 0.109
30–50	1.049 ± 0.105	1.191 ± 0.119	1.178 ± 0.118	0.951 ± 0.095
PX frame, $0.0 < y < 1.2$				
10–15	1.133 ± 0.113	1.017 ± 0.102	0.963 ± 0.096	1.093 ± 0.109
15–20	0.994 ± 0.099	1.094 ± 0.109	1.219 ± 0.122	0.978 ± 0.098
20–25	1.175 ± 0.118	1.107 ± 0.111	0.903 ± 0.090	1.192 ± 0.119
25–30	1.269 ± 0.127	1.021 ± 0.102	1.069 ± 0.107	1.149 ± 0.115
30–50	1.019 ± 0.102	1.184 ± 0.118	1.176 ± 0.118	0.966 ± 0.097

Table 9.4: R.m.s. of the distribution of the standard score $z(\lambda_i)$: $\sigma_{z(\lambda_i)} \pm \sigma_{\sigma_{z(\lambda_i)}}$ for the unpolarized pseudo-data test where the pseudo-data sets are reconstructed with the single muon efficiencies calculated for seagull dimuons.

9.2 Pileup Dependent L3 Efficiencies

Pileup studies discussed in Sec. 7.7.2 reveal a vertex dependence for L3 efficiencies. Thus, the MC sample is split into three different regions of pileup as shown in Fig. 9.5:

- low pileup: 0-9 vertices,
- average pileup: 10 - 17 vertices
- high pileup: 18 - 35 vertices

The L3 efficiencies for all dimuons are calculated for low and high pileup regions. They are shown in comparison to the pileup integrated L3 efficiencies for data and MC in Figs. 9.6 and 9.7. Deviations from the pileup integrated efficiencies are seen in particular at low p_T (up to 5 GeV) in the barrel and in all p_T region in the forward region, starting at $|\eta| > 0.8$. The pileup dependence is more pronounced for MC based efficiencies.

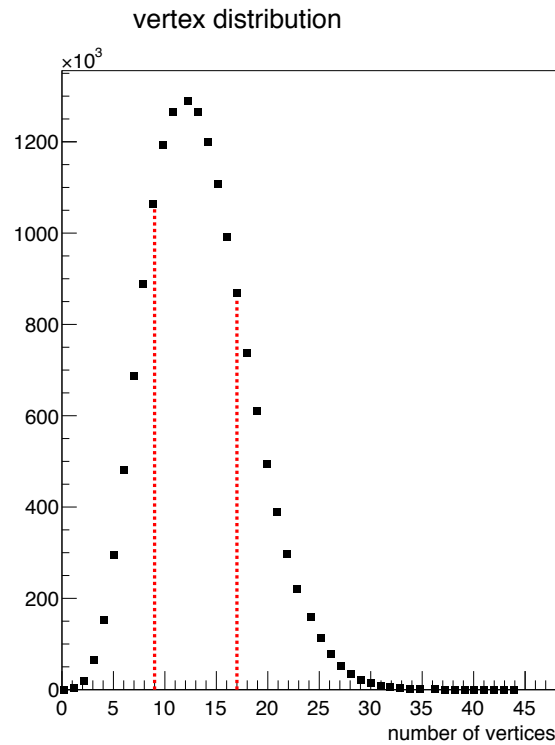


Figure 9.5: Distribution of the number of vertices in MC. The dashed red lines indicate three different pileup regions.

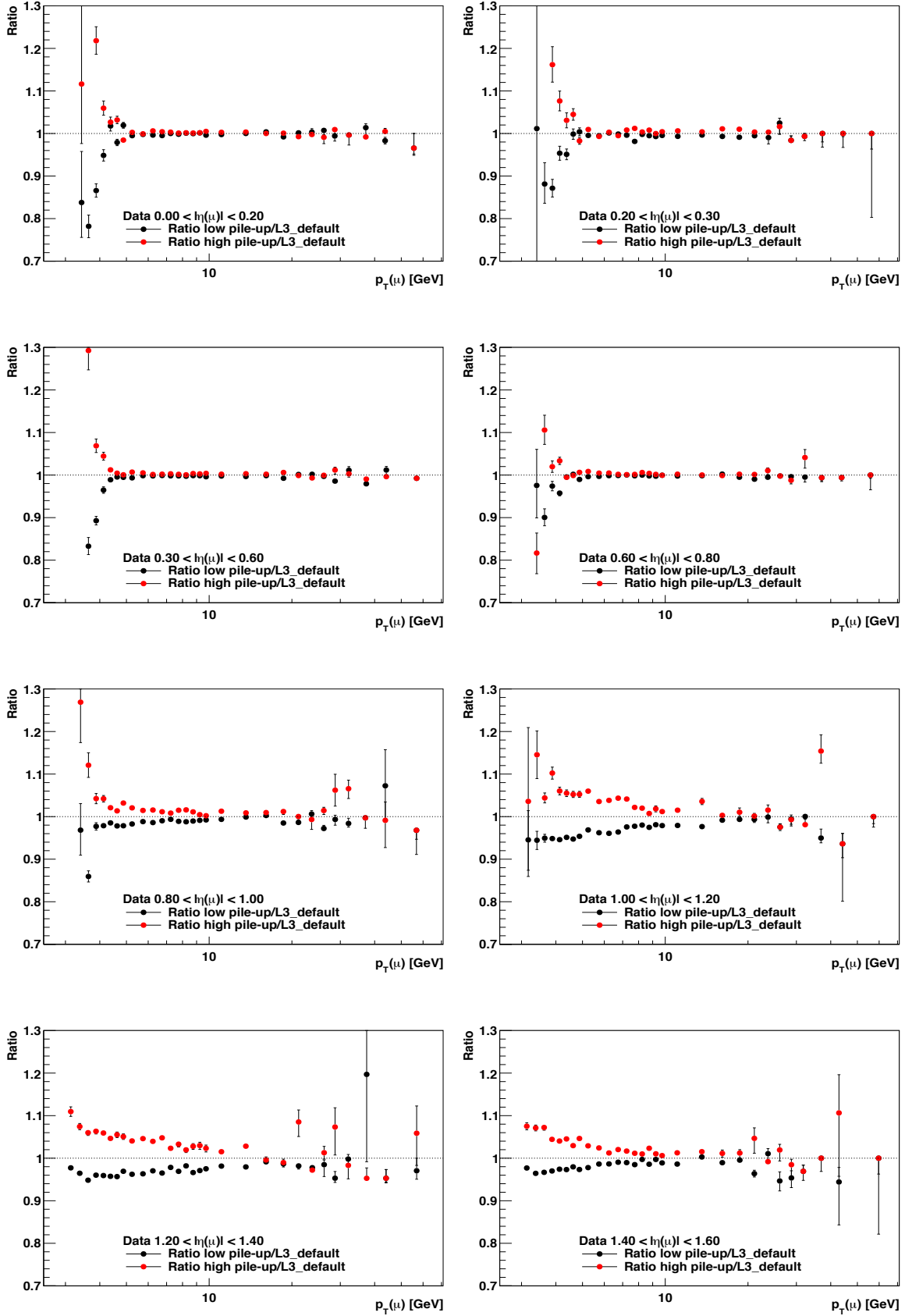


Figure 9.6: Data-driven L3 efficiencies calculated for low and high pileup events as a function of p_T for several $|\eta|$ bins. The error bars correspond to the first moment of the respective fraction.

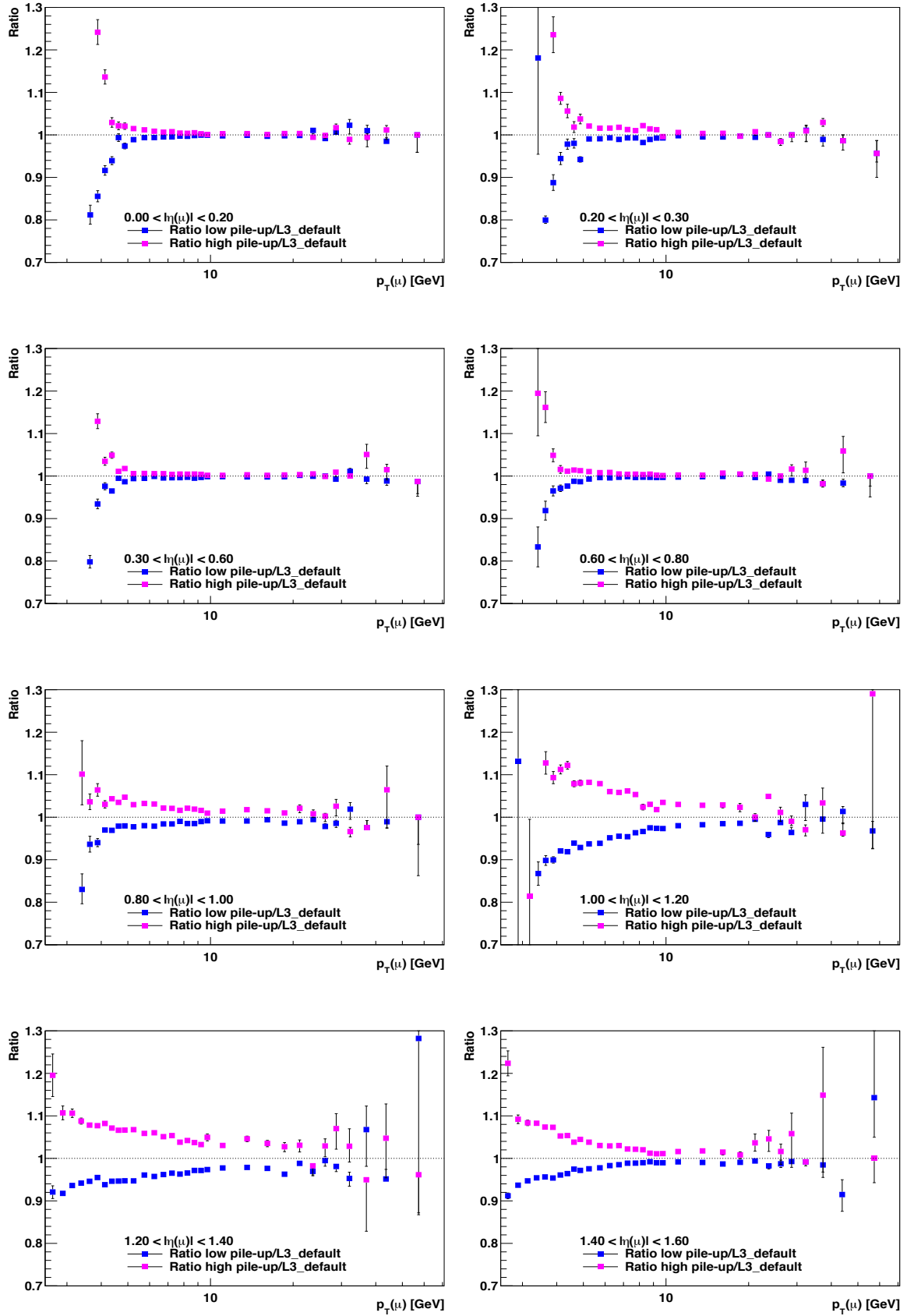


Figure 9.7: MC-driven L3 efficiencies calculated for low and high pileup events as a function of p_T for several $|\eta|$ bins. The error bars correspond to the first moment of the respective fraction.

Pileup dependent L3 efficiencies are used to generate and reconstruct $N_{Toy} = 50$ pseudo-data sets, while the pileup integrated L3 efficiencies are used to extract the parameters. Figure 9.8 shows the absolute bias of the polarization parameters in the PX frame introduced due to the usage of pileup integrated efficiencies when all the events are generated and reconstructed with low pileup efficiencies. The introduced bias is small in all p_T bins. Figure 9.9 shows the absolute bias of the polarization parameters in the PX frame introduced due to the usage of pileup integrated efficiencies when all the events are generated and reconstructed with high pileup efficiencies. The introduced bias is small and opposite sign to the bias introduced due to the low pileup efficiencies. The results for the $\tilde{\lambda}$ parameter obtained in these studies can be found in Appendix B.

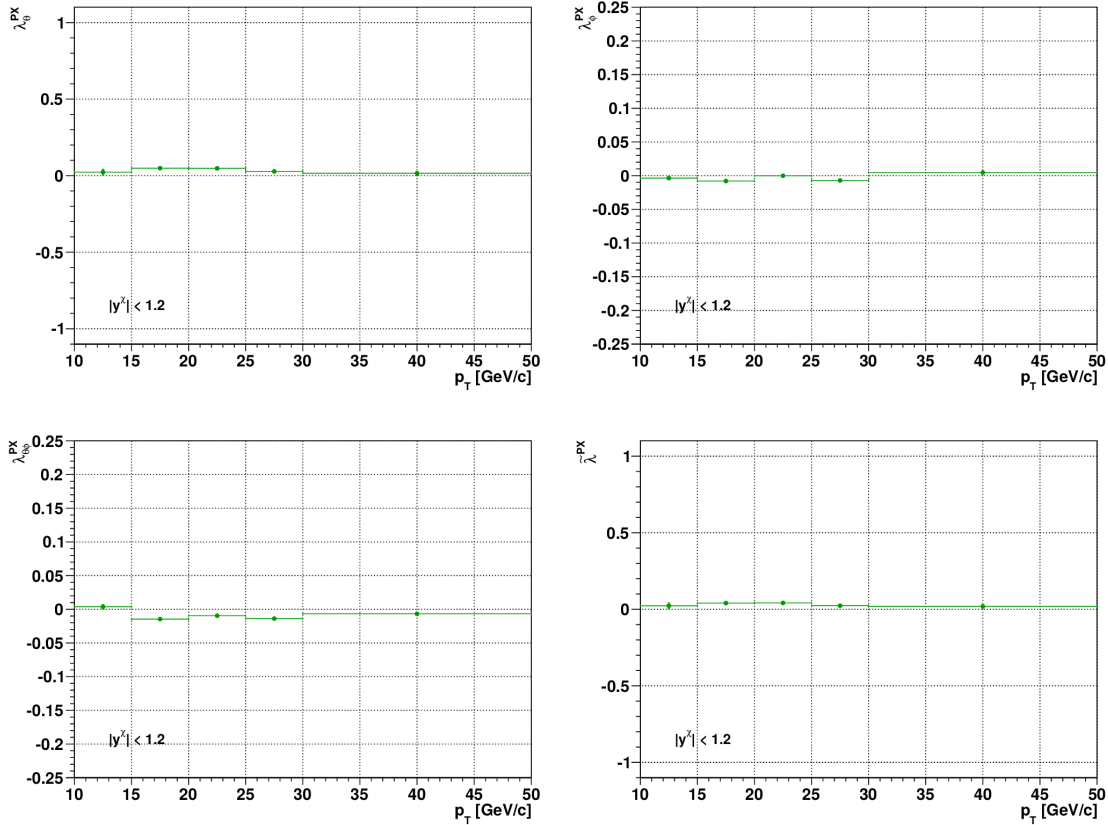


Figure 9.8: The absolute bias of the polarization parameters in the PX frame for the pseudo-data test of the total single muon efficiencies of low pileup L3 efficiencies. p_T dependence of the mean of the distribution of the parameter estimates of λ_{φ}^{PX} (top left), λ_{φ}^{PX} (top right), λ_{φ}^{PX} (bottom left) and $\tilde{\lambda}^{PX}$ (bottom right) in the rapidity region $0 < |y| < 1.2$. The error bars correspond to the first moment of the parameter distribution. The injected value is 0 for all parameters.

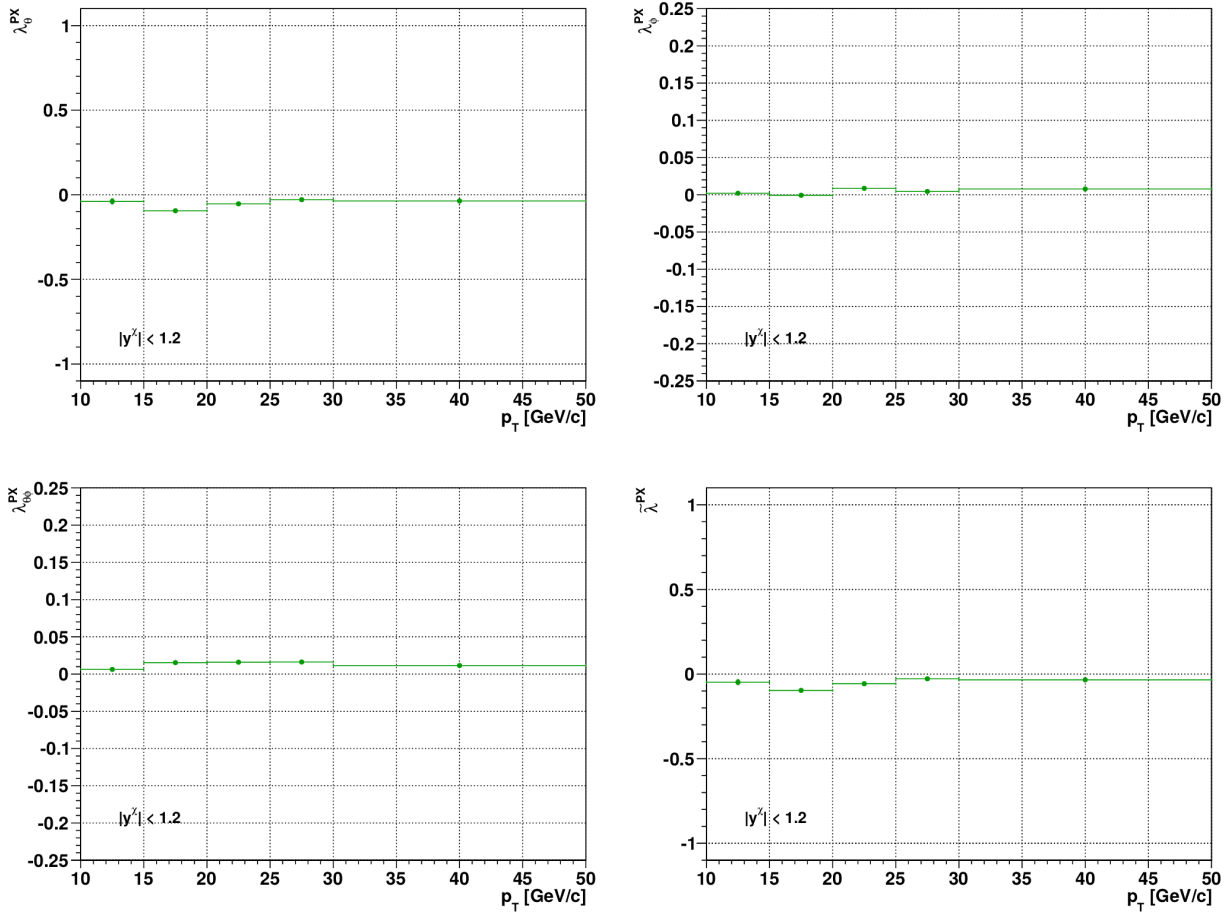


Figure 9.9: The absolute bias of the polarization parameters in the PX frame for the pseudo-data test of the total single muon efficiencies of high pileup L3 efficiencies. p_T dependence of the mean of the distribution of the parameter estimates of λ_{θ}^{PX} (top left), λ_{ϕ}^{PX} (top right), $\lambda_{\theta\phi}^{PX}$ (bottom left) and $\tilde{\lambda}^{PX}$ (bottom right) in the rapidity region $0 < |y'| < 1.2$. The error bars correspond to the first moment of the parameter distribution. The injected value is 0 for all parameters.

10 Summary and Conclusions

Quarkonium physics is an important tool to further the understanding of the strong interaction. Since the discovery of the J/ψ meson in 1974 - already 40 years ago - lots of different theories have emerged. The spectroscopy and the decay mechanisms of charmonium and bottomonium spectra are rather well described, but the mechanism of quarkonium production is still not yet satisfactorily understood. Quarkonium production considerations are based on factorization theorems which describe the production process in two independent phases – the formation of an initial quark-antiquark pair and the formation of a physical bound quarkonium state. Among these theories the NRQCD factorization approach is the most promising one. However, neither the NRQCD factorization approach nor any of the other theories available is able to describe quarkonium production and polarization at the same time. Before the LHC era, the polarization measurements showed inconsistencies. Only one of the three polarization parameters was determined, but in order to obtain unambiguous results, the full angular decay distribution has to be measured. Additionally, the measurement should be conducted in several reference frames. Then, a frame independent quantity $\tilde{\lambda}$ can be used to ensure the correctness of the result and the consistency of the analysis. CMS used this approach to study the polarizations of the $\Upsilon(nS)$ and prompt $\psi(nS)$ states. Thanks to the unprecedented rates of quarkonia at the LHC, the polarizations were measured up to high transverse momentum. The results showed no evidence of strong polarization.

Data taken with the CMS detector during the 2012 LHC run periods at a center of mass energy of $\sqrt{s} = 8$ GeV and an integrated luminosity of 20.7 fb^{-1} enables accurate polarization measurements of excited states like χ_{cJ} . χ_{cJ} states can be reconstructed via their radiative decays into $J/\psi + \gamma$, where the photon is measured through its pair conversion in the tracker. Recent studies showed that polarization measurements of J^{++} states can be conducted in the same way as 1^{--} states. The $J/\psi + \gamma$ data provide the inputs for the polarization studies. The most important inputs to measure the χ_{cJ} polarization are the single muon efficiencies and dimuon efficiency corrections. The efficiencies can change the measured polarization significantly if they are not determined correctly.

The total single muon detection efficiency can be calculated as the product of five sequential ones; with the exception of the offline muon tracking efficiency, the other four sequential efficiencies have been studied for seagull and cowboy dimuons

as well as for all dimuon pairs. Data-driven and MC based offline muon reconstruction efficiency, efficiency of the muon tracking quality cuts, L1·L2 efficiency, L3 efficiency and the total single muon efficiency product have been studied in detail as a function of p_T , $|\eta|$ and pileup. Additionally, the trigger path used in the χ_{cJ} polarization measurement contains a filter that is applied on dimuons, the dimuon vertexing module. Therefore, this efficiency has also been studied extensively. Moreover, muon pair correlations introduced by the dimuon trigger have been studied. Therefore, a special trigger, *HLT_Mu15_TkMu5_Onia* trigger, was designed to measure the ρ factor based on data.

At the time of writing this thesis, χ_{cJ} polarization studies, for which these single muon efficiencies and muon pair correlations are valuable inputs, are shortly before being finished. The quarkonium physics program at the LHC clearly has the potential to provide a wide range of polarization and cross-section measurements and, thus, might ultimately clear up remaining inconsistencies in quarkonium physics.

11 Acknowledgements

I would like to thank all my HEPHY colleagues for nearly a year of a very nice collaboration. Special thanks to Manfred Jeitler who brought me in touch with high energy physics, Wolfgang Adam who integrated me in the CMS analysis team and Claudia Wulz who supervised this thesis despite having an enormous tight timetable.

Many thanks to my working colleagues Ilse Krätschmer and Valentin Knünz who advised me on a daily basis, spend a lot of time looking at my problems and managed to finally make me understand the complex topic of quarkonium physics. I sincerely wish that both of you will have the opportunity to stay in physics for at least another couple of years. It was really a pleasure working with you!

The last five years of studying physics were undisputedly some of the best years in my life so far. Thanks to all my friends at the university for a lot of great and unforgettable memories: Philipp Moser, Thomas Madlener, Jakob Fellingner, Wolfgang Moser, Max Spanring - only to name a few.

Thanks to my tennis colleague Willi Kühberger who always had the time during the last five years to get a hit with me whenever I spend my weekends in Upper Austria.

Nothing would have been possible without my family Maria Brandstetter, Kurt Brandstetter and Clara Brandstetter. Thanks for all the support, thanks for always being prepared for a sudden visit and thanks for always listening to my problems and helping to solve them instantaneously.

Last but not least I would like to thank my gorgeous Clara Bodner! You have the ability of turning even the most exhausting day into a wonderful day worth to remember. Thanks for all your endurance and all your moral support.

12 Appendix A

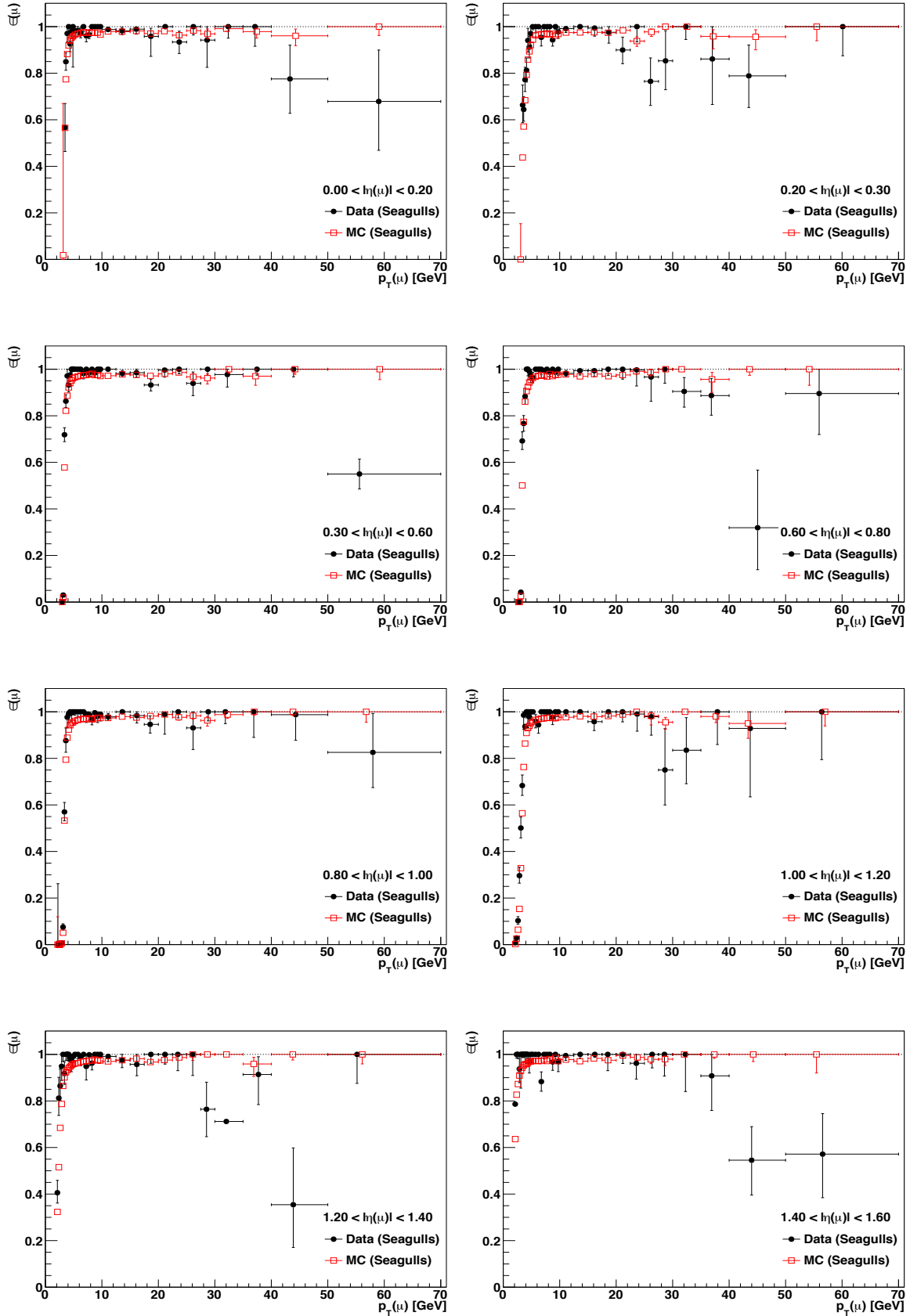


Figure 12.1: Offline muon reconstruction efficiencies calculated for seagull dimuons as a function of p_T for several $|\eta|$ bins.

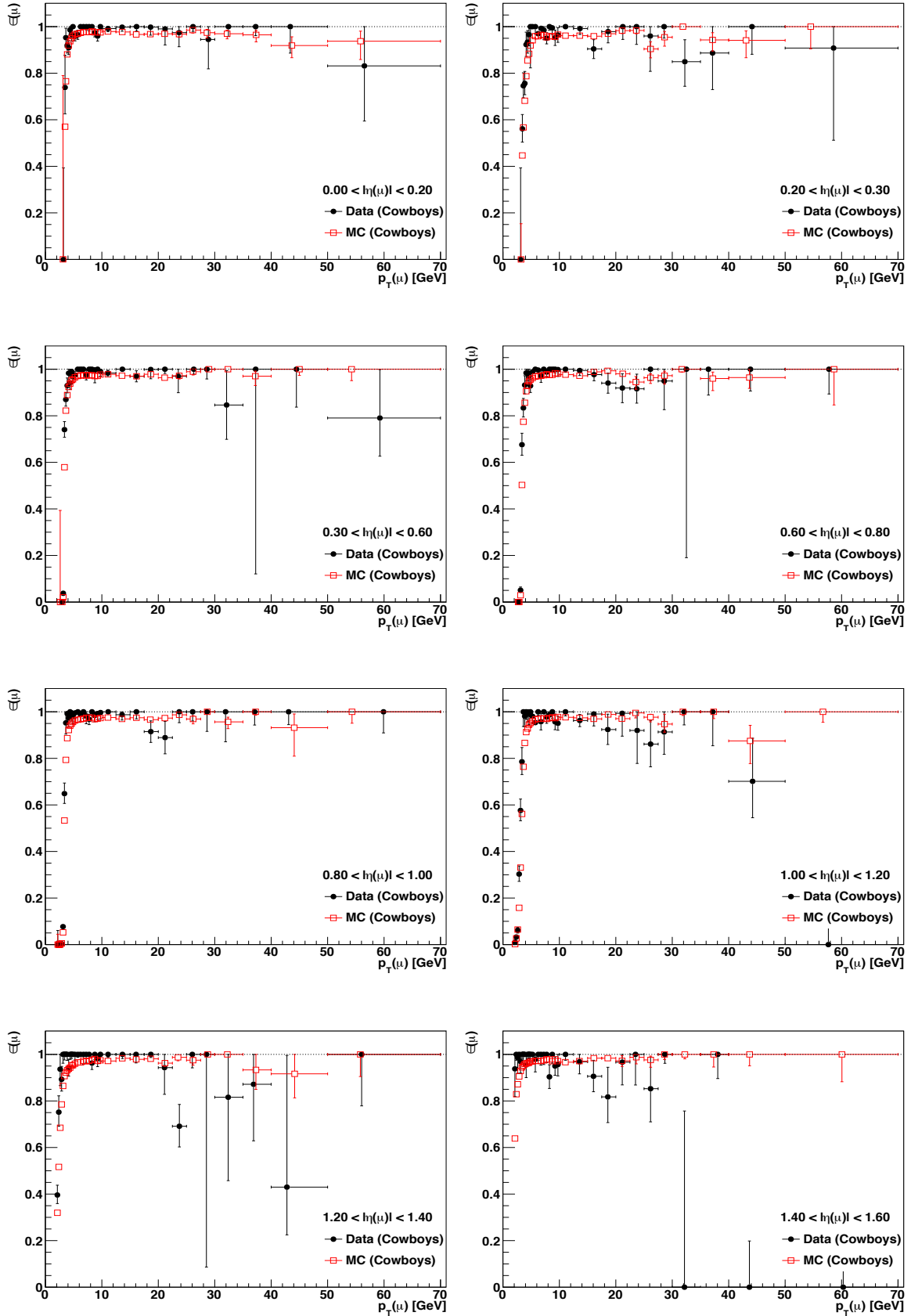


Figure 12.2: Offline muon reconstruction efficiencies calculated for cowboy dimuons as a function of p_T for several $|\eta|$ bins.

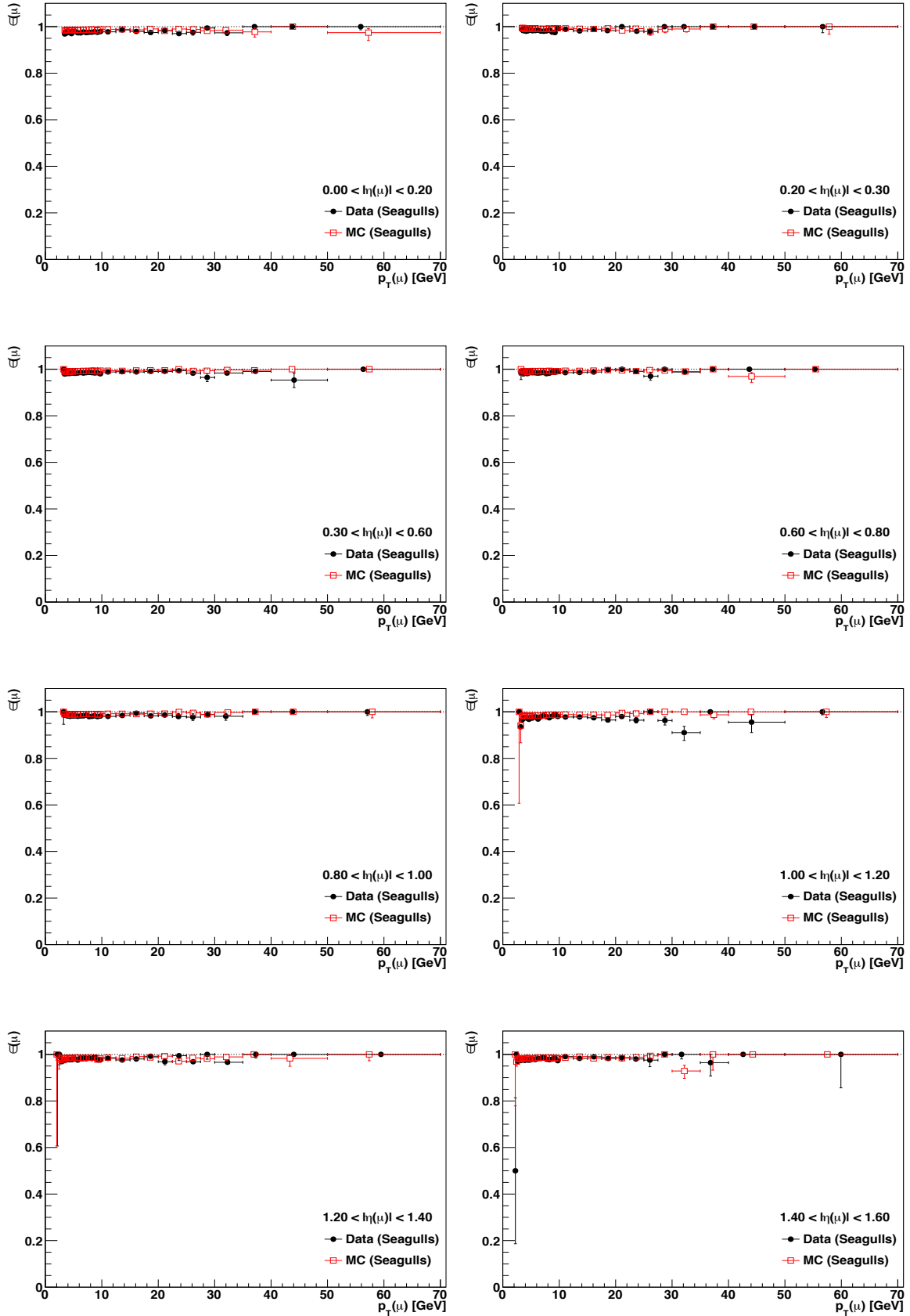


Figure 12.3: Efficiencies of the muon tracking quality cuts calculated for seagull dimuons as a function of p_T for several $|\eta|$ bins.

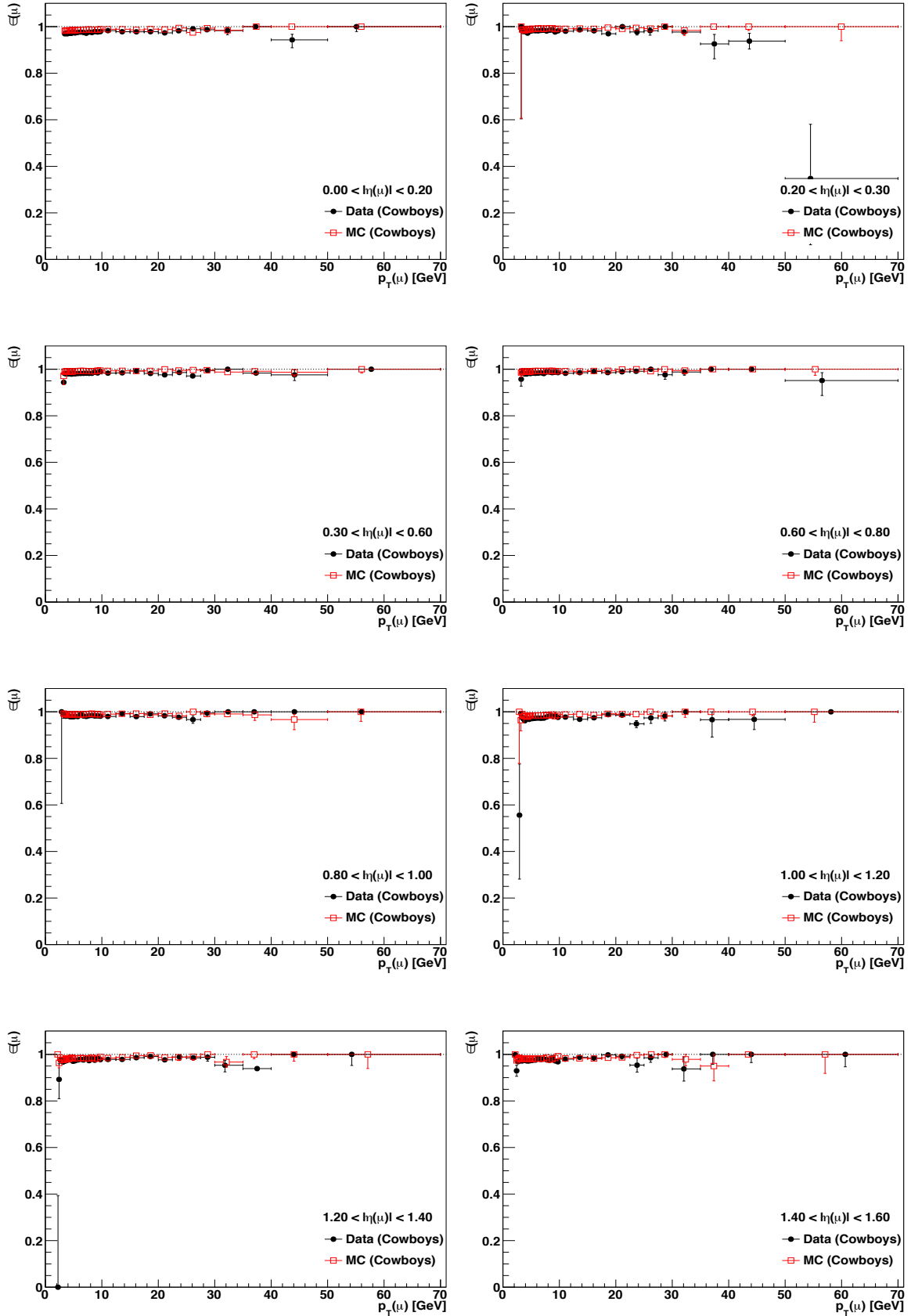


Figure 12.4: Efficiencies of the muon tracking quality cuts calculated for cowboy dimuons as a function of p_T for several $|\eta|$ bins.

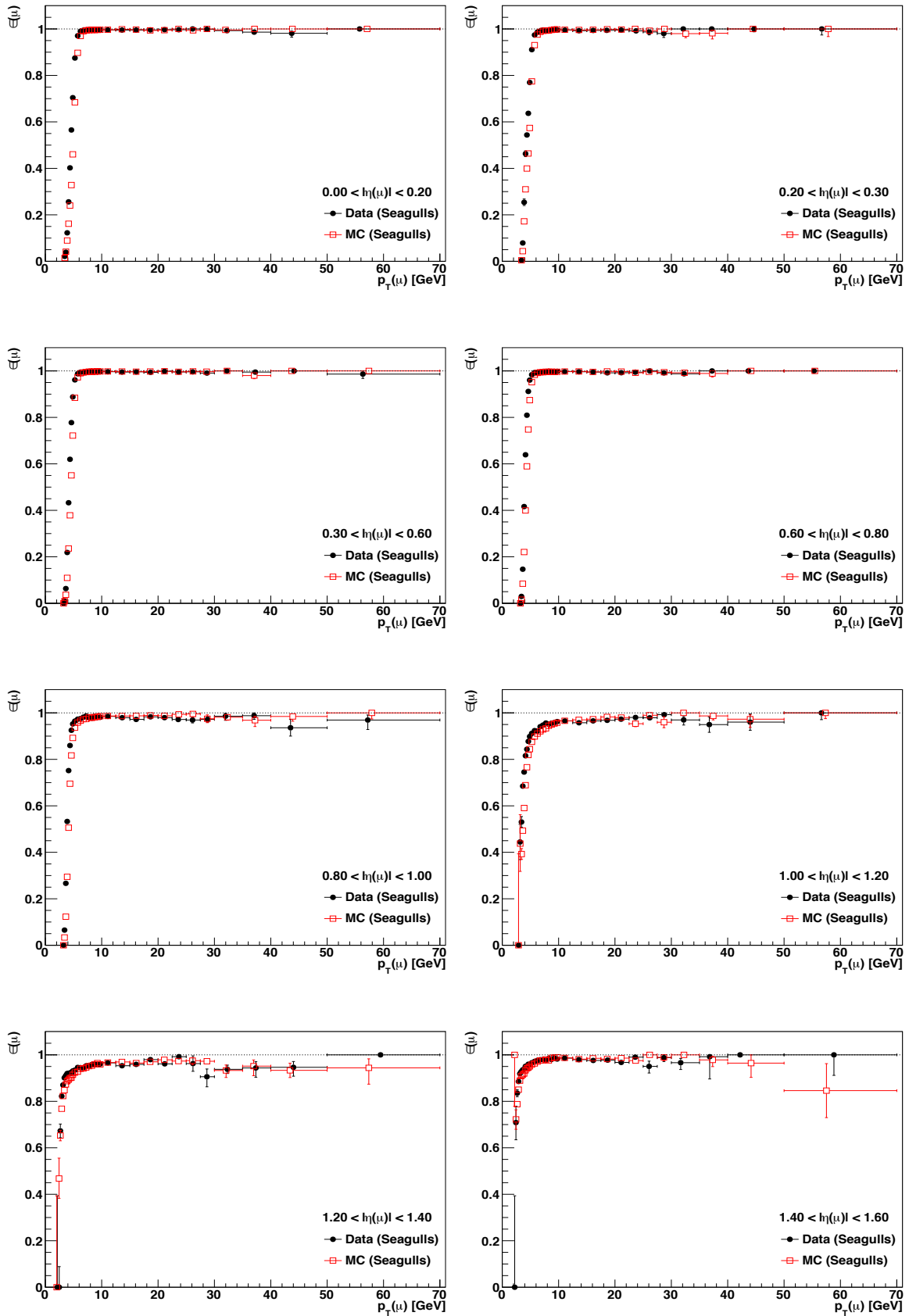


Figure 12.5: L3 Efficiencies calculated for seagull dimuons as a function of p_T for several $|\eta|$ bins.

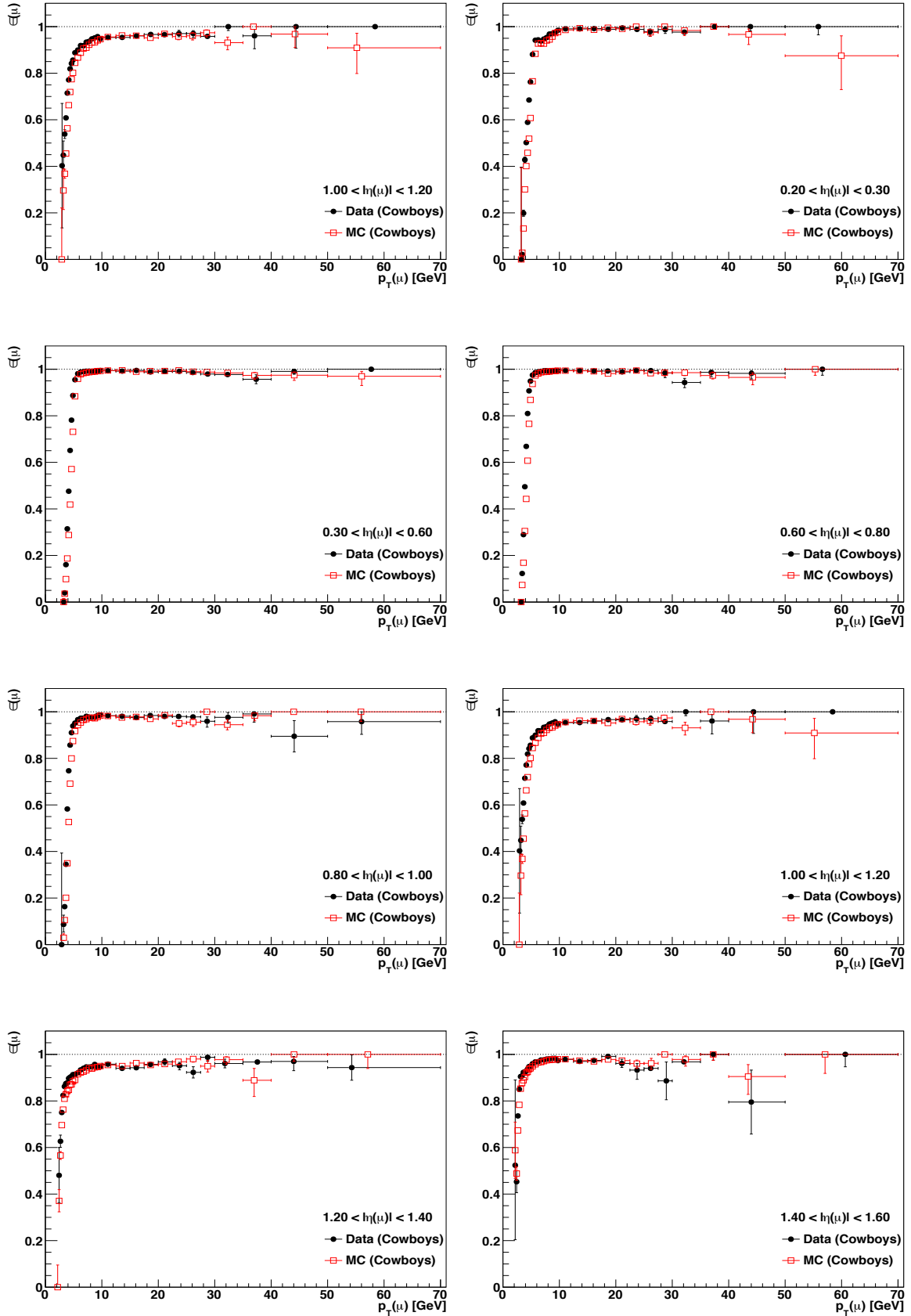


Figure 12.6: L3 Efficiencies calculated for cowboy dimuons as a function of p_T for several $|\eta|$ bins.

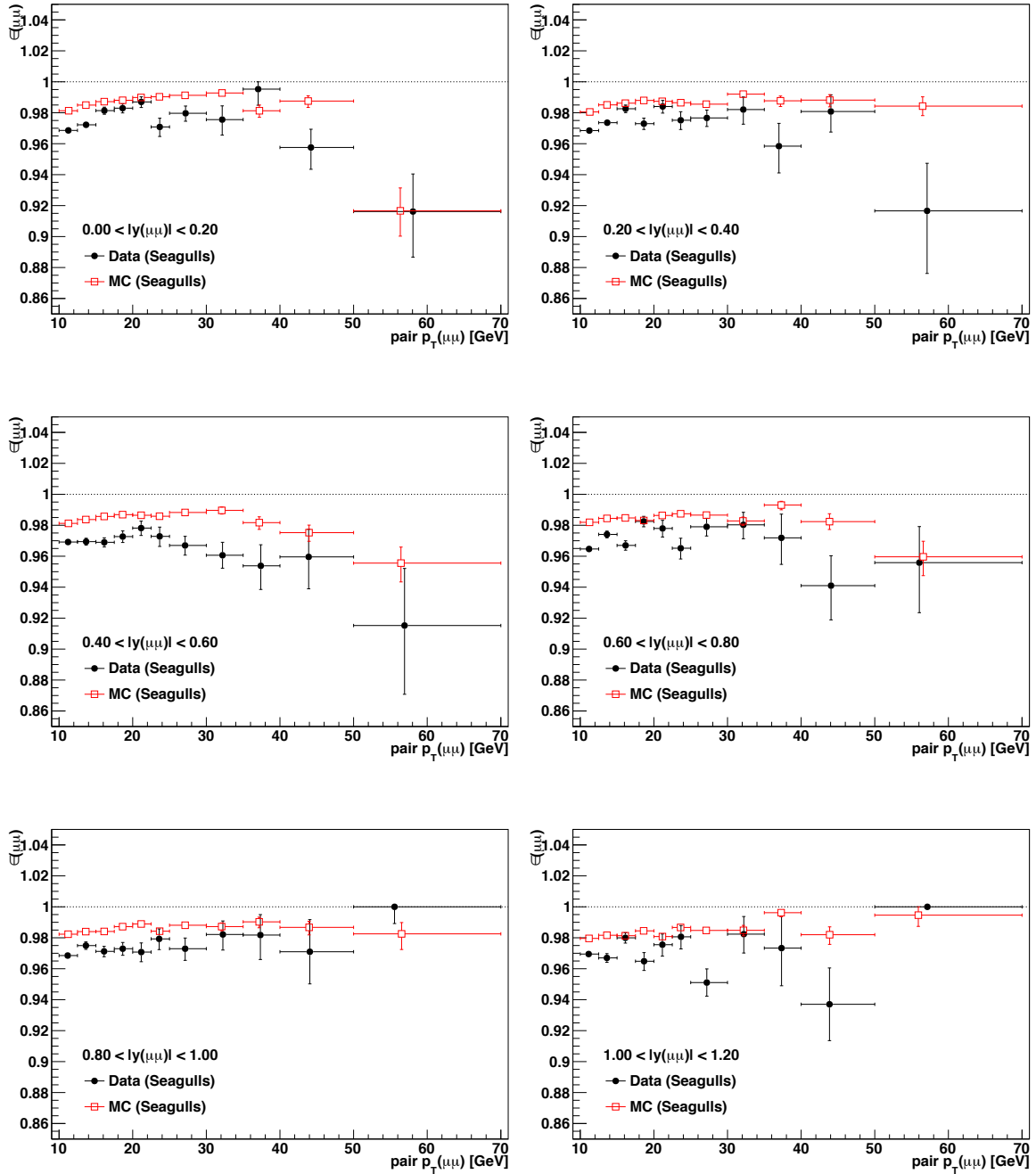


Figure 12.7: Vertex efficiencies calculated for seagull dimuons as a function of p_T for several $|\eta|$ bins.

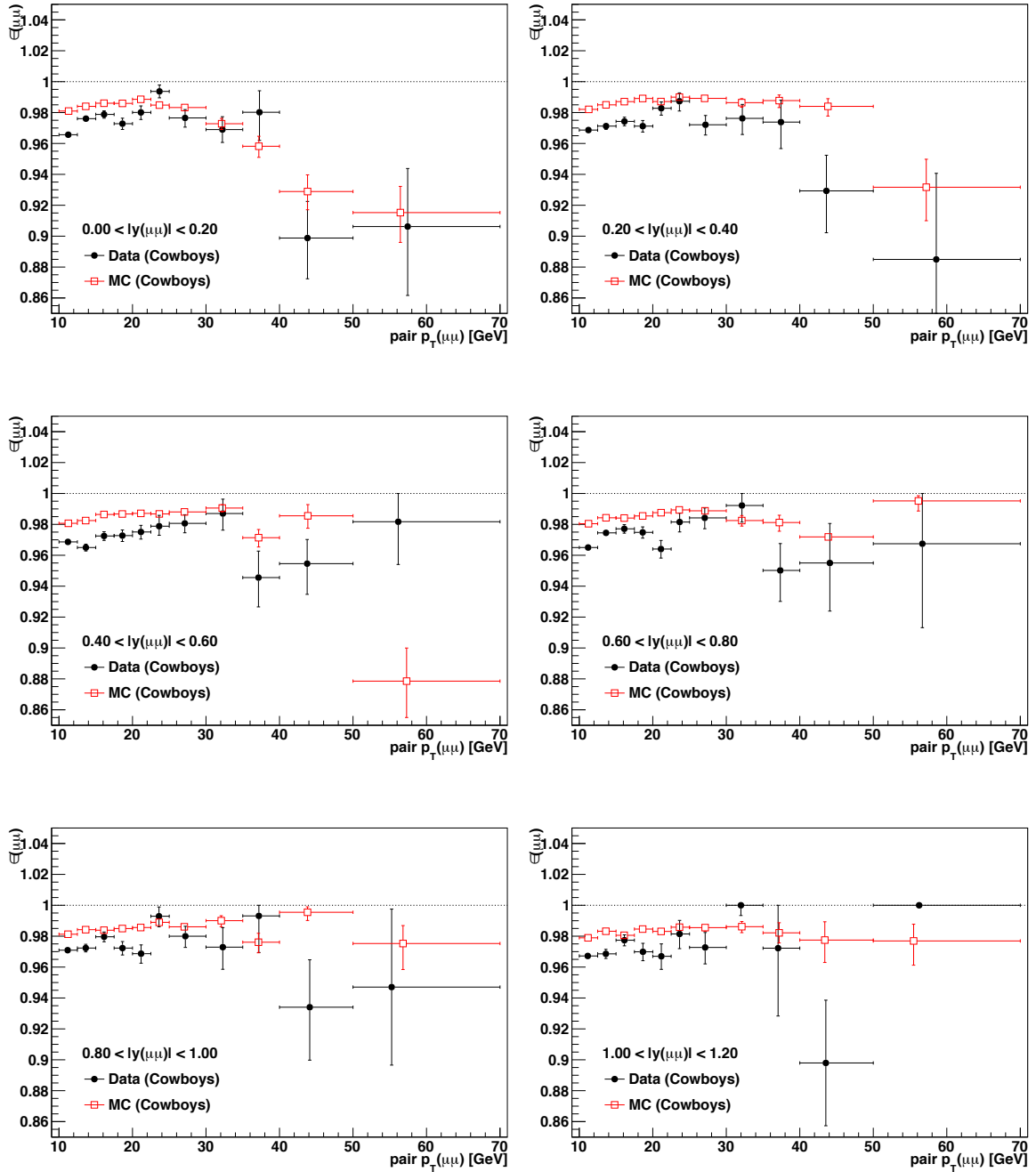


Figure 12.8: Vertex efficiencies calculated for cowboy dimuons as a function of p_T for several $|\eta|$ bins.

13 Appendix B

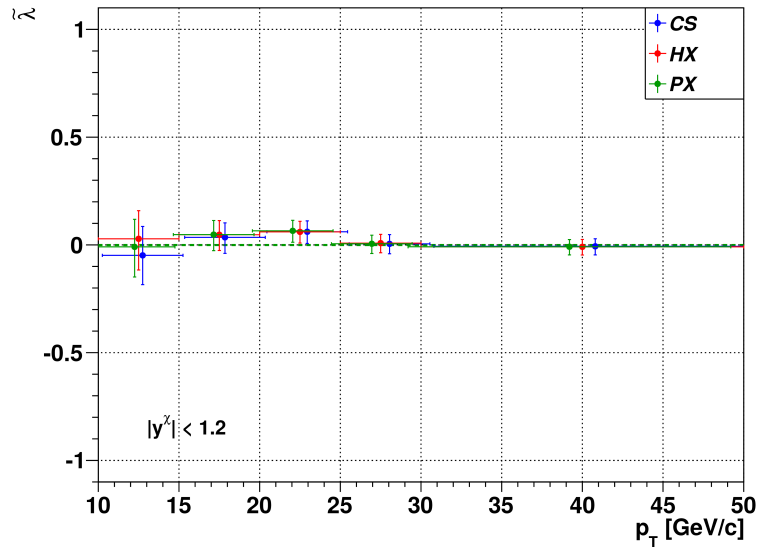


Figure 13.1: The absolute bias of $\tilde{\lambda}$ (in the CS, HX and PX frame) for the pseudo-data test of the total single muon efficiencies of cowboy dimuons as a function of p_T in the rapidity region $0 < |y| < 1.2$. The error bars correspond to the first moment of the parameter distribution. The dashed green line is the injected value.

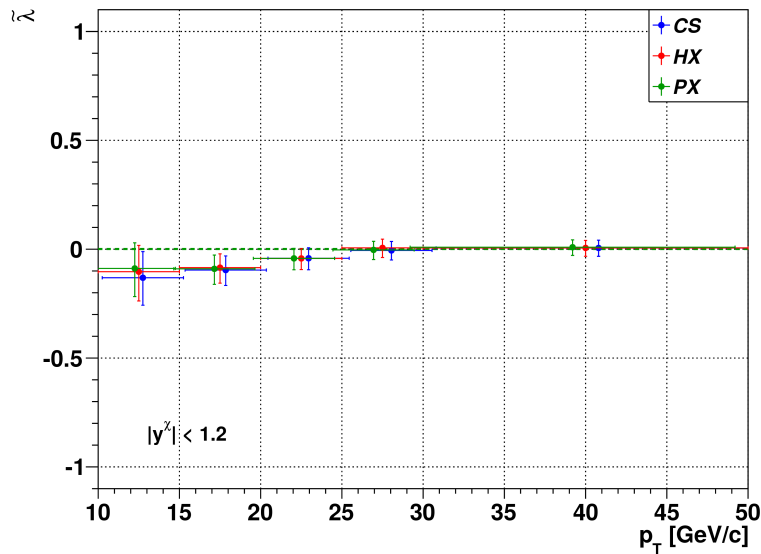


Figure 13.2: The absolute bias of $\tilde{\lambda}$ (in the CS, HX and PX frame) for the pseudo-data test of the total single muon efficiencies of seagull dimuons as a function of p_T in the rapidity region $0 < |y| < 1.2$. The error bars correspond to the first moment of the parameter distribution. The dashed green line is the injected value.

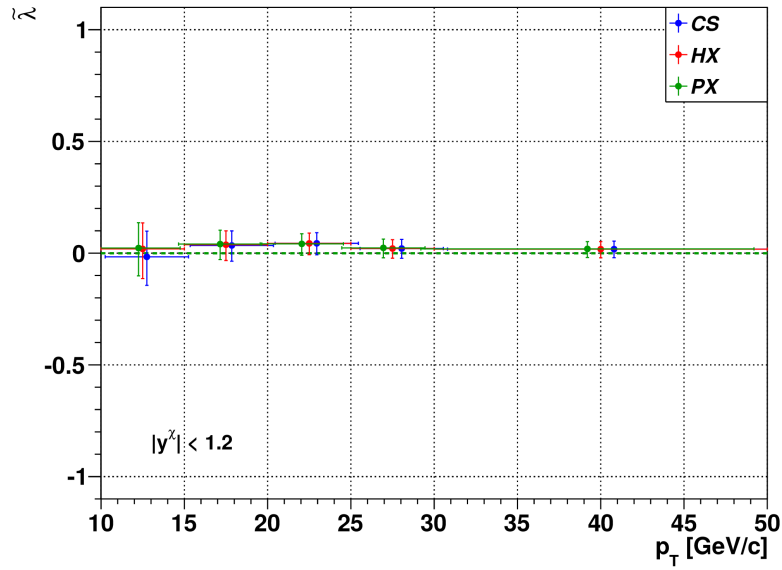


Figure 13.3: The absolute bias of $\tilde{\lambda}$ (in the CS, HX and PX frame) for the pseudo-data test of the total single muon efficiencies of low pileup L3 efficiencies as a function of p_T in the rapidity region $0 < |y| < 1.2$. The error bars correspond to the first moment of the parameter distribution. The dashed green line is the injected value.

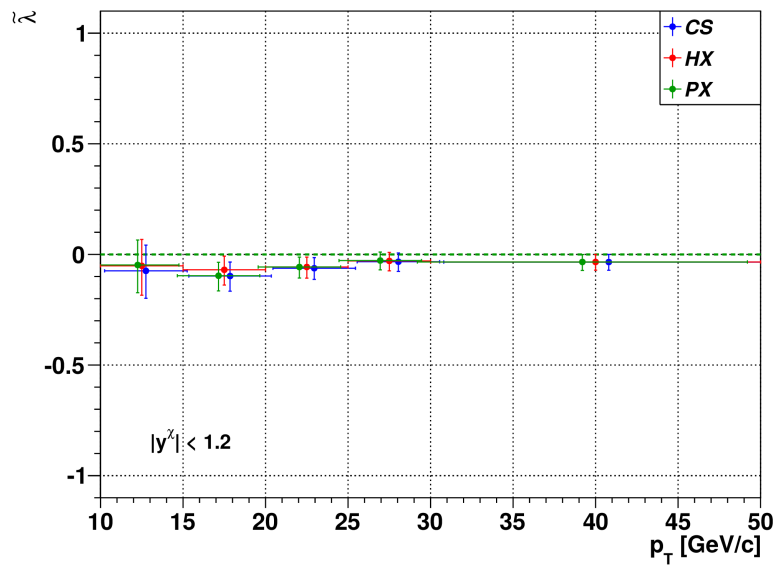


Figure 13.4: The absolute bias of $\tilde{\lambda}$ (in the CS, HX and PX frame) for the pseudo-data test of the total single muon efficiencies of high pileup L3 efficiencies as a function of p_T in the rapidity region $0 < |y| < 1.2$. The error bars correspond to the first moment of the parameter distribution. The dashed green line is the injected value.

Bibliography

- [1] *About Cern*. <http://home.web.cern.ch/about> (2011).
- [2] F. Hasert, H. Faissner *et al.* *Search for elastic muon-neutrino electron scattering*. *Physics Letters B* **46**, 121 (1973).
- [3] F. Hasert, S. Kabe *et al.* *Observation of neutrino-like interactions without muon or electron in the gargamelle neutrino experiment*. *Physics Letters B* **46**, 138 (1973).
- [4] UA1 Collaboration. *Experimental observation of isolated large transverse energy electrons with associated missing energy at $\sqrt{s} = 540$ GeV*. *Physics Letters B* **122**, 103 (1983).
- [5] G. Andresen *et al.* *Trapped antihydrogen*. *Nature* **468**, 673 (2010).
- [6] V. Fanti *et al.* *A new measurement of direct CP violation in two pion decays of the neutral kaon. A new measurement of direct CP violation in two pion decays of the neutral kaon*. *Physics Letters B* **465** (1999).
- [7] CMS Collaboration. *"Observation of a new boson at a mass of 125 GeV with the CMS experiment at the LHC"*. *Physics Letters B* **716(1)**, 30 (2012).
- [8] ATLAS Collaboration. *Observation of a new particle in the search of the Standard Model Higgs boson with the ATLAS detector at the LHC*. *Physical Letters B* **716(1)**, 1 (2012).
- [9] *LHC the guide*. CERN Brochure (2009).
- [10] *CMS Physics Technical Design Report: Detector performance and software*. No. Bd. 1 in CMS Technical design report. CERN (2006).
- [11] CMS Collaboration. *CMS Physics Technical Design Report, Volume II: Physics Performance*. *Journal of Physics G: Nuclear and Particle Physics* **34**, 995 (2007).
- [12] *Compact Muon Solenoid*. <http://cms.web.cern.ch/news/detector-overview> (2014).

-
- [13] *The CMS electromagnetic calorimeter project: Technical Design Report*. Technical Design Report CMS. CERN, Geneva (1997).
- [14] *The CMS hadron calorimeter project: Technical Design Report*. Technical Design Report CMS. CERN, Geneva (1997).
- [15] CMS Collaboration. *Performance of CMS muon reconstruction in pp collision events at $\sqrt{s} = 7$ TeV*. JINST **7**, P10002 (2012).
- [16] CMS Collaboration. *CMS, the Compact Muon Solenoid. Muon technical design report* (1997).
- [17] M. Felcini. *The Trigger System of the CMS Experiment*. Nucl.Instrum.Meth. **A598**, 312 (2009).
- [18] CMS Collaboration. *The CMS experiment at the CERN LHC*. JINST **3**, S08004 (2008).
- [19] CMS Collaboration. *The CMS Trigger System* (2013). CMS PAPER TRG-12-001.
- [20] V. Gori. *The CMS High Level Trigger*. Int.J.Mod.Phys.Conf.Ser. **31**, 1460297 (2014).
- [21] R. Frühwirth. *Application of Kalman filtering to track and vertex fitting*. Nucl. Instrum. Methods Phys. Res., A **262**, 444. 19 p (1987).
- [22] M. C. Llats. *The CMS Detector* (March 2013). Conference Aspen.
- [23] V. Veszpremi. *Operation and performance of the CMS tracker*. Journal of Instrumentation **9**, C03005 (2014).
- [24] D. H. Perkins. *Introduction to High Energy Physics*. Cambridge University Press (2000).
- [25] W. Cottingham and D. Greenwood. *An introduction to the standard model of particle physics*. Cambridge Univ Pr (2007).
- [26] C. S. Wu, E. Ambler, R. W. Hayward, D. D. Hoppes, and R. P. Hudson. *Experimental Test of Parity Conservation in Beta Decay*. Phys. Rev. **105**, 1413 (1957).
- [27] J. Christenson, J. Cronin, V. Fitch, and R. Turlay. *Evidence for the 2π Decay of the K_2^0 Meson*. Phys.Rev.Lett. **13**, 138 (1964).
- [28] University of Glasgow. *The Standard Model*. <http://www.physics.gla.ac.uk/ppt/research.htm> (2012).

- [29] The Economist online. *Worth the wait*. http://www.economist.com/blogs/graphicdetail/2012/07/daily-chart-1?fsrc=scn/tw_ec/worth_the_wait/ (2012).
- [30] O’Luanaigh, C. *New results indicate that new particle is a Higgs boson*. <http://home.web.cern.ch/about/updates/2013/03/new-results-indicate-new-particle-higgs-boson> (2013).
- [31] *Mechanik (Landau, L.D./E.M. Lifschitz: Lehrbuch der Theoretischen Physik)*. Akademie Verlag, 13th edition edn. (1990).
- [32] D. Flamm and F. Schöberl. *Introduction to the Quark Model of Elementary Particles*. Bd. 1.
- [33] J. Chadwick. *The Existence of a Neutron* **136**, 692 (1932).
- [34] H. Yukawa. *On the interaction of elementary particles*. Proc. Phys. Math. Soc. Jap. **17**, 48 (1935).
- [35] E. Fermi. *Quantum theory of radiation*. Rev. Mod. Phys. **4**, 87 (1932).
- [36] M. Gell-Mann. *A Schematic model of baryons and mesons*. Phys. Lett. **8**, 214 (1964).
- [37] G. Zweig. *An SU_3 model for strong interaction symmetry and its breaking; Version 2* p. 80 p (1964). Version 1 is CERN preprint 8182/TH.401, Jan. 17, 1964.
- [38] F. Tkachov. *A contribution to the history of quarks: Boris Struminsky’s 1965 JINR publication*. ArXiv e-prints (2009).
- [39] S. L. Glashow, J. Iliopoulos, and L. Maiani. *Weak Interactions with Lepton-Hadron Symmetry*. Phys. Rev. **D2**, 1285 (1970).
- [40] SLAC Collaboration. *Discovery of a Narrow Resonance in $e^+ e^-$ Annihilation*. Phys.Rev.Lett. **33**, 1406 (1974).
- [41] Brookhaven Collaboration. *Experimental Observation of a Heavy Particle J*. Phys. Rev. Lett. **33**, 1404 (1974).
- [42] N. Cabibbo. *Unitary Symmetry and Leptonic Decays*. Phys.Rev.Lett. **10**, 531 (1963).
- [43] J. H. Christenson, J. W. Cronin, V. L. Fitch, and R. Turlay. *Evidence for the 2π Decay of the K^0 Meson*. Phys. Rev. Lett. **13**, 138 (1964).

-
- [44] M. Kobayashi and T. Maskawa. *CP Violation in the Renormalizable Theory of Weak Interaction*. Prog. Theor. Phys. **49**, 652 (1973).
- [45] S. W. Herb *et al.* *Observation of a dimuon resonance at 9.5-GeV in 400-GeV proton - nucleus collisions*. Phys. Rev. Lett. **39**, 252 (1977).
- [46] J. Beringer *et al.* *Light Unflavored Mesons*. Phys.Rev.D **86** (2013).
- [47] ATLAS Collaboration. *Observation of a new χ_b state in radiative transitions to $\Upsilon(1S)$ and $\Upsilon(2S)$ at ATLAS*. Phys.Rev.Lett. **108** (2012).
- [48] T. Matsui and H. Satz. *J/ψ -suppression by quark gluon plasma formation*. Physics Letters B **178**, 416 (1986).
- [49] CMS Collaboration. *Indications of suppression of excited Υ states in PbPb collisions at $\sqrt{S_{NN}} = 2.76$ TeV*. Phys.Rev.Lett. **107**, 052302 (2011).
- [50] N. Brambilla *et al.* *Heavy Quarkonium Physics*. CERN, Geneva (2005).
- [51] N. Brambilla *et al.* *Heavy quarkonium: progress, puzzles, and opportunities*. The European physical journal / C **71**, 1534 (2011).
- [52] G. T. Bodwin, E. Braaten, and G. P. Lepage. *Rigorous QCD analysis of inclusive annihilation and production of heavy quarkonium*. Physical Review D **51**, 1125 (1995).
- [53] R. Baier and R. Rückl. *Hadronic production of J/ψ and ψ' : transverse momentum distributions*. Physics Letters B **102**, 364 (1981).
- [54] H. Fritzsche. *Producing heavy quark flavors in hadronic collisions- A test of quantum chromodynamics*. Physics Letters B **67**, 217 (1977).
- [55] G. T. Bodwin, E. Braaten, and J. Lee. *Comparison of the color-evaporation model and the NRQCD factorization approach in charmonium production*. Phys.Rev. (2005).
- [56] M. Krämer. *Quarkonium production at high-energy colliders*. Progress in Particle and Nuclear Physics **47**, 141 (2001).
- [57] CDF Collaboration. *J/Ψ and $\Psi(2S)$ Production in $p\bar{p}$ Collisions at $\sqrt{s} = 1.8$ TeV*. Phys. Rev. Lett. **79**, 572 (1997).
- [58] J. Lansberg. *J/Ψ production at $\sqrt{s} = 1.96$ and 7 TeV: colour-singlet model, NNLO and polarization*. Journal of Physics G: Nuclear and Particle Physics **38**, 124110 (2011).

- [59] M. Butenschön and B. A. Kniehl. *Reconciling J/ψ production at HERA, RHIC, Tevatron, and LHC with NRQCD factorization at next-to-leading order.* Phys.Rev.Lett. **106**, 022003 (2011).
- [60] P. Faccioli, C. Lourenco, J. Seixas, and H. K. Wöhri. *Towards the experimental clarification of quarkonium polarization.* Eur.Phys.J. **C69**, 657 (2010).
- [61] CMS Collaboration. *Measurement of the $\Upsilon(1S)$, $\Upsilon(2S)$, and $\Upsilon(3S)$ Polarizations in pp Collisions at $\sqrt{s} = 7$ TeV.* Phys. Rev. Lett. **110**, 081802 (2013).
- [62] P. Faccioli, C. Lourenco, and J. Seixas. *A New approach to quarkonium polarization studies.* Phys.Rev. **D81**, 111502 (2010).
- [63] P. Faccioli, C. Lourenco, and J. Seixas. *Rotation-invariant relations in vector meson decays into fermion pairs.* Phys.Rev.Lett. **105**, 061601 (2010).
- [64] P. Faccioli, C. Lourenco, J. Seixas et al. *Model-independent constraints on the shape parameters of dilepton angular distributions.* Phys. Rev. D (2011).
- [65] CDF Collaboration. *Measurement of J/ψ and $\psi(2S)$ polarization in $p\bar{p}$ collisions at $\sqrt{s} = 1.8$ TeV.* Phys. Rev. Lett. **85**, 12886 (2000).
- [66] CDF Collaboration. *Polarizations of J/ψ and $\psi(2S)$ Mesons Produced in $p\bar{p}$ Collisions at $\sqrt{s} = 1.96$ TeV.* Phys. Rev. Lett. **99**, 132001 (2007).
- [67] P. Faccioli, C. Lourenco, J. Seixas, and H. K. Wöhri. *Determination of χ_c and χ_b polarizations from dilepton angular distributions in radiative decays.* Phys.Rev. **D83**, 096001 (2011).
- [68] CMS Collaboration. *Prompt and non-prompt J/ψ production in pp collisions at $\sqrt{s} = 7$ TeV.* Eur.Phys.J. **C71**, 1575 (2011).
- [69] J. Beringer et al. *Review of Particle Physics.* Phys. Rev. D **86**, 010001 (2012).
- [70] M. Oreglia. *A Study of the Reactions $\psi' \rightarrow \gamma\gamma\psi$* (1980).
- [71] V. Knünz. Private Conversation with Valentin Knünz (2014).
- [72] CMS Collaboration. *Measurement of the prompt J/ψ and $\psi(2S)$ polarizations in pp collisions at $\sqrt{s} = 7$ TeV.* Phys.Lett. **B727**, 381 (2013).
- [73] CMS Collaboration. *Measurement of the $\Upsilon(1S)$, $\Upsilon(2S)$, and $\Upsilon(3S)$ Polarizations in pp Collisions at $s=7$ TeV.* Phys. Rev. Lett. **110**, 081802 (2013).
- [74] G. Petrucciani et al. *Documentation for TagProbeFitTreeProducer.* <https://twiki.cern.ch/twiki/bin/view/CMSPublic/SWGuideTagProbeFitTreeProducer> (2011).

-
- [75] G. Petrucciani *et al.* *Documentation for TagProbeFitTreeAnalyzer*. <https://twiki.cern.ch/twiki/bin/view/CMSPublic/SWGuideTagProbeFitTreeAnalyzer> (2010).
- [76] CMS Collaboration. *CMS Performance Note: Muon ID performance: low p_T muon efficiencies*. CMS DP-2014/020 (2014).
- [77] H. Wöhri, I. Krätschmer, J. Wang, and L. Zhang. *T&P single muon efficiencies for low p_T dimuon triggers in 2011*. CMS AN AN-11-417 (internal note, unpublished) (2011).
- [78] CMS Collaboration. *CMS-PAS-BPH-14-001* (2014).
- [79] R. Frühwirth. Private Conversation with Rudolf Frühwirth (2014).

List of Figures

Figure 2.1	Sketch of experiments and accelerators running at CERN [9].	10
Figure 3.1	Segment of the CMS detector with various layers [12].	13
Figure 3.2	Layout of the muon systems [15].	16
Figure 3.3	Example of four reconstructed muons [15].	17
Figure 3.4	Different stages of the CMS triggering, starting at 40 MHz and ending at 100 Hz [17].	18
Figure 3.5	Structure of L1 trigger information flow [18].	19
Figure 3.6	Integrated luminosities and pileup distribution recorded by the CMS detector in 2012 [23].	21
Figure 4.1	Particles of the standard model [28].	24
Figure 4.2	Prediction and discovery of important particles involved in the standard model [29].	25
Figure 5.1	First observation of the J/ψ resonance: (a) at Brookhaven in a fixed target experiment using p+Be collisions, (b) at the Stanford Linear Collider in e^+e^- collisions with J/ψ decaying into a multi-hadron state (top), into $\mu^+\mu^-$ (middle) and e^+e^- final states (bottom).	30
Figure 5.2	Charmonium spectrum [46].	31
Figure 5.3	Bottomonium spectrum [46].	31
Figure 5.4	Comparison of color-singlet and color-octet calculations to prompt J/ψ (left) and $\Upsilon(1S)$ (right) production at the Tevatron ($\sqrt{s} = 1.8$ TeV).	37
Figure 5.5	NLO and NNLO* contributions of the CSM for J/ψ (left) and $\Upsilon(1S)$ (right) (using CDF II data taken at $\sqrt{s} = 1.96$).	38
Figure 5.6	Global fits of the NRQCD factorization approach at NLO at different rapidity regions compared to data taken with the CDF detector at Fermilab (top left), the CMS (top right) and the LHCb detectors (bottom) at CERN.	38

Figure 6.1	Definition of polar (ϑ) and azimuthal angle (φ) of the positive lepton (l^+) (upper plot), definition of production plane and quarkonium rest frame (bottom left, bottom right) [60]. \mathbf{b}_1 and \mathbf{b}_2 refer to the two colliding proton beams.	40
Figure 6.2	Graphical representation of Eqs. 6.2, 6.2 and 6.3.	41
Figure 6.3	Values of λ_ϑ and λ_φ for fully transversely (a) and fully longitudinally (b) polarized states.	42
Figure 6.4	J/ψ polarization measurements conducted by CDF Tevatron Run I ($\sqrt{s} = 1.8$ GeV) and Run II ($\sqrt{s} = 1.96$ GeV). α corresponds to the λ_ϑ parameter as function of p_T . The results are compared to theoretical models [65][66].	43
Figure 6.5	χ mass-lifetime model divided into 8 different regions. See text for further explanations [71].	46
Figure 6.6	Dimuon invariant-mass (a) and lifetime distribution (b) in the J/ψ region for $18 < p_T < 20$ GeV and absolute rapidity < 0.6 [72].	47
Figure 6.7	Dimuon mass distribution in the $\Upsilon(nS)$ region for two rapidity bins [73].	47
Figure 6.8	Values of $\tilde{\lambda}$ for the J/ψ (top), for the $\psi(2S)$ (middle) and for $\Upsilon(1S)$, $\Upsilon(2S)$ and $\Upsilon(3S)$ (bottom) [72][73].	48
Figure 7.1	Example of a simultaneous fit to passing and failing probes in the $10 \text{ GeV} < p_T < 12.5 \text{ GeV}$ and $0.0 < \eta < 0.2$ bin. The lower right plot contains variables for passing and failing probe and the deduced efficiency.	50
Figure 7.2	Simultaneous fit to passing and failing probes in the $0.0 < \eta < 0.2$ and $10 \text{ GeV} < p_T < 12.5 \text{ GeV}$ bin. The lower right plot contains variables for passing and failing probe and the deduced efficiency.	54
Figure 7.3	Offline muon reconstruction efficiencies as a function of p_T for several $ \eta $ bins calculated for all dimuon pairs.	55
Figure 7.4	Ratio data/MC for offline muon reconstruction efficiencies as a function of p_T for several $ \eta $ bins. Error bars correspond to the first moment of the MC driven efficiencies.	56
Figure 7.5	Data-driven offline muon reconstruction efficiencies calculated for seagull and cowboy dimuons as a function of p_T for several $ \eta $ bins.	57
Figure 7.6	Ratio of MC driven offline muon reconstruction efficiencies calculated for seagull dimuons over the one calculated for cowboy dimuons as a function of p_T for several $ \eta $ bins. The error bars correspond to the first moment of the respective fraction.	58

Figure 7.7	Data/MC scale factors as a function of p_T for different $ \eta $ bins fitted with a $\frac{1}{p^\alpha}$ function at low p_T and with a constant at high p_T	59
Figure 7.8	Efficiencies of the muon tracking quality cuts as a function of p_T for several $ \eta $ bins calculated for all dimuon pairs. . .	61
Figure 7.9	Data-driven efficiencies of the muon tracking quality cuts for seagull and cowboy dimuons as a function of p_T for several $ \eta $ bins.	62
Figure 7.10	L1·L2 efficiencies as a function of p_T for several $ \eta $ bins calculated for all dimuon pairs.	64
Figure 7.11	L1·L2 efficiencies as a function of p_T for several η bins calculated for seagull dimuons.	65
Figure 7.12	L1·L2 efficiencies as a function of p_T for several η bins calculated for cowboy dimuons.	66
Figure 7.13	Data-driven L1·L2 efficiencies for seagull and cowboy dimuons as a function of p_T for several $ \eta $ bins.	67
Figure 7.14	Ratio of MC driven L1·L2 efficiencies calculated for seagull dimuons over the one calculated for cowboy dimuons as a function of p_T for several $ \eta $ bins. The error bars correspond to the first moment of the respective fraction.	68
Figure 7.15	Data-driven L1·L2 efficiencies for seagull and cowboy dimuon as a function of p_T in forward $ \eta $ bins (top). Ratio of MC driven L1·L2 efficiencies calculated for seagull dimuons over the one calculated for cowboy dimuons as a function of p_T in forward $ \eta $ bins (bottom). The error bars correspond to the first moment of the respective fraction.	69
Figure 7.16	L3 efficiencies as a function of p_T for several $ \eta $ bins calculated for all dimuon pairs.	71
Figure 7.17	L3 efficiencies for seagull and cowboy dimuons as a function of η for several p_T bins.	72
Figure 7.18	L3 efficiencies for seagull dimuons as a function of $\pm\eta$ for several p_T bins.	73
Figure 7.19	L3 efficiencies for cowboy dimuons as a function of $\pm\eta$ for several p_T bins.	74
Figure 7.20	Total single muon efficiencies as a function of p_T for several $ \eta $ bins calculated for all dimuon pairs.	76
Figure 7.21	Total single muon efficiencies as a function of p_T for several $ \eta $ bins calculated for seagull dimuons.	77
Figure 7.22	Total single muon efficiencies as a function of p_T for several $ \eta $ bins calculated for cowboy dimuons.	78
Figure 7.23	Data-driven total single muon efficiencies for seagull and cowboy dimuons as a function of p_T for several $ \eta $ bins. . .	79

Figure 7.24	Ratio of MC based total single muon efficiencies for seagulls over the one for cowboys as function of p_T for several $ \eta $ bins. The error bars correspond to the first moment of the respective fraction.	80
Figure 7.25	Ratio of MC based TnP efficiencies over MC-truth total single muon efficiencies calculated for all dimuons as function of p_T for several $ \eta $ bins.	81
Figure 7.26	Distribution of the number of vertices for the different run periods in 2012 (left) and for all run periods in comparison to the MC simulation (right).	82
Figure 7.27	Offline muon reconstruction efficiency (a), efficiency of the muon quality cuts (b), L1·L2 efficiency (c) and L3 efficiency (d) as a function of the number of vertices for $7.5 \text{ GeV} < p_T < 70 \text{ GeV}$ and $ \eta < 2.0$	83
Figure 7.28	Vertex efficiency as a function of dimuon p_T for several bins of dimuon $ y $	85
Figure 7.29	Vertex efficiency as a function of φ for several bins of $\cos \vartheta$ in the PX frame.	86
Figure 8.1	ρ factor calculated without any efficiency corrections for seagull and cowboy dimuons (a). 2011 MC ρ factor for seagull dimuons (b) [78].	89
Figure 8.2	Total efficiency corrections for seagull and cowboy dimuons.	91
Figure 8.3	Data-driven $L1 \cdot L2 \cdot L3$ efficiency requiring that the muon passed the tracker muon leg of the onia trigger as a function of p_T for several $ \eta $ bins for seagull and cowboy dimuons. .	92
Figure 8.4	Efficiency corrected ρ factor for seagull dimuons as a function of dimuon p_T and integrated $ y $	94
Figure 8.5	Efficiency corrected ρ factors for seagull dimuons as a function of p_T for several bins in $ y $	94
Figure 8.6	Efficiency corrected ρ factor for cowboy dimuons as a function of dimuon p_T and integrated $ y $	95
Figure 8.7	Efficiency corrected ρ factors for cowboy dimuons as a function of p_T for several bins in $ y $	95
Figure 9.1	Distribution of λ_φ (a) and pull distribution (b) in the bin $ y < 1.2$, $15 < p_T < 30 \text{ GeV}$ for 50 generated pseudo-data sets. Parameter distribution: Solid green line corresponds to an imposed Gaussian fit of the results and dotted red line to the injected parameter. Pull distribution: Solid green line corresponds to an imposed Gaussian fit of the results and dotted red line to the expected parameter distribution.	97

- Figure 9.2 Absolute bias of the $\tilde{\lambda}$ parameter introduced by the testing framework (in the CS, HX and PX frames). The error bars correspond to the first moment of the parameter distribution. The dashed green line is the injected value. 99
- Figure 9.3 The absolute bias of the polarization parameters in the PX frame for the pseudo-data test of the total single muon efficiencies of cowboy dimuons. p_T dependence of the mean of the distribution of the parameter estimates of λ_θ^{PX} (top left), λ_φ^{PX} (top right), $\lambda_{\theta\varphi}^{PX}$ (bottom left) and $\tilde{\lambda}^{PX}$ (bottom right) in the rapidity region $0 < |y| < 1.2$. The error bars correspond to the first moment of the parameter distribution. The injected value is 0 for all parameters. 100
- Figure 9.4 The absolute bias of the polarization parameters in the PX frame for the pseudo-data test of the total single muon efficiencies of seagull dimuons. p_T dependence of the mean of the of the distribution of the parameter estimates of λ_θ^{PX} (top left), λ_φ^{PX} (top right), $\lambda_{\theta\varphi}^{PX}$ (bottom left) and $\tilde{\lambda}^{PX}$ (bottom right) in the rapidity region $0 < |y| < 1.2$. The error bars correspond to the first moment of the parameter distribution. The injected value is 0 for all parameters. 102
- Figure 9.5 Distribution of the number of vertices in MC. The dashed red lines indicate three different pileup regions. 104
- Figure 9.6 Data-driven L3 efficiencies calculated for low and high pileup events as a function of p_T for several $|\eta|$ bins. The error bars correspond to the first moment of the respective fraction. . 105
- Figure 9.7 MC-driven L3 efficiencies calculated for low and high pileup events as a function of p_T for several $|\eta|$ bins. The error bars correspond to the first moment of the respective fraction. . 106
- Figure 9.8 The absolute bias of the polarization parameters in the PX frame for the pseudo-data test of the total single muon efficiencies of low pileup L3 efficiencies. p_T dependence of the mean of the of the distribution of the parameter estimates of λ_θ^{PX} (top left), λ_φ^{PX} (top right), $\lambda_{\theta\varphi}^{PX}$ (bottom left) and $\tilde{\lambda}^{PX}$ (bottom right) in the rapidity region $0 < |y| < 1.2$. The error bars correspond to the first moment of the parameter distribution. The injected value is 0 for all parameters. . . 107

Figure 9.9	The absolute bias of the polarization parameters in the PX frame for the pseudo-data test of the total single muon efficiencies of high pileup L3 efficiencies. p_T dependence of the mean of the of the distribution of the parameter estimates of λ_ϑ^{PX} (top left), λ_φ^{PX} (top right), $\lambda_{\vartheta\varphi}^{PX}$ (bottom left) and $\tilde{\lambda}^{PX}$ (bottom right) in the rapidity region $0 < y < 1.2$. The error bars correspond to the first moment of the parameter distribution. The injected value is 0 for all parameters. . .	108
Figure 12.1	Offline muon reconstruction efficiencies calculated for seagull dimuons as a function of p_T for several $ \eta $ bins.	113
Figure 12.2	Offline muon reconstruction efficiencies calculated for cowboy dimuons as a function of p_T for several $ \eta $ bins.	114
Figure 12.3	Efficiencies of the muon tracking quality cuts calculated for seagull dimuons as a function of p_T for several $ \eta $ bins. . .	115
Figure 12.4	Efficiencies of the muon tracking quality cuts calculated for cowboy dimuons as a function of p_T for several $ \eta $ bins. . .	116
Figure 12.5	L3 Efficiencies calculated for seagull dimuons as a function of p_T for several $ \eta $ bins.	117
Figure 12.6	L3 Efficiencies calculated for cowboy dimuons as a function of p_T for several $ \eta $ bins.	118
Figure 12.7	Vertex efficiencies calculated for seagull dimuons as a function of p_T for several $ \eta $ bins.	119
Figure 12.8	Vertex efficiencies calculated for cowboy dimuons as a function of p_T for several $ \eta $ bins.	120
Figure 13.1	The absolute bias of $\tilde{\lambda}$ (in the CS, HX and PX frame) for the pseudo-data test of the total single muon efficiencies of cowboy dimuons as a function of p_T in the rapidity region $0 < y < 1.2$. The error bars correspond to the first moment of the parameter distribution. The dashed green line is the injected value.	122
Figure 13.2	The absolute bias of $\tilde{\lambda}$ (in the CS, HX and PX frame) for the pseudo-data test of the total single muon efficiencies of seagull dimuons as a function of p_T in the rapidity region $0 < y < 1.2$. The error bars correspond to the first moment of the parameter distribution. The dashed green line is the injected value.	122

Figure 13.3	The absolute bias of $\tilde{\lambda}$ (in the CS, HX and PX frame) for the pseudo-data test of the total single muon efficiencies of low pileup L3 efficiencies as a function of p_T in the rapidity region $0 < y < 1.2$. The error bars correspond to the first moment of the parameter distribution. The dashed green line is the injected value.	123
Figure 13.4	The absolute bias of $\tilde{\lambda}$ (in the CS, HX and PX frame) for the pseudo-data test of the total single muon efficiencies of high pileup L3 efficiencies as a function of p_T in the rapidity region $0 < y < 1.2$. The error bars correspond to the first moment of the parameter distribution. The dashed green line is the injected value.	123

List of Tables

5.1	Properties of the charmonium meson family [46].	32
5.2	Properties of the bottomonium meson family [46].	32
7.1	Data/MC scale factors of the offline muon tracking efficiency for different $ \eta $ bins.	51
7.2	p_T ranges of the different HLT_MuX_TrackY_Jpsi triggers.	52
9.1	Mean of the distribution of the standard score $z(\lambda_i)$: $\mu_{z(\lambda_i)} \pm \sigma_{\mu_{z(\lambda_i)}}$ for the unpolarized pseudo-data test where the pseudo-data sets are reconstructed with the single muon efficiencies calculated for cowboy dimuons.	101
9.2	R.m.s. of the distribution of the standard score $z(\lambda_i)$: $\sigma_{z(\lambda_i)} \pm \sigma_{\sigma_{z(\lambda_i)}}$ for the unpolarized pseudo-data test where the pseudo-data sets are reconstructed with the single muon efficiencies calculated for cowboy dimuons.	101
9.3	Means of the distribution of the standard score $z(\lambda_i)$: $\mu_{z(\lambda_i)} \pm \sigma_{\mu_{z(\lambda_i)}}$ for the unpolarized pseudo-data test where the pseudo-data sets are reconstructed with the single muon efficiencies calculated for seagull dimuons.	103

9.4 R.m.s. of the distribution of the standard score $z(\lambda_i)$: $\sigma_{z(\lambda_i)} \pm \sigma_{\sigma_{z(\lambda_i)}}$
for the unpolarized pseudo-data test where the pseudo-data sets are
reconstructed with the single muon efficiencies calculated for seagull
dimuons. 103

Acronyms and Abbreviations

ALICE A Large Ion Collider Experiment

ATLAS A Toroidal LHC Apparatus

CDF Collider Detector at Fermilab

CDF II upgraded Collider Detector at Fermilab

CEM color-evaporation model

CERN European Organization for Nuclear Research

CPT charge, parity and time

CSC Cathode Stripe Chambers

CSM color-singlet model

DT Drift Tubes

ECAL Electromagnetic Calorimeter

GCT Global Calorimeter Trigger

GMT Global Muon Trigger

GT Global trigger

HCAL Hadronic Calorimeter

HLT High Level Trigger

L1 Level-1 Trigger

L2 Level-2

L3 Level-3

LDME long distance matrix element

LHCb Large Hadron Collider beauty

LINAC	Linear Particle Accelerator
MC	Monte Carlo
NLO	next-to-leading order term in Tylor expansion
NNLO	next-to-next-to-leading order term in Taylor expansion
NRQCD	non relativistic quantum chromodynamics
PDF	probability density function
POG	Physics Object Group
PPD	posterior probability density
PS	Proton Synchrotron
PSB	Proton Synchrotron Booster
QED	quantum electrodynamics
QGP	quark-gluon plasma
r.m.s	root mean square
RPC	Resistive Plate Chamber
SDC	short distance coefficient
SPS	Super Proton Synchrotron
TnP	Tag and Probe